**School of Civil and Mechanical Engineering**
**Department of Civil Engineering**

# Capacity of OSB Skin Structural Insulated Panels with Strengthening to Resist Windborne Debris Impact

**Qingfei Meng**

**This thesis is presented for the Degree of**
**Doctor of Philosophy**
**of**
**Curtin University**

**April 2018**

## Declaration

To the best of my knowledge and belief this thesis contains no material previously published by any other person except where due acknowledgment has been made.

This thesis contains no material which has been accepted for the award of any other degree or diploma in any university.

Signature: .....

Date: 20/4/2018

# Abstract

Devastating losses of building structures caused by strong winds have been frequently reported around the world. In Australia, tropical cyclone is considered one of the major natural hazards, especially in Northern regions of Western Australia and Queensland. To account for the high wind speed for building structure and personnel protection, the capacity of existing structural panels to resist windborne debris impacts needs be investigated, and new designs and strengthening techniques of structural panels with increased impact resistance capacities need be developed.

The direct wind load acting on building structures is the wind pressure and suction, which may damage the structural windows, walls and lift up roofs. Strong wind might also lift up debris from damaged structures, roof tiles, and broken tree trunks and propel them at high speed to impact on building structures, which could cause damages to structures by creating openings on structure walls and roofs. The penetrated debris into the room also imposes a great threat to people in the house. An opening on building envelope would also increase the pressure differentials outside and inside the house and make the wall more vulnerable to collapse and roof to be lifted up. Therefore for building structure protection against strong wind, the structural walls/roofs should be strong enough not only to resist wind pressure, but also to resist windborne debris impact. The Australian wind loading codes (AS/NZS 1170.2:2011) has specific requirement on structural panels to resist windborne debris impact. It requires the structural panels to resist impact from a 4 kg timber at a speed equal to 0.4 design wind speed. In some regions, such as the Karratha area in North WA, the design wind speed for 10000 year return period is 110 m/s, implying the structural panels need be strong enough to resist the impact at a velocity of 44 m/s. This is a substantial increase from the requirement in its previous version, in which the structural panels were required to resist impact from the same 4 kg timber at the velocity of 15 m/s.

This thesis investigates the capacities of oriented strand board (OSB) Skin Structural Insulated Panels (SIP) in resisting windborne debris impacts, and the effectiveness of strengthening techniques on improving the impact resistance of such panels. The primary research tasks include investigating the static and dynamic material properties of oriented strand board (OSB) in current OSB skin SIP and glass fibre laminate for application as a strengthening material, experimental tests of OSB Skin SIP with various strengthening measures subjected to windborne debris impacts; development of high fidelity numerical models to predict responses of SIPs with different strengthening measures to windborne debris impact; and generation of vulnerability curves of SIPs against windborne debris impact.

In this study, various strengthening techniques using different materials and placement at different locations on the panel are considered. The strengthening materials investigated include basalt fibre fabric, glass fibre laminate, basalt fibre mesh and steel wire mesh, which are respectively placed on the front, back, and/or as an interlayer between the OSB skin and EPS core. It is found the basalt fibre fabric has the best strengthening result on the OSB skin SIP. The vulnerability study of the basalt fibre fabric strengthened SIP is carried out through intensive numerical simulations with the verified numerical model. The results demonstrate the panel with this strengthening method can resist higher impact loads, which may lead to application of such strengthening techniques on structural panels in strong wind regions.

# Table of Contents

# Acknowledgements

Firstly, I would like to thank both my Supervisor Prof. Hong Hao and my Co-supervisor Dr. Wensu Chen. Your helpful discussion and supervision greatly contribute to this study. I would never accomplish this thesis without your generous help.

Secondly, I would like to thank my family, my wife Flora and my parents. Thank you for your constant support. It really helps me going through every tough decision and period of time.

I would also like to acknowledge the following people, your contribution and support helped me significantly on study and life. I would never forget these kindness and friendship from all of you. The names are listed alphabetically below.

Ben and Cindy, Bipin Shrestha, Carol Liu and her family, Changhai Zhai, Chao Li, Cheryl Cheng, Chi Zhang, Dagang Lu, Duo Lu, Dylan Pang, Ethan Kang, Frankie Sia, Gang Li, Guigang Tu, Haoran Zuo, Jian Cui, Jianrong Yang, Jun Li, Kairui Ye, Kaiyuan Zhang, Kane Li, Ke Zhou and his family, Kinzang Thinley, Lian A., Ping Liang, Qi Qian, Rosi Yu, Shaoquan Lu and his family, Shenglan Ma, Sucy Leong, Wen Gao, Woo Wu, Xiaochen Guo, Xihong Zhang, Xing Chen, Xingyu Fan, Xuecheng Nian, Yaozong Li and his family, Yifei Hao, Yinghong Lin, Yingqi Liu, Youwen Zhang, Yunfei Bu, Yuan Cheng, Zhejian Li, Zhuo Xu.

Lastly, I would like to acknowledge the financial support from International postgraduate research scholarship (IPRS) and Australian Postgraduate Award (APA) at Curtin University. I would like to acknowledge the financial support from Australian Commonwealth Scientific and Industrial Research Organization (CSIRO) through the project “Climate Adaptation Engineering for Extreme Events Cluster (CAEx)”.

Qingfei Meng

June, 2017

# Primary Publications

This thesis is assembled by publications, either accepted, submitted or in preparation, which form the individual chapters and are listed below.

**Chapter 3**

Meng, Q., Chen, W., Hao, H., Cui, J., Shi, Y., Zhang, X. Failure behaviours of Oriented Strand Board (OSB) material under quasi-static and dynamic loads. Journal of Materials in Civil Engineering, (2017), 30(3), 04017297

**Chapter 4**

Chen, W., Meng, Q., Hao, H., Cui, J., Shi, Y., Quasi-static and dynamic tensile properties of fiberglass/epoxy laminate sheet, *Construction and Building Materials*, 143 (2017) 247-258

**Chapter 5**

Meng, Q., Hao, H., Chen, W. Laboratory test and numerical study of structural insulated panel strengthened with glass fibre laminate against windborne debris impact. *Construction and Building Materials*, 114 (2016) 434-446,

**Chapter 6**

Meng, Q., Chen, W., Hao, H., Numerical and experimental study of steel wire mesh and basalt fibre mesh strengthened structural insulated panel (SIP) against projectile impact. Advances in Structural Engineering, (2017), 1369433217733762.

**Chapter 7**

Meng, Q., Hao, H., Chen, W., Experimental and numerical study of basalt fibre cloth strengthened structural insulated panel under windborne debris impact. *Journal of Reinforced Plastics and Composites*, (2016), Vol. 35(17) 1302–1317

**Chapter 8**

Meng, Q., Chen, W., Hao, H., Vulnerability analyses of OSB skin structural insulated panel strengthened with basalt fibre cloth subjected to windborne debris impact. International Journal of Structural Stability and Dynamics, (2017), 1850088

## Statement of contribution of others

The work presented in this thesis was primarily designed, experimentally executed, interpreted and written by the first author of the individual manuscripts (Qingfei Meng). Contributions by others are described in the following. The signed contribution form is attached in the appendix.

**Chapter 3**

Qingfei Meng carried out the design of the experimental study as part of the PhD study under the supervision of Hong Hao and Wensu Chen. Jian Cui, Yanchao Shi and Xuejie Zhang help to carry out the experiment in Tianjin University. Hong Hao provided the support in Tianjin University and Curtin University. Qingfei Meng was financially supported by the IPRS and APA scholarship. The manuscript was written by Qingfei Meng with contributions from Wensu Chen and Hong Hao, both of whom also provided additional intellectual input in the discussion of the result.

**Chapter 4**

Wensu Chen conducted the design of the experimental study. Qingfei Meng, Jian Cui, and Yanchao Shi carried out the dynamic experiment in Tianjin University. Hong Hao provided the support in Tianjin University and Curtin University. Qingfei Meng was financially supported by the IPRS and APA scholarship. The manuscript was written by Wensu Chen with contributions from Qingfei Meng and Hong Hao, both of whom also provided additional intellectual input in the discussion of the result.

**Chapter 5**

Qingfei Meng and Wensu Chen carried out the experimental study designed by Qingfei Meng, who also carried out the numerical study based on the result of the experimental study as a part of the PhD study project. Hong Hao provided the support in Curtin University. Qingfei Meng was financially supported by the IPRS and APA scholarship. The manuscript was written by Qingfei Meng with contributions from Wensu Chen and Hong Hao, both of whom also provided additional intellectual input in the discussion of the result.

**Chapter 6**

Qingfei Meng and Wensu Chen carried out the experimental study designed by Hong Hao and Wensu Chen. Qingfei Meng carried out the numerical study based on the experimental results as a part of the PhD study project. Hong Hao provided the support in Curtin University. Qingfei Meng was financially supported by the IPRS and APA scholarship. The manuscript was written by Qingfei Meng with contributions from Wensu Chen and Hong Hao, both of whom also provided additional intellectual input in the discussion of the result.

**Chapter 7**

Qingfei Meng and Wensu Chen carried out the experimental study designed by Hong Hao and Wensu Chen. Qingfei Meng carried out the numerical study based on the experimental result as a part of the PhD study project. Hong Hao provided the support in Curtin University. Qingfei Meng was financially supported by the IPRS and APA scholarship. The manuscript was written by Qingfei Meng with contributions from Wensu Chen and Hong Hao, both of whom also provided additional intellectual input in the discussion of the result.

**Chapter 8**

Qingfei Meng carried out vulnerability study of the strengthened panel based on the numerical study in Chapter 7. Hong Hao provided the support in Curtin University. Qingfei Meng was financially supported by the IPRS and APA scholarship. The manuscript was written by Qingfei Meng with contributions from Wensu Chen and Hong Hao, both of whom also provided additional intellectual input in the discussion of the result.

# Other publications during PhD study

Chen, W., Hao, H., Irawan, P., Chen, S., & **Meng, Q**. Experimental investigations of fabric material against projectile impacts. Construction and Building Materials, 104, 142-153. 2016

**Conference papers**

Hao H, Chen W, Chen S, **Meng Q**. Finite Element Analysis of Structural Insulated Panel with OSB Skins against Windborne Debris Impacts (Keynote paper). 1st Pan-American Congress on Computational Mechanics (PANACM), Buenos Aires, Argentina, May 2015.

**Meng, Q.**, Hao, H., & Chen, W. Numerical study of basalt fibre cloth strengthened Structural Insulated Panel under windborne debris impact. Applied Mechanics & Materials, 846. Brisbane, Australia, Sept 2016

Chen, W. S., Hao, H., & **Meng, Q.** Experimental study of steel wire mesh reinforced structural insulated panels against windborne debris impact. In Mechanics of Structures and Materials: Advancements and Challenges (pp. 571-576). CRC Press. Perth, Australia, Dec 2016

# Chapter 1 Introduction

## 1.1 Background

Strong wind events such as cyclones, hurricanes and typhoons are recognized as natural hazard which could cause tremendous damage to buildings. Apart from the wind load itself, impact from windborne debris during windstorms is another potential hazard to building structures.

*Figure 1.1 Damage caused by Hurricane Andrew (1)*

Windborne debris causes damage to buildings. As shown in Figure 1.1, Hurricane Andrew (2) caused enormous damage to the suffered area including the building roof lift-up and structural collapse. The damage pattern is similar to other strong wind events, such as Hurricane Alicia (3) and Hurricane Hugo (4). As observed from wind induced damage, Mehta *et al*. (5, 6) pointed out that the availability of debris in the surrounding area and the resistant capacity of cladding to windborne debris impacts are two primary considerations in wall cladding design. Building envelopes made from metal sheeting or fibre cement, glass windows, roof tiles are especially susceptible to debris impact damage. The increase of internal pressure owing to the creation of building envelop opening, combined with uplift forces acting on the roof, can lead to catastrophic failures (7). In September 1999, Typhoon York caused significant damage to the central business district of Hong Kong. Post windstorm damage investigations have shown that damage caused by windborne debris represents a typical insurance payout cost for windstorm strikes in modern urban areas (8).

*Figure 1.2 Steel skin SIP (L); Oriented Strand Board (OSB) skin SIP (M); Fibre cement skin SIP (R);*

Structural insulated panel (SIP) as shown in Figure 1.2, has been popularly used in Canada, Australia, America and parts of Europe as residential, industrial and commercial building materials in recent twenty years. The SIP has the advantages of fire resistance, thermal insulation, and easily assembled (9). The SIP usually consists of EPS foam core and two skin layers, which are made of various skin materials such as steel sheet, fibre cement board and Oriented Strand Board (OSB). According to the studies by Chen et al. (10-14) and Chen and Hao (15-18), the impact resistance capacities of seven structural panels commonly used in Australian building industry were studied against windborne debris through impact tests and numerical simulations, including the SIPs with different skins. Most of the SIPs with brittle skins experienced localized punch shear failure. It was found that the OSB skin SIP could not survive the debris impact at the required velocity specified in Australia Wind Loading Code (AS/NZS 1170:2:2011) (19) and the critical impact velocity of OSB skin SIP strike by a 4 kg timber debris was only 18 m/s (13, 16, 18). As stipulated in the standard, the wind speed is 110 m/s for 10,000 years return period and 88 m/s for return period of 500 years, implying the structural insulated panel should have the capability to resist 4 kg rod like debris impact at the velocity of 44 m/s under extreme conditions or 35 m/s under normal design condition to be used in the Cyclonic region D. As OSB skin SIP is eco-friendly and the best representative of both current and future SIP built industry, it is chosen in the present study to examine the efficiency of various strengthening measures.

## 1.2 Objective

This study is to investigate the capacities of OSB Skin Structural Insulated Panels in resisting windborne debris impacts, and the effectiveness of various strengthening techniques in improving the impact resistance. In this study, the mechanical properties of the strengthening material including OSB skin and glass fibre laminate under different strain rates are investigated. The numerical models to predict responses of SIPs with different strengthening measures are developed and calibrated. The vulnerability curves are generated to

investigate the impact resistance capacity of the strengthened panel by varying layer thickness, strengthening position and adhesive strength.

## 1.3 Thesis organisation

This thesis comprises nine chapters. Eight chapters are arranged as follows.

Chapter 2 presents literature review on the windborne debris impact on structural insulated panels (SIP) and the related standards and guidelines.

Chapter 3 presents quasi-static and dynamic tensile behaviour of oriented strand board (OSB). The testing results indicated the tensile strength of OSB was sensitive to strain rate. It was found that the damage mode under quasi-static loading condition was different from that under dynamic loading condition. Empirical formula was derived to predict the tensile strength enhancement of OSB material under different strain rates based on the testing results.

Chapter 4 presents quasi-static and dynamic tensile behaviour of glass fibre laminate. The testing results indicated the tensile strength of glass fibre laminate was also sensitive to strain rate. There were no obvious differences between the damage modes in quasi-static test and high strain rate test. Empirical formula was derived to predict the tensile strength of glass fibre laminate material under different strain rates.

Chapter 5 presents the investigations of glass fibre laminate strengthened OSB skin SIPs in both experimental and numerical methods. One unstrengthened and six strengthened SIPs were manufactured and tested by using a pneumatic cannon system. Two high speed cameras were used to capture failure modes and dynamic responses. The effectiveness of glass fibre laminate strengthening was examined and compared in terms of the residual velocity of the projectile. A numerical model was also developed by using LS-DYNA to simulate the laboratory test. The accuracy of the model was calibrated by the test results. The validated numerical model was then used to conduct more numerical simulations to obtain vulnerability curve of strengthened OSB skin SIPs against windborne debris impact.

Chapter 6 presents the investigation of steel wire mesh and basalt fibre mesh strengthened OSB skin SIPs in both experimental and numerical methods. Their impact resistant capacities were identified by comparing damage mode, residual velocity and unpenetrated length of projectile after impact. It was found that the resistance capacity of the OSB skin SIP was enhanced of different levels by applying steel wire mesh and basalt fibre mesh. In addition, finite element model was developed in LS-DYNA to simulate the dynamic response of the SIPs under impact. The accuracy of the numerical model was validated with testing data and the validated model can be used for further

analysis of steel wire mesh and basalt fibre mesh strengthened panels against impact loads.

Chapter 7 presents the experimental and numerical study of SIP with or without basalt fibre cloth strengthening under windborne debris impact. Five specimens with different configurations were tested. The dynamic responses were quantitatively compared in terms of residual speed of debris after impact. The results indicated that basalt fibre cloth enhanced the resistance capacity of SIP. A numerical model was developed in LS-DYNA to simulate the debris impact. The testing results were used to verify the accuracy of the numerical model, which can be used in the subsequent vulnerability study.

Chapter 8 presents the vulnerability analysis of OSB skin SIP strengthened with basalt fibre cloth against windborne debris impact. Using the calibrated numerical model in chapter 7, intensive simulations were conducted to examine the influences of thickness of basalt fibre, location of basalt fibre layer, bonding strength between the basalt fibre fabric and the OSB skin on dynamic responses of basalt fibre cloth strengthened OSB skin SIP. The debris penetration or fracture of the strengthened SIP that creates an opening was defined as failure of the panel in this study. Empirical formulae were derived based on the numerical results to predict the thresholds of penetration velocity and projectile mass that lead to failure of SIP. The empirical formulae can be straightforwardly used to assess the windborne debris impact resistance capacity of basalt fibre cloth strengthened OSB skin SIP.

Chapter 9 summarises the findings in this thesis along with some suggestions for future work.

# Chapter 2 Literature review

## 2.1 Overview

This chapter presents a literature review on the current study of windborne debris impact on structural panels. The literature review includes 1) background of windborne debris impact and impact mechanics; 2) current standards and guidelines; 3) existing study of debris impact on panels; 4) overview of strengthening methods on structural components.

## 2.2 Windborne debris impact and impact mechanics

Strong wind events have caused devastating losses. As reported, Hurricane Bhola recorded as a moderate strength cyclone attacked East Pakistan, which resulted in uncountable economic losses and claimed more than 300,000 lives in 1900s (20). In Queensland and some western part of Australia, strong wind is considered as one of the major natural hazards. During a windstorm, loose objects such as roof tiles, broken tree trunks and gravels might be lifted up and propelled as windborne debris. As shown in Figure 2.1, the high speed wind would carry the debris flying at a high speed and impacting on objects, which would threaten people inside the building if the building envelope is penetrated. Furthermore, the internal pressure will increase as a result of wind blowing through the created opening. The increased internal pressure together with the external pressure and suction, might lead to structural failure such as roof lifting-up and wall collapse.

*Figure 2.1 Windborne debris impact and stayed in the tree after Hurricane Andrew (L) Rod like debris (21); (R) Sheet like debris (22)*

Reports of Hurricane Alicia (3), Hurricane Hugo (4), and Hurricane Andrew (2) also cited windborne debris as a major contributor to loss. Sparks et al.(23) attributed most of the damage to the building envelope to windborne debris. The investigations following Hurricane Andrew highlighted windborne debris as a major cause of property damage (24, 25). Therefore, besides wind pressure on walls and suction on roofs, the windborne debris strike is another

significant threat to the buildings in strong wind regions (26, 27). Based on the potential impact elevations on building envelopes, Minor (28) characterized windborne debris as "small" missiles and "large" missiles that impact the building envelope at high and low elevations, respectively. Wills *et al.* (29) classified windborne debris as particles (e.g., rocks), sheets (e.g., plywood) and rods (e.g., lumber) according to their geometries and aerodynamic properties. Lin *et al.* (30) named the debris as compact-like, plate-like and rod-like debris as shown in Figure 2.2. McDonald (31) found the timber with cross section of 100*50 mm in a mass between 5.4-6.8 kg is the most representative debris in strong wind.

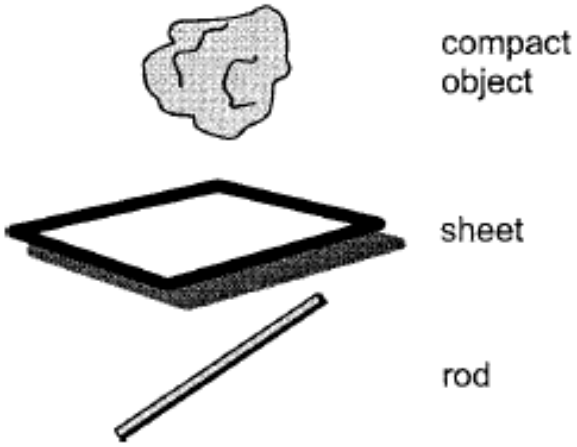


*Figure 2.2 Debris types (30)*

The impact mechanics and structural responses have been reviewed as well. Borvik et al. (32) conducted impact tests on steel plate to investigate its failure mode and multi-stage model was used for analysis. Borvik et al. (33) also conducted impact tests by using different shapes of projectile, the blunt projectile caused a localised shear region on the target, which was verified in (34). Corbett et al. (35) reported that brittle targets experienced shear dominated failure when subjected to blunt projectile impact . Corbett et al. (35) summarized structural responses based on a number of experimental investigations. The impacted plate was found to experience increasing global deformation with the rising impact velocity before reaching the perforation limit. When the perforation limit was reached, further increasing impact velocity resulted in the reduction of global deformation. The impact resistant performance was affected by impact obliquity. Virostek et al. (36) investigated the performances of aluminium and steel plates against projectile impact. It was found that there was slight difference in performance when impact angle was less than 15 degree. As reported by Goldsmith and Finnegan (37), Awerbuch and Bodner (38), and Woodward and Baldwin (39), the obliquity does not significantly affect the ballistic limit of a metal plate when the impact

angle is less than 30 degree. Apart from single layer structures, multi-layered structures subjected to ballistic impact were also investigated. Michelle et al. (40) investigated two types of failure modes of sandwich panels under impact. The key parameters for shear failure include sheet thickness, out of plane shear failure strength, core crushing strength and projectile radius. Marom and Bodner (41) studied multi-layered beam and found it had higher impact resistance capacity than the equivalent weight monolithic beam. Corran et al. (42) observed similar results by investigating impact resistance performance of multi-layered steel sheet and monolithic steel sheet. Radine and Goldsmith (43) conducted experimental study and found that the impact resistance capacity of spaced layers was less effective than the contacted layers subjected to impact load. Hetherington and Rajagopalan (44) revealed that the configuration of rigid front surface and fibre reinforced plastic at back surface was effective to resist projectile penetration. The key parameters determining impact resistant capacity have been identified as projectile mass, speed, angle, shape, momentum, kinetic energy, impact location, failure mode and the configuration of the panels etc.

## 2.3 Existing standards and guidelines

There are some design standards and guidelines available for the design of the structural panels against windborne debris impact as follows.

### 2.3.1 AS/NZS (Australian/New Zealand Standard) 1170.2:2011 (45)

The impact loading from windborne debris is specified in the AS/NZS 1170.2:2011. Where windborne debris loading is required for impact resistance testing, the debris impact loading shall be: (a) a timber member of 4 kg mass with a nominal cross-section of 100 mm × 50 mm impacting end on at 0.4 $V_R$ for horizontal trajectories and 0.1 $V_R$ for vertical trajectories; and (b) Spherical steel ball 8 mm diameter (approximately 2 grams mass) impacting at 0.4 $V_R$ for horizontal trajectories and 0.3 $V_R$ for vertical trajectories where $V_R$ is the regional wind speed. It is also stated that these two test debris items are representative of a large range of windborne debris of varying masses and sizes that can be generated in serve wind storms.

For the specific cyclonic area such as Cyclone C and D areas, the wind speed is 110 m/s for 10,000 years return period and 88 m/s for return period of 500 years. According to the AS/NZS 1170.2:2011, the structural panels should have capacity to resist 4 kg timber debris impacting velocity at 44 m/s horizontally under extreme conditions or 35 m/s under normal design conditions.

### 2.3.2 FEMA (US Federal Emergency Management Agency) (46)

According to FEMA 320, the missile used to determine impact resistance is defined as 6.8 kg (15 lb.) timber with cross section of 50.8 mm (2 in.) × 101.6

mm (4 in.) at 160.9 km/h (100 mph) horizontally and 107.8 km/h (67 mph) Vertically.

### 2.3.3 SBC (US Standard Building Code) (47)

The SBC SSTD-12 (47) requires large missile impact test to verify the performance of structural panels against windborne debris impact. The test requirements are given as follows:

1) Three specimens are required to be tested.

2) Each specimen is to be impacted twice: one at the centre within an area of 78.5 $mm^2$ and the other one within an area of 113.1 $mm^2$ from corner.

3) The typical large missile is a 4.08 kg (9 pounds) lumber with cross section of 50.8 mm (2 in.) × 101.6 mm (4 in.) at 54.7 km/h (34 mph).

4) A porous specimen passes the test if it can resist missile impacts without penetration. A non-porous specimen is acceptable if it resists the large missile impact with no opening forming through which a 3 mm diameter sphere can pass.

5) All three specimens must pass the test.

### 2.3.4 FBC (Florida Building code) (48)

According to the FBC, the large missile impact test requirements are given as follows:

1) Entire assembled units are to be subjected to a 50.8 mm (2 in.) × 101.6 mm (4 in.) lumber weighing 4.08 kg (9 pounds) impacting at a speed of 15.2 m/s (50 feet per second), representing hurricane conditions in Florida.

2) Three specimens are required to be tested.

3) Each of three identical specimens is to receive two impacts, i.e. one near the centre and one near the corner.

4) The system is acceptable if all three specimens reject the missile impacts without penetration.

## 2.4 Existing studies on structural panels against impact

There are some existing studies on commonly used structural panels in Florida (49). The projectile impact testing was performed to gain a better understanding of the performances of the panels under the impacts from windborne debris. Based on the test results, a list of wall and roof assemblies that passed the FBC test (48) was given. However, the above tests only considered the typical panels used in Florida and the tests were performed according to the criterion in the Florida Building Code (48). Therefore, the

results could not be extrapolated to determine the impact resistant capacity of the current studied panels.

In Australia, Ginger *et al*. (50) presented a summary of work carried out in the area of wind and structural engineering, with the aim of mitigating wind induced damage of domestic housing. Frye *et al*. (51) studied the realistic impact speeds of objects with varying shapes and sizes and quantified the potential damage subjected to different missile mass and velocity. In addition, the response of a metal cladding wall system was studied subjected to static loading and dynamic impact loading. Chen et al. (10-14) and Chen and Hao (15-18) reported the impact resistance capacities of seven structural panels and envelops commonly used in Australian building industry through impact tests and numerical simulations, including the SIPs with different skins against windborne debris. Most of the SIPs with brittle skins experienced localized punch shear failure.

There are also some other studies on the debris impact on structural panels. Braden and Scheer studied the performance of the public and commercial building subjected to large projectile impact (52, 53). Fernandez *et al*. (54) presented an experimental investigation of the performance of metal shutter systems designed to protect windows from windborne debris. It was found that the deflection of the metal panel window protection system was highly sensitive to impact location, debris type and impact orientation.

### 2.4.1 Experimental method

Some testing facilities have been utilized to investigate impact resistance capacity of the structural components such as drop weight, pendulum, catapult, and pneumatic cannon impact system (55-59). Drop weight test is an experimental method to study the dynamic response of panels under low velocity impact. Wang *et al*. (60) performed low-velocity impact tests with a drop weight impact tower. The energy levels varied by altering the drop height of the impactor. Load time history of each impact event was measured by a KISTLER force transducer. A high speed oscilloscope was used to acquire and record the data during the impact. Found *et al*. (61, 62) used a drop-weight impact rig to study the behaviour of CFRP panel. The hemispherical impactor with 12 mm diameter was released by an electromagnetic switch from a height of 0.5 m for which the impact velocity was measured at approximately 3 m/s. Mines *et al*. (63) used a drop mass to drive a penetrator into the centre of panel. Azrul (64) performed drop weight tests on RC beams and panels without or with different CFRP strengthening schemes.

According to the testing guidelines in AS/NZS, SBC, FBC and FEMA and the previous study carried out in US and Australia, the pneumatic cannon impact system were used to test the impact resistance capacity of the structural panel. At the University of Florida, a large missile cannon used compressed air to

propel a large missile to hit the test panels (49). Chen et al. (10-14) and Chen and Hao (15-18) used a pneumatic cannon system as shown in Figure 2.3 to generate windborne debris impact in Australia. The halogen lights were used to provide sufficient light for the high speed camera and the steel frame was used to provide a stable boundary for the SIP specimens subjected to the impact.

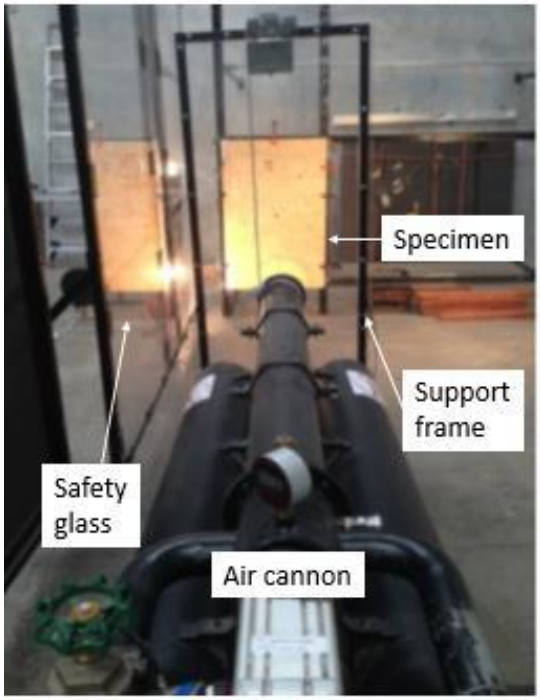


*Figure 2.3 Typical pneumatic cannon impact test system (10, 11, 13-18)*

### 2.4.2 Numerical method

Numerical simulation is also used to study impact response of structural panel. In the previous study, Chen et al. (10-14) and Chen and Hao (15-18) used commercial software LS-DYNA to simulate the impact response of structural panels. Herbin *et al*. (65, 66) derived fragility curves of aluminium storm shutters subjected to windborne debris impact based on the calibrated models. Croop and Lobo (67) presented guidelines for model selection of foams to simulate their behaviours in LS-DYNA. MAT 163 is usually used for the simulation of EPS foam which exhibits rate dependency. Eight node solid element is usually used to model core element (i.e., honeycomb) and Belytschko-Tsay shell element is commonly used for modelling the composite skin (68-70). S/R Hughes–Liu shell element is another option to model the thin layer element (71). Zhou and Stronge (72) meshed all parts of the sandwich panel, including skin layers and the core layer by using 4-node axisymmetric bilinear elements. A finer mesh is usually required at the impact location of panels to better capture the deformation and penetration damage (69). An appropriate erosion criterion is important for numerical analyses and modelling (73). The contacts between each sandwich panel layers are defined as either

perfect bonding or bonding with a certain tensile and shear strength. For example, Azrul (64) simulated debonding between concrete slab and CFRP sheet for CFRP strengthened RC panel under drop weight impacts. Debonding failure was well predicted as compared to testing results. A half or a quarter of panel model was created to save computational time in many numerical studies owing to symmetry (68, 71).

The physical testing can demonstrate the overall structural response straightforwardly. However, it has some shortcomings related to cost, equipment, time and safety. Moreover, the reproducibility of test results is not always ensured due to the uncertainties involved in test, and the test results often cannot be extrapolated, which greatly limit the applicability of the testing results. On the other hand, reliable numerical simulation overcomes the above shortcomings. It can be used to simulate physical tests and better study the structural dynamic responses. It allows more detailed observations and calculations of structural responses, e.g. predictions of the distributions of internal stress and strain of structures that are difficult to be measured in the tests. Furthermore the internal deformation and failure that are often difficult to obtain from physical tests, but are easily calculated in numerical simulations. With the development in computer technology and computational mechanics, more and more physical tests can be and have been performed by numerical tests, as evidenced in many reports and literature. However, physical tests cannot be abolished, which are needed to calibrate the numerical model. Only a proven numerical model can be used to simulate physical tests and study the dynamic responses of structures. Then the calibrated numerical models can be used to undertake intensive parametric study to identify the effects of parameters on the structural response.

## 2.5 Overview of strengthening technique on the structural components

According to the regional design wind speed ($V_R$), the projectile impact velocity could be over 40 m/s in the region D defined in AS/NZS (19) with $V_R$ more than 100 m/s under the extreme wind condition. As the structural components cannot meet the requirement in Australian wind loading code (45). The strengthening is necessary to increase the impact-resistant capacity of the structural components.

Triantafillou (74) strengthened the reinforced concrete (RC) beam with FRP, and proved FRP as an effective technique to improve the shear resistance of the RC beam. FRP laminate strengthening was also reported as an effective method to enhance the capacities of RC structures to resist blast (75-77) and impact loadings. It was also found that epoxy-bonded FRP laminate was effective in strengthening masonry structure components (78). Meng and Werasak (79) found that applying glass fibre laminate could enhance the

mechanical performance of the structural insulated panels under compressive loads. Mousa et al.(80) strengthened the sandwich panels by using Carbon Fibre Reinforced Plastic (CFRP) and found that both strength and ductility of the strengthened panel increased by conducting bending test. Mohotti et al.(81) found the polyurea coating was effective to reduce the residual velocity of projectile and increase energy absorption ability of the panel. Wu et al. (82) tested concrete columns strengthened with CFRP and BFRP. The BFRP strengthened columns were found to have comparable capacities with CFRP strengthened columns in terms of shear resistance and energy dissipation capacity. Lopresto et al. (83) carried out tests on plastic laminates strengthened by basalt fibre and e-glass fibre. It was found that the basalt fibre composite had higher tensile strength, compressive strength and flexural strength than glass fibre composite.

As a commonly used construction material, steel wire mesh was also considered in this study to enhance the resistance capacity of the structural panel owing to the advantages of low-cost and lightweight. Nie et al.(84) strengthened RC beams with steel wire mesh and found that the flexural load carrying capacity and stiffness were improved as compared to the non-strengthened beam. Huang et al.(85) investigated the steel wire mesh strengthened T-type beam and found that both the flexural bearing capacity and the stiffness of the beam increased. Kamal and Eltehewy (86) investigated the concrete panel strengthened by steel wire mesh and reported that the use of steel wire mesh could effectively mitigate the response of the panel. Ibrahim (87) found the steel wire mesh reinforced concrete slab had higher ultimate load capacity as compared to the non-strengthened slab. Kumar and Patel (88) found that it was effective to use steel wire mesh to enhance the axial strength of the column. Gao et al.(89) studied the steel wire mesh strengthened concrete tube and found the compressive behaviour of strengthened specimen was enhanced. Li et al. (90) used steel wire mesh to strengthen the concrete slab. It was found the steel wire mesh reinforcement provided additional spall and crater resistance and effectively reduced the perforation damage under blast. Fibre mesh has also been studied. Shaheen et al. (91) used fibreglass mesh and steel wire mesh to strengthen ferrocement beams. It was reported that the beam strengthened with glass fibre had a lower crack loading capacity, and the beam strengthened with welded wire meshes exhibited better structural behaviour than other specimens.

## 2.6 Summary

In this chapter, the background about windborne debris impact and its impact on structural insulated panels is briefly reviewed. Both experimental and numerical studies on the dynamic response of the panel subjected to windborne debris impact are presented. To meet with the requirement of the wind loading code, strengthening on the panel is applied to achieve a higher

impact resistance capacity. The strengthening techniques on the structural components are also reviewed for potential strengthening methods in this study. In summary, this thesis is aimed to propose new strengthening methods onto the SIP to resist windborne debris impact, which might benefit SIP industry in future for producing strong panels for applications in strong wind regions.

***The [Meng Q, Chen W, Hao H, Cui J, Shi Y, Zhang X. Failure Behaviors of Oriented Strand Board Material under Quasi-Static and Dynamic Loads. Journal of Materials in Civil Engineering. 2017 Dec 20;30(3):04017297.] is unable to be reproduced here due to copyright restrictions.***

***The [Failure Behaviors of Oriented Strand Board Material under Quasi-Static and Dynamic Loads] can instead be accessed via [https://ascelibrary.org/doi/abs/10.1061/(ASCE)MT.1943-5533.0002172]***

# Chapter 4 Quasi-static and dynamic tensile properties of glass fibre laminate sheet

## 4.1 Introduction

Fibre composite as a high-performance engineering material has been widely used due to its high stiffness and strength. Glass fibre laminate composite can be made from different glass fibre reinforcements in the forms of unidirectional, woven, multiaxial and chopped strand mat in various matrix such as epoxy, polyester or phenolic (130). Thermo-laminated woven fiberglass/epoxy material, as one of glass fibre laminate materials, is made from woven glass fibre fabric impregnated with epoxy resin binder, which is manufactured under pressure and heat. The glass fibre laminate has the advantages of high mechanical strength, good corrosion resistance, sound flame resistance and humidity resistance etc. This type of laminate composite can be used in a variety of applications including insulating structural parts in electrical equipment, vehicle and boat structure, marine structure, pressure vessel, container, gas pipe, aerospace structure, and civil engineering structure etc. (131). During the service life, fiberglass/epoxy laminate or structures strengthened by fiberglass/epoxy laminate might be subjected to dynamic loadings such as impact and blast. For instance, the fiberglass/epoxy laminate material was applied as an interlayer of structural insulated panel for improving the structural performance against windborne debris impact (98). As reported in (130), a shock wave with the velocity of 1~10 m/s on a structure can generate a strain rate of between 100 $s^{-1}$ and 1000 $s^{-1}$ near the impacted location. Therefore, understanding the dynamic behaviours of fiberglass/epoxy laminate material under different strain rates is of significance for reliable predictions of its responses subjected to dynamic loadings.

G10 and FR-4 (FR represents Fire Retardant) laminate material are two commonly used fiberglass/epoxy laminate materials. The commercially available laminate sheet has the thickness in the range of 0.1 mm to 76 mm. G10 and FR-4 laminate have almost the same mechanical properties except that the epoxy resin of FR-4 contains flame retardant. G10/FR-4 fiberglass/epoxy composite can be manufactured into sheet, tube and rod. Some studies have been carried out to investigate the mechanical properties of the fiberglass/epoxy laminate (G10/FR-4). Naderi and Khonsari (132) investigated the fatigue failure of fiberglass/epoxy (G10/FR-4) laminate by conducting tension–tension and bending fatigue tests. The finding can be used to assess the severity of degradation of the specimen and predict fatigue life. Liakat and Khonsari (133) applied thermographic approach to study the fatigue behaviour of fiberglass/epoxy (G10/FR-4) composite laminate by conducting uniaxial tension–compression and fully-reversed bending fatigue tests at different stress levels and loading ratios. Whisler and Kim (134) investigated

the effect of impactor radius on the low velocity impact resistance of plain weave fiberglass/epoxy (G10/FR-4) composite panels. It was found that the impactor radius significantly affected the damage. Herranena et al. (135) assumed the FR-4 glass fibre laminate as an isotropic and linear material in the numerical simulation. It can be concluded that the study on the dynamic mechanical properties of G10/FR-4 fiberglass/epoxy laminate sheet material is still lacking in the literature. However, some studies have been conducted with regard to the strain rate effect on the mechanical properties of glass fibre laminate material, which can be used as references.

In the previous studies, contradictory results were reported with respect to the strain rate effect on the mechanical properties such as strength, failure strain and Young's Modulus. For example, some studies (130, 131, 136-142) reported the existence of strain rate effect on the material while others (143-148) presented that strain rate has marginal effect on the material properties. Barre, Chotard (130) studied the strain rate effect on the tensile dynamic mechanical properties of glass fibre reinforced phenolic and polyester resins. It was found that the elastic modulus and the strength were strain rate dependent. Reis, Coelho (131) found that glass fibre reinforced polymer was strongly affected by strain rate with the strain rate between 0 and 1.6E-03 $s^{-1}$. Ochola et al.(136) revealed that glass fibre reinforced polymer had strain rate effect on the compressive strength when the strain rate was between $10^{-3}$ to 450 $s^{-1}$. Davies and Magee (137) reported that the glass reinforced plastic was sensitive to strain rate and the dynamic increase factor was 1.55 over the strain rate from $10^{-3}$ to $10^{3}$ $s^{-1}$. Staab and Gilat (138) studied the ply fiberglass/epoxy and found that the mechanical response characteristics were strain rate sensitive. Welsh and Harding (139) studied the laminates properties at strain rate up to 700 $s^{-1}$, and found an increase of both the tensile strength and elastic modulus. Schoßig et al. (140) studied the glass fibre reinforced plastics and revealed the positive correlation between the tensile stress and the strain rate. Harding and Welsh (141) tested the woven glass fibre/epoxy composite at strain rate from quasi-static to 1000 $s^{-1}$. It was found that the dynamic modulus and strength were 2.5 times of the static values in the 0 degree direction (with tensile axis parallel to the principle reinforced direction) and 1.7 times of the static values in the 45 degree to the principle reinforced direction. The increase of material strength was related to the different failure modes. It was also found that strain rate effect was influenced by fibre reinforcement architecture. The dynamic elastic modulus was 2.5 and 2 times of the static modulus for the plain-weave and satin-weave fiberglass/epoxy laminate, respectively. The mechanical properties were also affected by the fibre reinforcement orientation and the specimen size. Landel and Nielsen (149) reviewed and summarized previous researches on some polymer and composite material. Unlike the isotropic material, the mechanical properties of glass fibre laminate were depended on the woven orientation of the fibres.

Wisnom (150) investigated the effects of specimen size on the mechanical properties of unidirectional glass fibre/epoxy material. The size effect on tensile failure was found in both tensile and flexural tests. The strength of laminates decreased with the increase in specimen size. Harding (151) reported two types of woven fiberglass/epoxy materials in compression up to 860 $s^{-1}$ using cylindrical and thin strip specimens. It was revealed that there was a significant increase in the initial modulus, strength and ultimate strain with increasing strain rate for woven fiberglass/epoxy composites. Shokrieh and Omidi (152) investigated tensile properties of unidirectional fiberglass/epoxy composites under different strain rate of 0.001–100 $s^{-1}$. The results revealed that the tensile strength increased significantly with the strain rate but the tensile modulus and the failure strain increased moderately with the strain rate.

However, other studies found the strain rate has marginal effect on dynamic properties of glass fibre laminate. Daniel and Liber (143) found that strain rate had no influence on the material properties such as the longitudinal elastic modulus of fiberglass/epoxy laminate. Lifshitz (144) reported that the initial modulus and failure strain of the angle ply fiberglass/epoxy laminates were insensitive to the strain rate and the dynamic strength was 20%~30% higher than the static value. Armenakas and Sciammarella (145) presented that the ultimate strength of unidirectional fiberglass/epoxy specimens had a decreased trend with the increasing strain rate. Hou and Ruiz (146) found that the tensile strength and modulus of woven carbon fibre reinforced laminate were independent of strain rate. Belingardi and Vadori (147) carried out the low speed impact test on the glass fibre composite, no sensitivity between the mechanical characteristics and strain rate was found. Okoli and Smith (148) found that Poisson's ratio of fiberglass/epoxy laminate was insensitive to strain rate when the strain rate is between $10.6*10^{-3}$ and 2.72 $s^{-1}$. It was inferred that the absence of strain rate sensitivity on Poisson's ratio was due to the presence of fibres in the laminate. Ou and Zhu (153) studied the tensile behaviours of glass fibre/epoxy laminate composite at different strain rates from quasi-static up to 160 $s^{-1}$. The results revealed that tensile strength, maximum strain and toughness of the material were sensitive to strain rate while Young's Modulus was insensitive to strain rate. The above reviews reveal that there is no general consensus yet on the strain rate effects on fibre materials. The difference on strain rate effects observed by different researchers might be due to the types of material (fibre and matrix) (143, 146, 148, 153), fibre structural effect (144, 145), interaction between the reinforcement and the matrix (139), testing condition, specimen type, specimen size, quality in preparing specimen and testing procedures and equipment (131), etc.

The above review indicates that the strain rate effect is highly dependent on the type of fibre glass composite. There is no study on the strain rate effects of the fiberglass/epoxy laminate in literature yet. In this chapter, tensile tests on fiberglass/epoxy laminate were carried out under both the quasi-static and intermediate loading rates. The dynamic material properties of glass fiber laminate were investigated with strain rate up to 115 $s^{-1}$. The damage modes and testing results were recorded and compared. The strain rate effects on the tensile strength and failure strain of the fiberglass/epoxy laminate were examined. Empirical formulae were proposed to predict the tensile strength, failure strain and Young's Modulus under different strain rates based on the testing results.

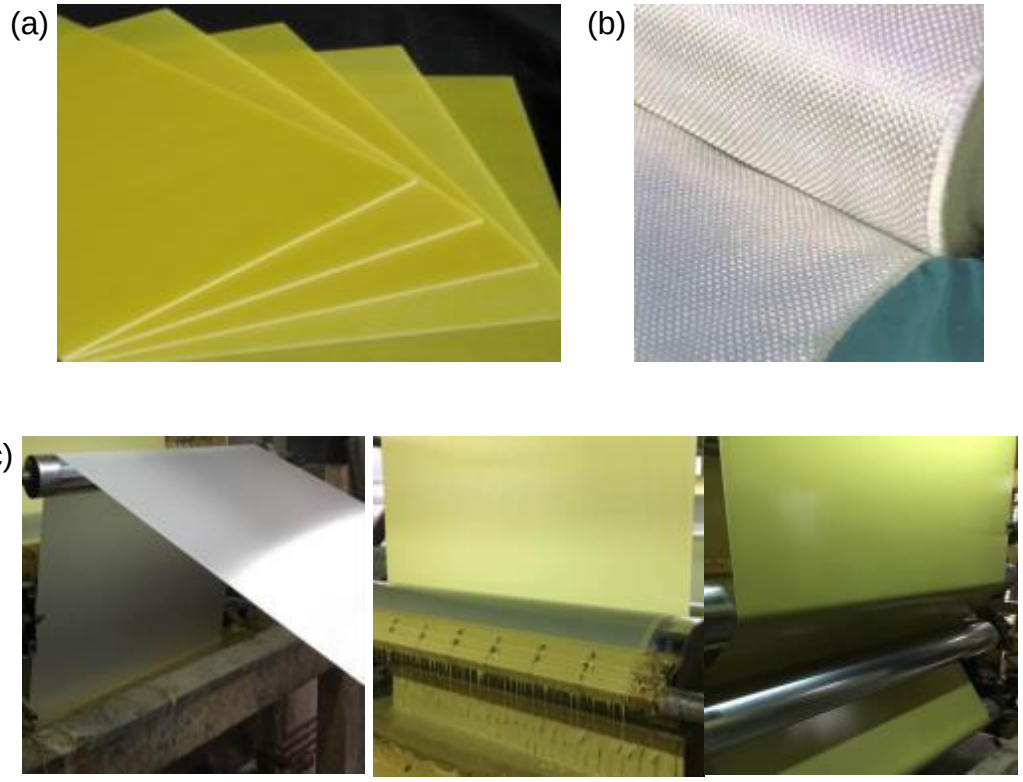


*Figure 4.1 (a) Photograph of fiberglass/epoxy laminate sheet; (b) Fiberglass fabric layer; (c) Manufacturing process of fiberglass fabric layer impregnated with epoxy resin*

## 4.2 Testing specimens

In this study, the fiberglass/epoxy laminate sheet (G10/FR-4) as shown in Figure 4.1(a) was tested. The fiberglass/epoxy laminate (G10/FR-4) with thickness of 1mm was made from five layers of woven glass fabric impregnated with epoxy resin binder under pressure and heat. The density of glass fiber laminate sheet is about 2.0 g/$cm^3$. The epoxy resin binder is made of Bisphenol-A-Epoxy resin with the weight of around 45%. The woven glass fabrics made from continuous filament fibre with the diameter between 10~30 $\mu m$ were stacked in layers. The warp and weft directions of fabric are called lengthwise (0 degree) and crosswise (90 degree), respectively. The manufacturing procedure is presented in Figure 4.1(c). The tensile strength of

the laminate (G10/FR-4) was around 240 MPa, which was provided by the supplier.

### 4.2.1 Quasi-static testing specimens

The quasi-static tensile specimens were designed as per the guideline ASTM-D638 (154), which stipulates the requirement of tensile testing. The fiberglass/epoxy laminate sheet was cut into dumbbell-shaped specimens. Figure 4.2 shows the dimensions of the quasi-static tensile specimen. The total length of the specimen was 165 mm and the width of the holder was 20 mm. The length and the width of the gauge section were 65 mm and 13 mm, respectively. The reduced section outside the gauge section with radius 76.5 mm was placed to avoid stress concentration.

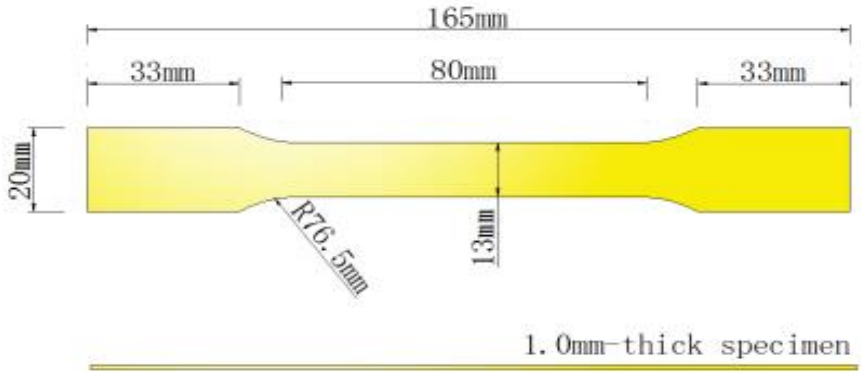


*Figure 4.2 Schematic diagram of the quasi-static and low velocity tensile specimen (mm)*

### 4.2.2 Dynamic testing specimens

To meet with the specific requirements for using the INSTRON® VHS 160/100-20 system, the dimension of dumbbell-shaped specimens were adjusted as shown in Figure 4.3. The total length was changed to 450 mm and the two ends had different length. The upper end had a longer length of 300 mm, which ensured the upper jaw of the actuator to move and grip the specimen when the desired speed was obtained. The other end had a shorter length of 70 mm, which was fixed to the lower jaw. The width of ends and gauge section were kept as 20 mm and 13 mm, respectively. The gauge length was shortened to 60 mm, which reduced the time required for a stress wave to propagate through the gauge length to better achieve dynamic stress equilibrium. In addition, the shortened gauge could increase the testing range of strain rate. For each crosshead speed, at least three specimens were tested. A total of 34 specimens were prepared for the dynamic tensile tests.

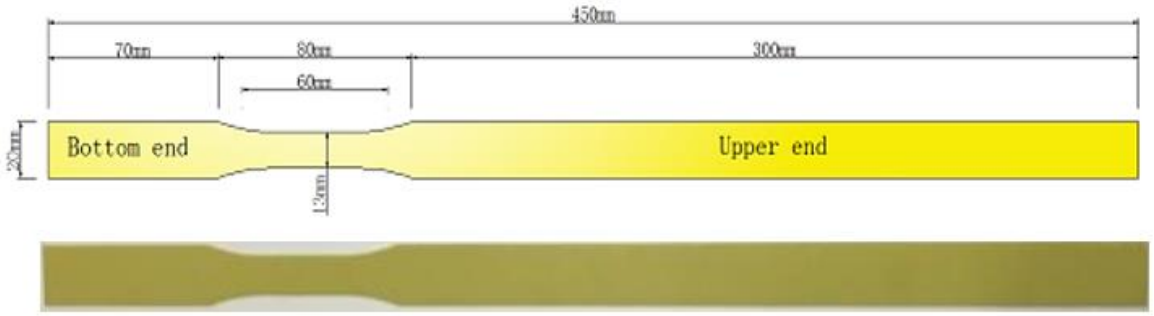


*Figure 4.3 Schematic diagram of the dynamic tensile specimen (mm)*

## 4.3 Testing facilities and setup

### 4.3.1 Quasi-static test


*Figure 4.4 Quasi-static testing set-up (L) Shimadzu® AGS-300kNX; (R) Epsilon® Extensometer*

As shown in Figure 4.4(L), a servo hydraulic machine i.e. Shimadzu AGS-300kNX universal testing machine was used to carry out the quasi-static and low velocity tensile test in this study. The Shimadzu AGS- 300kNX Series universal testing machine had the load capacity of 300 kN and the crosshead speed range of 0.001 to 500 mm/min. The constant-rate strain of the machine was controlled by using non-backlash precision ball-screw drive. An inbuilt load cell was installed in the machine to measure the tensile load. The room temperature was around 15℃± 5℃ during the test. The crosshead measurement included the deformation from gauge section, deformation from part of the upper and bottom ends and the slippage between the grip and the specimen. Therefore, an extensometer was deployed to measure the elongation of the gauge length of the specimen for strain calculation as shown in Figure 4.4 (R). Nine crosshead speeds (i.e. 0.1, 0.5, 1, 5, 10, 50, 100, 250 and 500 mm/min) were applied for quasi-static and low velocity tensile tests. The difference in strain rate between the extensometer measurement and the

crosshead measurement was negligible at quasi-static and low velocity tests. The strain rates were calculated by dividing the crosshead speed and the gauge length of 80 mm. The results are given in Table 4.1.

### 4.3.2 Dynamic test

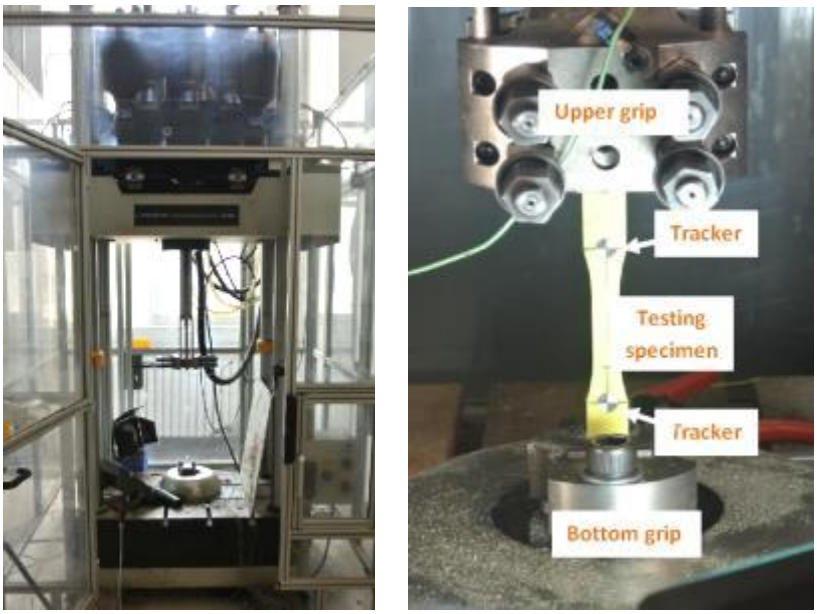


*Figure 4.5 (L) Photograph of INSTRON® VHS 160/100-20; (R) Tensile testing setup*

A variety of techniques such as Charpy pendulum (for strain rate up to 100 $s^{-1}$), conventional screw driven load frame (for strain rate up to 1 $s^{-1}$), drop weight impact system (for strain rate up to 100 $s^{-1}$), high speed servo-hydraulic machine (for strain rate up to 100 $s^{-1}$) and SHPB system (for strain rate 100~3000 $s^{-1}$) were used to investigate material dynamic properties (114, 115, 130, 155-157). The test of strain rate effect on glass fibre laminate material requires constant loading speed during the dynamic testing course. It was difficult for the drop weight impact system and pendulum impactor system to keep a certain constant loading speed during the dynamic testing process. In this study, dynamic tensile tests were carried out by using high speed servo-hydraulic machine, i.e. INSTRON® VHS 160/100-20 as shown in Figure 4.5. The room temperature was around 25℃± 5℃ during the test. A high speed camera Fastcam was positioned beside the Instron testing machine along with halogen light source LeiYing™ M-300G to capture the failure procedures and trace the trackers for the strain calculation. The frame rate of 30,000 fps was used for the high speed camera in the testing. Testing data was recorded by using INSTRON® VHS software. The INSTRON® VHS 160/100-20 machine used servo-hydraulic control technologies to provide constant strain rate at high velocities for tensile tests. The machine had the capability of providing stable velocity in the range of 0.1 m/s to 25 m/s. As indicated in the previous studies (114, 115), the machine was able to maintain a satisfactory constant velocity profile when the crosshead speed was up to 20 m/s. Therefore, the crosshead velocity used in the study varied

from 0.5 m/s to 20 m/s. The corresponding strain rate can be calculated based on the formula $\dot{\varepsilon} = V / L$, where $V$ is the constant velocity and $L$ is the specimen gauge length. Six crosshead speeds (i.e. 0.5, 1, 5, 10, 15, 20 m/s) were applied for dynamic testing. The corresponding theoretical and actual strain rates were calculated as provided in Table 4.2. The theoretical strain rate was derived from the above relationship. It was found that the theoretical strain rates were higher than the actual strain rates, as shown in Figure 4.6. The actual strains were measured via tracing the trackers from the video clips captured by the high speed camera. The actual strain rate was calculated by linear fitting the slope of the strain time histories as shown in Figure 4.7. As shown in Figure 6 of a tested case the theoretical strain rate was around 125 $s^{-1}$, which was higher than the actual strain rate of 54.06 $s^{-1}$. The difference in strain rate obtained from the two approaches might be due to the slippage between the grip and the specimen. The deformation of the upper end and the bottom end of the specimen also contributed to the strain difference, which made the actual deformable length of the specimen longer than the gauge length. Therefore, the strain rate calculated by using the gauge length likely overestimates the true strain rate of the specimen.

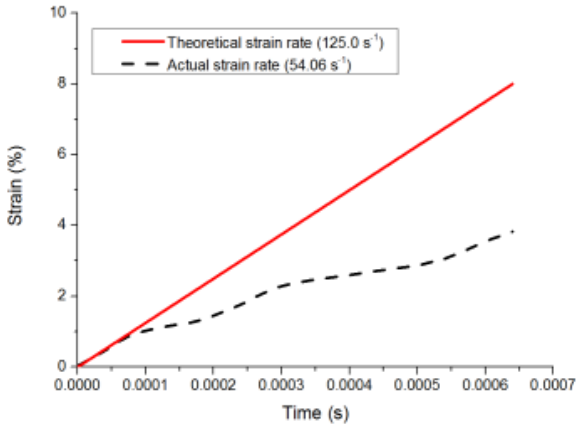


*Figure 4.6 Strain time histories (theoretical strain rate vs. tracker measurement from high speed camera clip)*

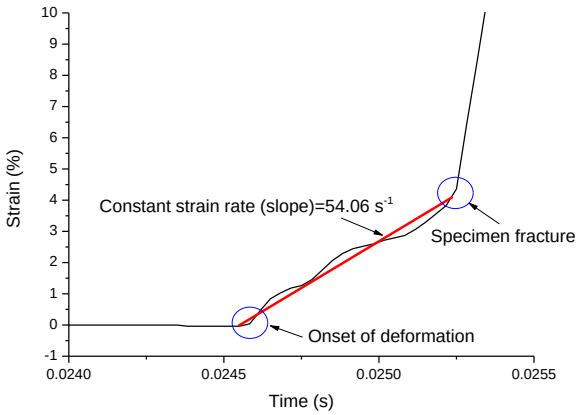


*Figure 4.7 Strain time history derived by the trackers (from high speed camera clip) at the strain rate of 54.06 $s^{-1}$*

## 4.4 Tensile testing results

### 4.4.1 Quasi-static test results

A total of 34 specimens under nine extension rates were tested. Figure 4.8 shows the typical failure patterns of four specimens (i.e. #4, #12, #16 and #34) at quasi-static and low velocity tests. As observed, the specimens experienced the fracture failure occurred at either end or both ends of the gauge. Similar failure pattern was also observed in (140) in testing the fiberglass/epoxy reinforced thermoplastic material. The fractures occurred at gauge ends were due to stress concentration or unavoidable loading eccentricity effect.

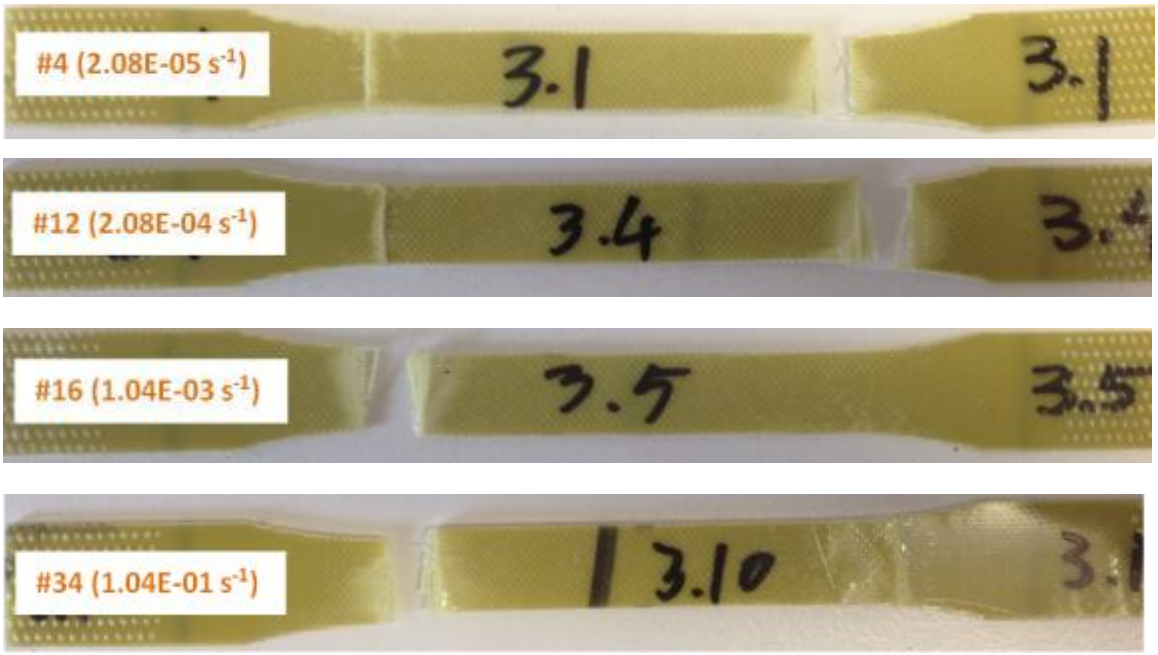


*Figure 4.8 Failure patterns after quasi-static and low velocity tensile tests*

Figure 4.9 shows the stress-strain curves in the quasi-static and low velocity tests. The specimen showed approximately linear elastic behavior before the brittle failure. It was found that Young's Modulus of the specimen decreased slightly at each strain rate due to the initial damage and delamination of fiber and/or epoxy after loading. Based on the quasi-static and low velocity testing results, the tensile strength, failure strain and Young's Modulus at quasi-static (i.e. strain rate of 2.08E-05 $s^{-1}$) were calculated as 258.94 MPa, 2.24% and 11.60 GPa, respectively. When the strain rate reached 2.08E-02 $s^{-1}$(#27), the tensile strength increased to 320.06 MPa and the corresponding failure strain increased to 2.96%. Figure 4.10 shows the mean tensile strength of the specimen under quasi-static and low velocity tests with standard deviation. It shows apparent dependence of tensile strength on the strain rate at low strain rate. The complete results in terms of failure strength, failure strain and Young's Modulus are given in Table 4.1.

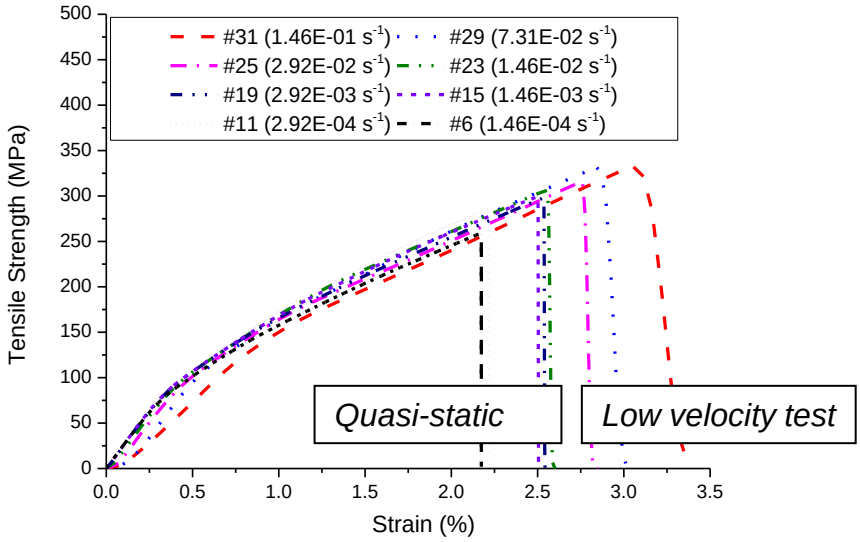


*Figure 4.9 Stress-strain curves of quasi-static and low velocity testing*

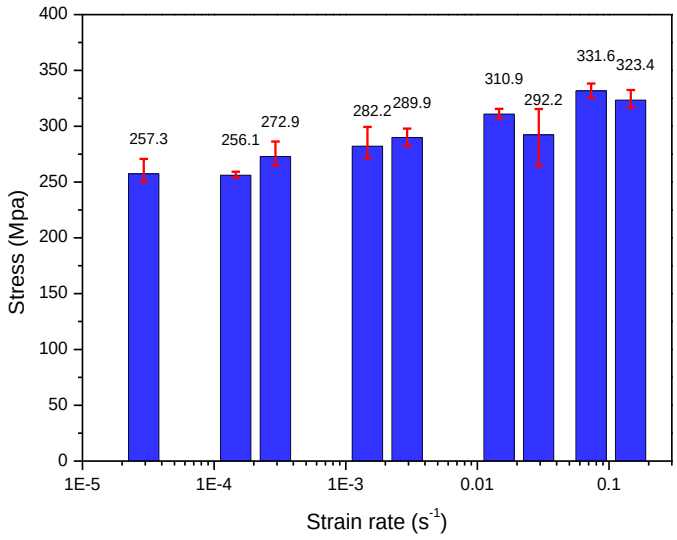


*Figure 4.10 Testing summary of tensile strength in the quasi-static and low velocity tests*

*Table 4.1 Specimen configurations and results in the quasi-static and low velocity tests*

| No. (#) | Crosshead speed | Stain Rate | Width | Peak Load | Failure Strength | Failure Strain | Young's Modulus | DIF of failure strength |
|---|---|---|---|---|---|---|---|---|
| | mm/min | $s^{-1}$ | mm | kN | MPa | % | GPa | |
| 1 | 0.1 | 2.08E-05 | 13.0 | 3.52 | 271.71 | 2.42 | 11.21 | 1.05 |
| 2 | 0.1 | 2.08E-05 | 13.0 | 3.25 | 250.15 | 2.09 | 11.94 | 0.97 |
| 3 | 0.1 | 2.08E-05 | 13.0 | 3.26 | 250.46 | 2.06 | 12.12 | 0.97 |
| 4 | 0.1 | 2.08E-05 | 13.0 | 3.43 | 263.44 | 2.36 | 11.15 | 1.02 |
| 5 | 0.5 | 1.04E-04 | 13.0 | 3.31 | 255.16 | 1.99 | 12.78 | 0.99 |
| 6 | 0.5 | 1.04E-04 | 13.0 | 3.37 | 259.05 | 2.18 | 11.84 | 1.00 |
| 7 | 0.5 | 1.04E-04 | 13.0 | 3.30 | 253.75 | 2.01 | 12.62 | 0.98 |

| | | | | | | | | |
|---|---|---|---|---|---|---|---|---|
| 8 | 0.5 | 1.04E-04 | 12.9 | 3.57 | 276.74 | 2.61 | 10.60 | 1.07 |
| 9 | 1 | 2.08E-04 | 12.9 | 3.72 | 287.55 | 2.23 | 12.87 | 1.11 |
| 10 | 1 | 2.08E-04 | 13.1 | 3.48 | 266.36 | 2.03 | 13.11 | 1.03 |
| 11 | 1 | 2.08E-04 | 13.1 | 3.45 | 263.55 | 2.11 | 12.43 | 1.02 |
| 12 | 1 | 2.08E-04 | 13.1 | 3.44 | 263.13 | 2.31 | 11.37 | 1.02 |
| 13 | 5 | 1.04E-03 | 13.1 | 3.89 | 297.48 | 2.51 | 11.80 | 1.15 |
| 14 | 5 | 1.04E-03 | 13.0 | 3.53 | 270.39 | 2.19 | 12.33 | 1.04 |
| 15 | 5 | 1.04E-03 | 13.0 | 3.59 | 276.14 | 2.28 | 12.10 | 1.07 |
| 16 | 5 | 1.04E-03 | 13.0 | 3.58 | 275.60 | 2.48 | 11.10 | 1.06 |
| 17 | 10 | 2.08E-03 | 13.0 | 3.87 | 297.23 | 2.55 | 11.64 | 1.15 |
| 18 | 10 | 2.08E-03 | 13.1 | 3.67 | 280.76 | 2.42 | 11.57 | 1.08 |
| 19 | 10 | 2.08E-03 | 13.0 | 3.77 | 288.67 | 2.44 | 11.79 | 1.11 |
| 20 | 10 | 2.08E-03 | 13.0 | 3.99 | 305.90 | 2.84 | 10.74 | 1.18 |
| 21 | 50 | 1.04E-02 | 13.0 | 3.99 | 306.83 | 2.56 | 11.93 | 1.18 |
| 22 | 50 | 1.04E-02 | 13.0 | 4.10 | 315.61 | 2.78 | 11.33 | 1.22 |
| 23 | 50 | 1.04E-02 | 13.1 | 4.03 | 308.87 | 2.73 | 11.27 | 1.19 |
| 24 | 50 | 1.04E-02 | 13.1 | 3.77 | 288.82 | 2.62 | 11.00 | 1.12 |
| 25 | 100 | 2.08E-02 | 13.1 | 4.10 | 313.58 | 2.76 | 11.32 | 1.21 |
| 26 | 100 | 2.08E-02 | 13.0 | 3.86 | 296.48 | 2.44 | 12.13 | 1.14 |
| 27 | 100 | 2.08E-02 | 13.1 | 4.18 | 320.06 | 2.96 | 10.80 | 1.24 |
| 28 | 250 | 5.21E-02 | 13.1 | 4.40 | 336.38 | 3.02 | 11.09 | 1.30 |
| 29 | 250 | 5.21E-02 | 13.1 | 4.31 | 329.70 | 2.86 | 11.51 | 1.27 |
| 30 | 250 | 5.21E-02 | 13.0 | 4.23 | 325.13 | 2.91 | 11.14 | 1.26 |
| 31 | 500 | 1.04E-01 | 13.0 | 4.18 | 321.46 | 2.95 | 10.86 | 1.24 |
| 32 | 500 | 1.04E-01 | 13.0 | 4.12 | 317.39 | 2.84 | 11.14 | 1.23 |
| 33 | 500 | 1.04E-01 | 13.0 | 4.32 | 331.45 | 3.07 | 10.78 | 1.28 |
| 34 | 500 | 1.04E-01 | 13.0 | 4.16 | 319.02 | 2.96 | 10.77 | 1.23 |

### 4.4.2 Dynamic tensile test results

#### 4.4.2.1 Validation of testing results-dynamic stress equilibrium

In quasi-static testing, the stress wave had plenty of time to propagate forth and back inside the specimen to achieve stress equilibrium during the load application. However, in dynamic testing, the loading rate was much faster than that in quasi-static testing. The stress wave might not have enough time to travel through the specimen to reach stress equilibrium. Therefore, sufficient number of stress reverberations inside the specimen before failure was needed to achieve stress equilibrium. As suggested in the study (158), stress wave should have enough time to travel back and forth inside the specimen for at least three times. The speed of stress wave was calculated by using the equation $c=\sqrt{\frac{E}{\rho}}$, where E= Elastic modulus of fiberglass/epoxy laminate; $\rho =$ Density of fiberglass/epoxy laminate. The time required for stress wave to travel one way can be calculated as $t = L / c$, where L= gauge length of specimen, c= speed of stress wave. In this study, the elastic modulus of fiberglass/epoxy laminate at quasi-static test was about 11.6 GPa and the density was about 2.0 g/cm3. The velocity of stress wave in fiberglass/epoxy laminate material was calculated as 2350 m/s, which required 34 $\mu s$ to travel through the testing gauge. When the strain rate was up to 115 $s^{-1}$, the specimen fractured at around 313 $\mu s$, which allowed stress wave travelling through and back the specimen for around five times. Therefore the testing data was valid since the stress equilibrium was reached.

#### 4.4.2.2 Failure patterns

A total of 22 specimens under six crosshead speeds were tested. Figure 4.11 shows the failure patterns of the specimens at five strain rates of 5.81 $s^{-1}$, 28.25 $s^{-1}$, 85.2 $s^{-1}$, 104 $s^{-1}$, and 115 $s^{-1}$. The specimen failed at the adjacent region between testing gauge and the transition part. When the strain rate is less than 92 $s^{-1}$, most of the specimens experienced localized fracture occurred on either end of the gauge section. The delamination of the specimen was not observed. When the strain rate increased, most of the specimens experienced multiple breaks on both ends of the test gauge, which was also observed in (140). The specimen experienced fiber rupture along with some delamination. More damages such as delamination and diagonal cracks were extended to a larger area, which resulted in the increase of tensile strength of material. It can be concluded that the increase of tensile strength is heavily affected by the damage modes. In addition, at a high strain rate, the specimen had no time to initiate the failure at internal defects and weak points or stress concentrated areas. These multiple failures in the specimen require more energy to cause the damage, hence results in strength increment. By contrast, at a low strain rate the specimen had relatively longer time to develop the failure along the weaker section.

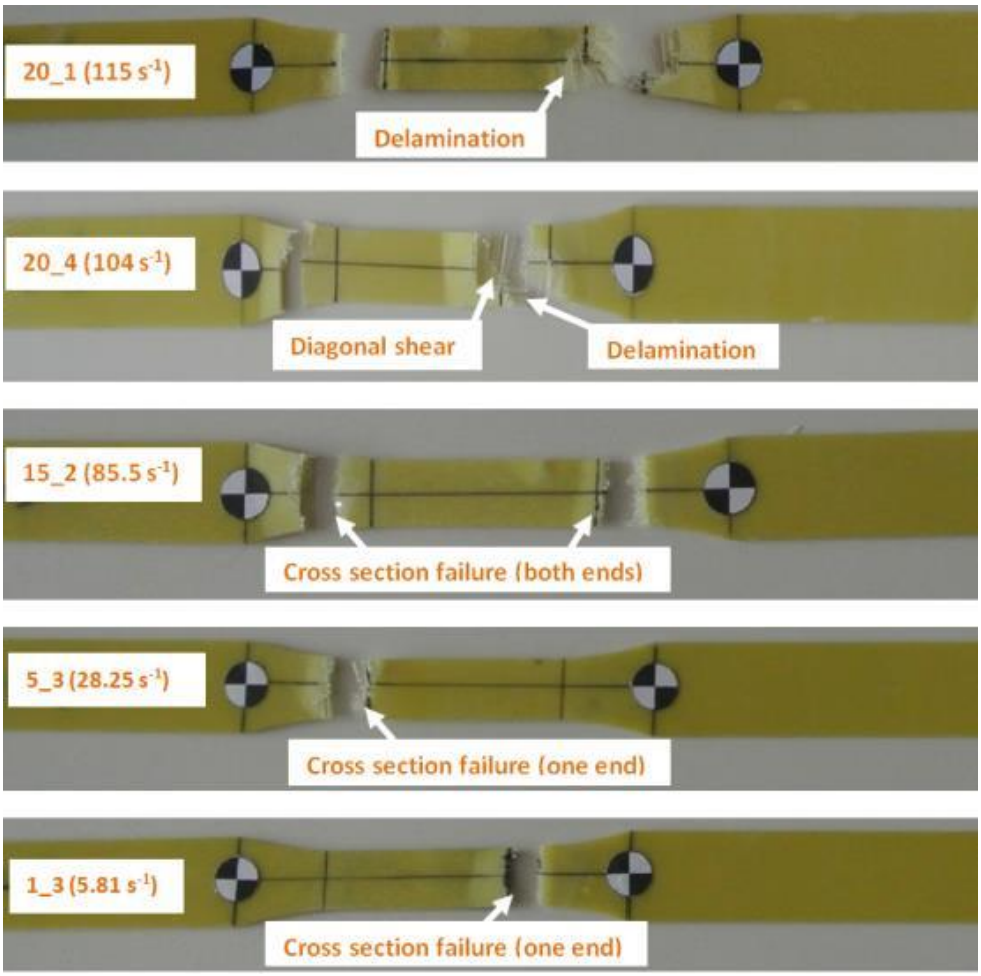


*Figure 4.11 Failure patterns after dynamic tensile tests (at the strain rates of 5.81 $s^{-1}$, 28.25 $s^{-1}$, 85.2 $s^{-1}$, 104 $s^{-1}$, 115 $s^{-1}$)*

Figure 4.12 shows typical load time histories at various strain rates. The loads were measured by the inbuilt load cell. It is apparent that the tensile strength of the specimen is strain rate sensitive. The representative stress-strain curves of the specimen at different strain rate in the high velocity tensile testing are shown in Figure 4.13. The specimen shows nonlinear behavior at high strain rate, which is due to the fluctuation of the stress caused by the vibration of the Instron machine. The Young's modulus is taken as the slope of the stress-strain curve from the origin to the failure point in this study. At the strain rate of 2.88 $s^{-1}$, the tensile strength is 316.58 MPa and the failure strain is 3.35%. The tensile strength and failure strain increase with the increasing strain rate. When the strain rate increases to 105.02 $s^{-1}$, the tensile strength rises to 423.40 MPa and the failure strain is 4.15%, which indicates the increments of 33.9% and 23.9%, respectively. The detailed testing results are given in Table 4.2.

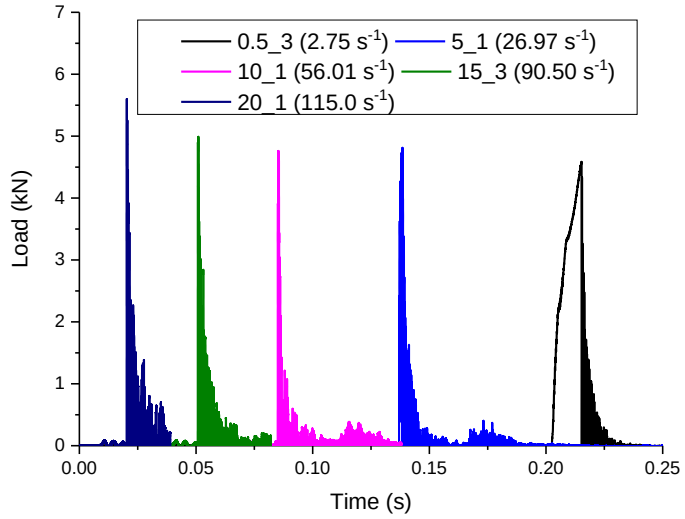


*Figure 4.12 Load time histories at various strain rates*

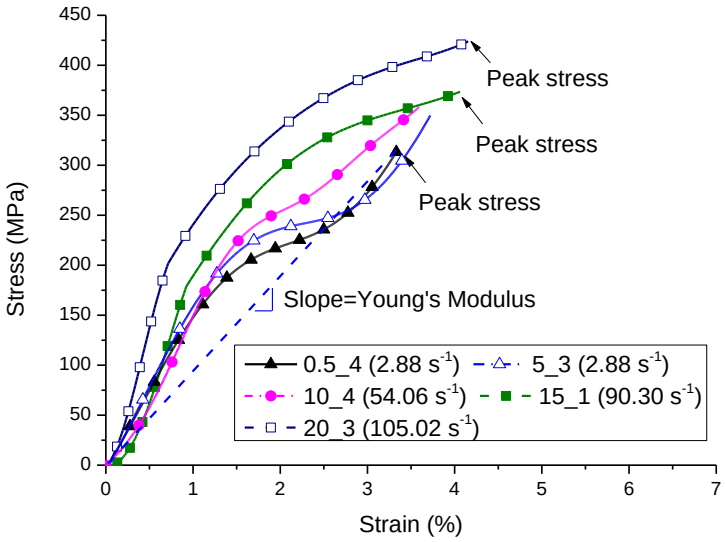


*Figure 4.13 Representative stress-strain curves at different strain rates*

*Table 4.2 Specimen configurations and testing results in the high-speed tests*

| No. | Actuator Speed | Theoretical Stain Rate | Actual Stain Rate | Coupon Width | Peak Load | Failure Strength | Failure Strain | DIF of failure strength |
|---|---|---|---|---|---|---|---|---|
| | m/s | $s^{-1}$ | $s^{-1}$ | mm | kN | MPa | % | |
| 0.5_1 | 0.5 | 6.25 | 2.89 | 12.9 | 4.44 | 343.46 | 3.37 | 1.33 |
| 0.5_2 | 0.5 | 6.25 | 2.87 | 13.0 | 4.41 | 338.22 | 3.37 | 1.31 |
| 0.5_3 | 0.5 | 6.25 | 2.75 | 13.1 | 4.59 | 350.72 | 3.49 | 1.35 |
| 0.5_4 | 0.5 | 6.25 | 2.88 | 13.0 | 4.11 | 316.58 | 3.35 | 1.22 |
| 1_1 | 1 | 12.50 | 5.67 | 13.0 | 4.46 | 342.90 | 3.72 | 1.32 |
| 1_2 | 1 | 12.50 | 5.87 | 13.1 | 3.86 | 294.15 | 3.17 | 1.14 |
| 1_3 | 1 | 12.50 | 5.81 | 12.9 | 4.55 | 351.62 | 3.65 | 1.36 |
| 5_1 | 5 | 62.50 | 26.97 | 13.1 | 4.49 | 343.65 | 3.75 | 1.33 |

| | | | | | | | | |
|---|---|---|---|---|---|---|---|---|
| 5_2 | 5 | 62.50 | 28.66 | 13.1 | 4.65 | 355.59 | 3.58 | 1.37 |
| 5_3 | 5 | 62.50 | 28.25 | 13.0 | 4.62 | 353.94 | 3.72 | 1.37 |
| 5_4 | 5 | 62.50 | 28.35 | 13.0 | 4.63 | 356.98 | 3.63 | 1.38 |
| 10_1 | 10 | 125.00 | 56.01 | 13.1 | 4.33 | 330.70 | 3.65 | 1.28 |
| 10_2 | 10 | 125.00 | 54.04 | 13.1 | 4.46 | 341.81 | 3.73 | 1.32 |
| 10_4 | 10 | 125.00 | 54.06 | 13.0 | 4.65 | 357.48 | 3.61 | 1.38 |
| 15_1 | 15 | 187.50 | 90.30 | 13.0 | 4.78 | 367.92 | 3.98 | 1.42 |
| 15_2 | 15 | 187.50 | 85.50 | 13.1 | 4.62 | 354.11 | 3.97 | 1.37 |
| 15_3 | 15 | 187.50 | 90.50 | 13.1 | 4.89 | 374.20 | 4.06 | 1.45 |
| 15_4 | 15 | 187.50 | 91.12 | 13.0 | 4.93 | 379.50 | 3.52 | 1.47 |
| 20_1 | 20 | 250.00 | 115.00 | 13.1 | 5.58 | 426.90 | 3.97 | 1.65 |
| 20_2 | 20 | 250.00 | 104.60 | 13.2 | 5.64 | 428.40 | 4.24 | 1.65 |
| 20_3 | 20 | 250.00 | 105.02 | 13.0 | 5.52 | 423.40 | 4.15 | 1.64 |
| 20_4 | 20 | 250.00 | 104.00 | 13.0 | 5.60 | 431.03 | 4.16 | 1.66 |

## 4.5 Analysis and discussion

### 4.5.1 Strain rate effect on tensile strength

Figure 4.14 shows the tensile strength of the specimen increases with strain rate. The quasi-static tensile strength is around 258.94 MPa and the tensile strength steadily increases with strain rate under quasi-static status and low strain rates less than 30 $s^{-1}$. When the strain rate is over 30 $s^{-1}$, the specimen experiences significant increase in strength with the strain rate. The tensile strength at strain rate of 104.6 $s^{-1}$ is about 428.4 MPa, showing an increment of 65%. The strength increment is caused by more energy dissipated by multiple failures at high strain rate. The relationship between the tensile strength and strain rate is log-linear when the axis of strain rate is scaled using logarithmic value with base 10 (i.e. $\log_{10}\varepsilon$). Based on the test data, a logarithmic bi-linear relationship between the tensile strength and strain rate is fitted. The similar relationship can be also found in other studies of fibre laminate material (115, 130, 141, 159). The dynamic tensile strength can be predicted by using the following empirical formulae.

$$\sigma_{Dynamic} = \sigma_{Static}(14.1log_{10}\varepsilon + 325.2) \quad when\ 10^{-5} < \varepsilon < 30s^{-1} \tag{4. 1}$$

$$\sigma_{Dynamic} = \sigma_{Static}(63.2log_{10}\varepsilon + 251.4) \quad when\ 30 < \varepsilon < 115s^{-1} \tag{4. 2}$$

where $\varepsilon$ is the strain rate.

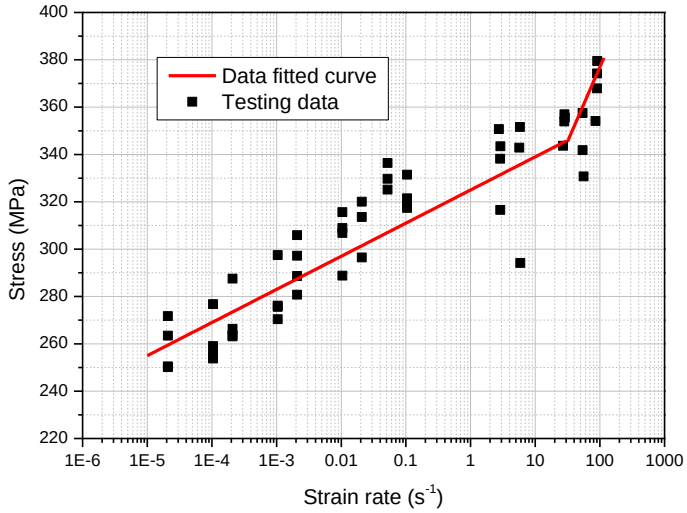


*Figure 4.14 Tensile strength vs. strain rate*

### 4.5.2 Strain rate effect on failure strain

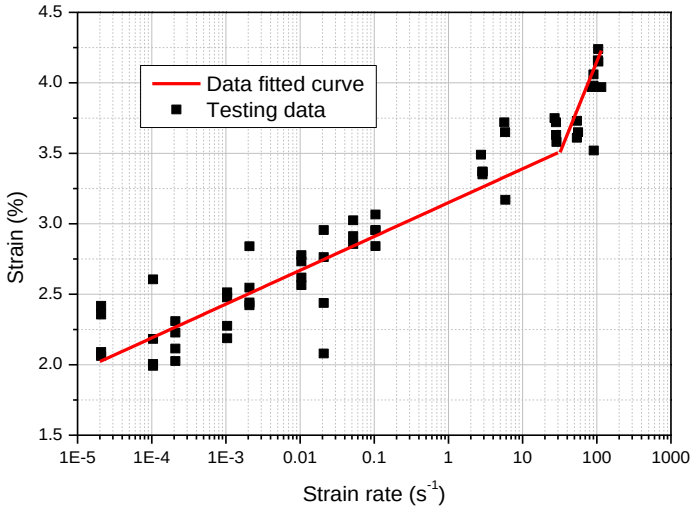


*Figure 4.15 Failure strain vs. strain rate*

Figure 4.15 shows the failure strain at various strain rates. The failure strain at quasi-static loading is around 2.24%. It is found that the failure strain is less sensitive to strain rate when the strain rate is less than 30 $s^{-1}$. The failure strain shows a significant increase with increasing strain rate when the strain rate is over 30 $s^{-1}$. For instance, when the strain rate reaches 104.6 $s^{-1}$, the failure strain is 4.24%, with an increment of 89.3 % comparing with the failure strain at quasi-static status. The empirical formulae to predict the failure strain of material are given below.

$$\varepsilon_{Dynamic} = \varepsilon_{Static}(0.24log_{10}\varepsilon + 3.15) \quad when\ 10^{-5} < \varepsilon < 30s^{-1} \tag{4.3}$$

$$\varepsilon_{Dynamic} = \varepsilon_{Static}(1.305log_{10}\varepsilon + 1.557) \quad when\ 30 < \varepsilon < 115s^{-1} \tag{4.4}$$

where $\varepsilon$ is the strain rate.

### 4.5.3 Dynamic increase factor and empirical formulae

The increment of tensile strength at different strain rates can be represented as dynamic increase factor (DIF), which is defined as dividing dynamic tensile strength over quasi-static tensile strength at strain rate 2.08E-05 $s^{-1}$ in this study. The DIF of tensile strength is about 1.6 at the strain rate 115 $s^{-1}$. Available testing data on glass fiber laminate by other researchers including Harding and Welsh (141), Davies and Magee (137), Shokrieh and Omidi (152), Reis, Coelho (131) and Barre, Chotard (130) in the literature were compared herein. As observed, the tensile strength of glass fiber laminates was of different levels due to different glass fiber laminates were tested in the studies. Figure 4.16 presents the DIF of tensile strength as a function of strain rate. The DIF trend of the specimen is consistent with most previous testing data on glass fiber laminate (130, 131, 137, 141) although the strength in (137) has a large variation, which is possibly due to the quality in preparing the specimens. However, the DIF reported by Shokrieh and Omidi (152) showed the glass fiber was less sensitive to strain rate at lower strain rate but remarkably strain rate dependent when the strain rate was over 20 $s^{-1}$. The difference of material behavior can be explained by the structural effect of fiber types. The unidirectional fiberglass/epoxy composite studied in (152) showed less strain rate sensitivity than the woven fiberglass/epoxy composite in this study at low strain rate range. The DIF for dynamic tensile strength of the glass fiber laminate can be predicted by using the following empirical formulae and the DIF curves are fitted with all the available data.

$$DIF_{\sigma} = 0.045log_{10}\varepsilon + 1.28 \quad when\ 10^{-5} < \varepsilon < 30s^{-1} \tag{4.5}$$

$$DIF_{\sigma} = 0.551log_{10}\varepsilon + 0.53 \quad when\ 30 < \varepsilon < 115s^{-1} \tag{4.6}$$

where $\varepsilon$ is the strain rate.

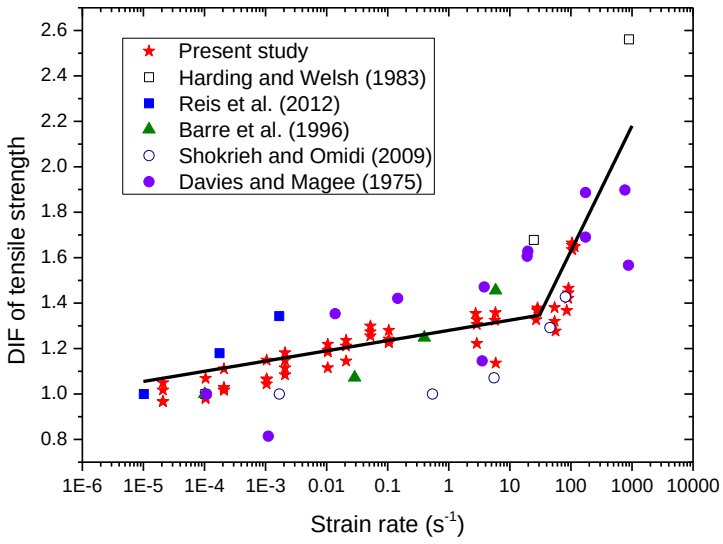


*Figure 4.16 DIF of tensile strength vs. strain rate*

The failure strain of the glass fibre laminate material increases with the strain rate in the current study. The ratio of dynamic failure strain to static failure strain ($\frac{\varepsilon_d}{\varepsilon_s}$) was compared with the testing data reported by other researchers such as Harding and Welsh (141), Shokrieh and Omidi (152), and Ou and Zhu (153). Harding and Welsh (141) observed a steady increase of failure strain at the strain rate from $10^{-4}$ to 800 $s^{-1}$. However, Shokrieh and Omidi (152) reported insignificant strain rate effect on the failure strain at the low strain rate range ($10^{-3}$~6 $s^{-1}$), which might be due to the size effect. It was found that the specimens in (152) had much less gauge length of 12.7 mm and the width of 12.7 mm than the specimens in other studies. The existence of fewer defects in smaller specimen resulted in more consistent failure strain at low strain rate range. Ou and Zhu (153) revealed the strain rate had significant effect on the failure strain (3~3.5 times) when the material was subjected to high strain rate. The discrepancy is probably because different type of glass fiber laminate material was tested. The specimen tested in (153) has tensile strength of 700 MPa and Young's Modulus of 44 GPa while the corresponding parameters in this study are 258.94 MPa and 11.60 GPa, respectively. The results indicate the strain rate effect is more significant for the glass fiber laminate material with higher strength. Figure 4.17 presents the ratio $\frac{\varepsilon_d}{\varepsilon_s}$ as a function of strain rate. The relationship between $\frac{\varepsilon_d}{\varepsilon_s}$ and strain rate can be expressed by the following empirical formulae.

$$\frac{\varepsilon_d}{\varepsilon_s} = 0.077 log_{10}\varepsilon + 1.504 \quad when\ 10^{-5} < \varepsilon < 30 s^{-1} \tag{4.7}$$

$$\frac{\varepsilon_d}{\varepsilon_s} = 1.605 log_{10}\varepsilon - 0.755 \quad when\ 30 < \varepsilon < 115 s^{-1} \tag{4.8}$$

where $\varepsilon$ is the strain rate.

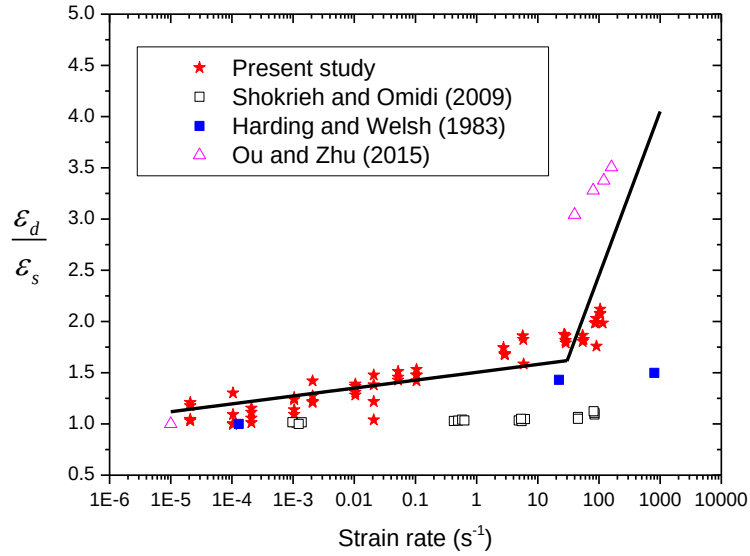


*Figure 4.17 Ratio of dynamic to static failure strain ($\frac{\varepsilon_d}{\varepsilon_s}$) vs. strain rate*

The ratio of dynamic Young's Modulus to static Young's Modulus ($\frac{E_d}{E_s}$) is also compared herein with the available data (143, 152, 153). The ratio $\frac{E_d}{E_s}$ as a function of strain rate is presented in Figure 4.18. The Young's Modulus shows a decreasing trend with the increase of strain rate in the low strain rate range, which indicates a similar trend with the testing data reported by Ou and Zhu (153) and Daniel and Liber (143). As explained by Ou and Zhu (153), that the quasi-static Young's Modulus is higher than the dynamic one might be due to the facts that different testing machines were used or the failure strains at quasi-static were much less than those at dynamic loading. However, Young's Modulus reported by Shokrieh and Omidi (152) did not show strain rate dependence at low strain rate range. Again, the smaller specimen size had less defects, which resulted in more consistent performance at low strain rate range. When the strain rate went higher than 30 s$^{-1}$, the Young's Modulus remarkably increased with the increasing strain rate. A similar trend of the Young's Modulus with the strain rate higher than 30 s$^{-1}$ can be found from the data (152, 153). The relationship between $\frac{E_d}{E_s}$ and strain rate can be expressed by the following empirical formulae.

$$\frac{E_d}{E_s} = -0.0238 log_{10}\varepsilon + 0.898 \quad when\ 10^{-5} < \varepsilon < 30 s^{-1} \tag{4.9}$$

$$\frac{E_d}{E_s} = 0.555 log_{10}\varepsilon - 0.023 \quad when\ 30 < \varepsilon < 1000 s^{-1} \tag{4.10}$$

where $\varepsilon$ is the strain rate.

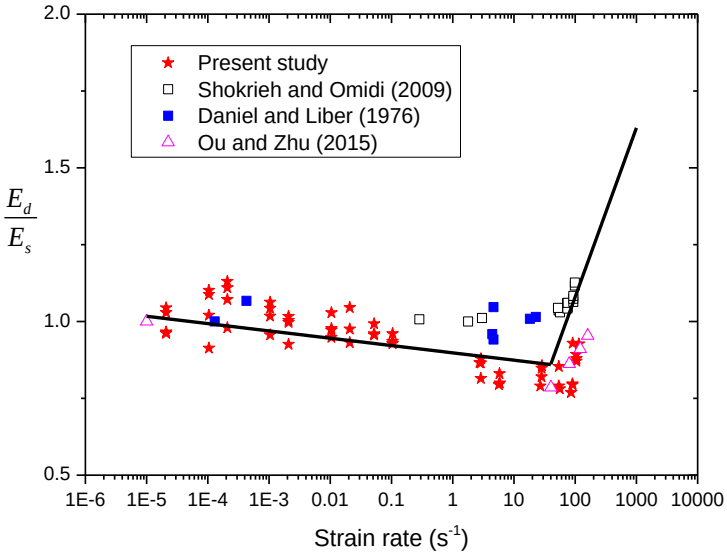


*Figure 4.18 Ratio of dynamic to static Young's Modulus* $\frac{E_d}{E_s}$ *vs. strain rate*

## 4.6 Summary

The quasi-static and dynamic properties of fiberglass/epoxy laminate were experimentally investigated in this chapter. The specimens were tested at strain rate up to 115 $s^{-1}$. It was found that fiberglass/epoxy laminate was sensitive to the strain rate in terms of tensile strength, failure strain and Young's Modulus. The strain rate effect was demonstrated by the failure patterns at different strain rates. The fractures at either end or both ends of the gauge section, delamination and diagonal cracks were observed in the quasi-static, low velocity and high velocity tests. The logarithmic bi-linear relationships between the tensile strength/failure strain and strain rate were proposed based on the testing data. Empirical formulae were derived to predict the tensile strength and failure strain of the fiberglass/epoxy laminate under different strain rates.

# Chapter 5 Experimental and numerical study on the glass fibre laminate strengthened structural insulated panel against windborne debris impact

## 5.1 Introduction

The dynamic properties of glass fibre laminate have been investigated in the previous chapter. Glass fibre laminate is a light weight, strong and robust material(160). Kawata et al.(161) found the impact absorption capacity of GFRP is higher than CFRP. Sun et al.(162) reported that protective covering with epoxy adhesive interlayers can effectively protect concrete against projectile impact. As shown in Figure 5.1, glass fibre laminate is a composite material by impregnating the glass fibre with epoxy resin under proper pressure and heat. However, there is no study that has been reported in the open literature of using glass fibre laminates to strengthen structural insulated panels to improve the impact resistance capacities of the panel, and no study of the performance of glass fibre laminate to strengthen OSB skin SIPs subjected to windborne debris impact.

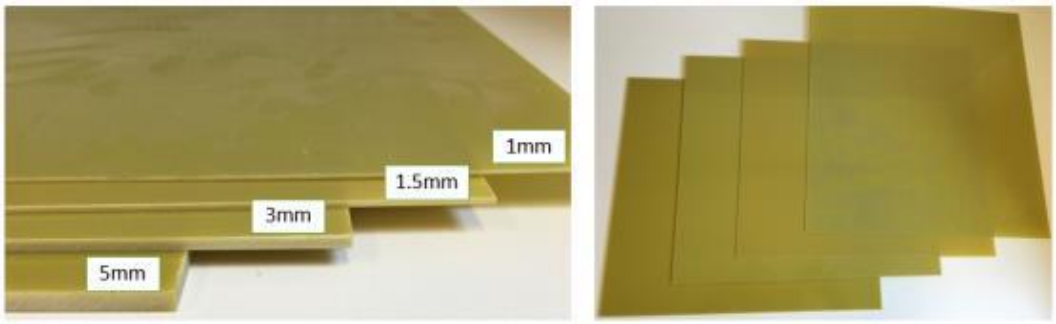


*Figure 5.1 Photograph of glass fibre laminate*

This chapter studies the performance of glass fibre laminate strengthened OSB skin SIPs against windborne debris impact. Six strengthened SIPs and one referencing panel without strengthening were subjected to a 4 kg timber projectile impact at the velocity ranging between 18 m/s and 40 m/s. Structural response of the panel was captured by two high speed cameras in the front and back sides. The damage modes and the residual velocity of the projectile after each strike were recorded and analysed. In addition, a numerical model was developed to simulate the SIP subjected to projectile impact by using commercial software LS-DYNA. The numerical model was calibrated with the data acquired from the laboratory test. By using the calibrated numerical model, the glass fibre laminate strengthened SIP subjected to various projectile impacts were simulated and analysed. The calibrated numerical model is then used to carry out intensive numerical simulations to study the performance of strengthened SIPs with OSB skins subjected to impacts of windborne debris with different weights and impact velocities.

## 5.2 Experimental investigation

A total of seven specimens (i.e. A/B/C/D/E/F/G) were tested by using a pneumatic cannon system. The damage modes of the panels and the residual velocity of projectile were recorded with two high speed cameras. The schematic view of specimens and experimental setup are given below.

### 5.2.1 Description of the specimens

All the tested SIPs used in this study have the same dimension of 1200*800*120 mm. The non-strengthened specimen A, which is a commercially available SIP, includes an EPS foam core and two OSB sheets as the skin layers. Figure 5.2 shows the schematic views of the two strengthening methods of the commercial SIP. In this study, four specimens B/C/D/G are strengthened by applying a single layer of glass fibre laminate sheet between the OSB skin and EPS core as a strengthening interlayer, as shown in Figure 5.2 (M). Another two specimens (i.e., E/F) are strengthened by two layers of glass fibre laminates inserted between the OSB skins and EPS core, as illustrated in Figure 5.2 (R). The thicknesses of the strengthened glass fibre laminates are 1mm, 1.5mm, 3mm, and 5mm respectively as detailed in Table 5.1. The tensile strength of the glass fibre laminate is 200 MPa and the mass density is 1900 kg/m$^3$. The EPS foam, OSB skins and glass fibre laminates are glued together by using waterproof epoxy with bonding strength of 6-7 MPa (16). Figure 5.2 also shows the photos specimens being prepared for the tests, which was done by a commercial SIP manufacturer.

The detailed material properties of glass fibre laminate, EPS, OSB and timber projectile are given in section 5.3.1.

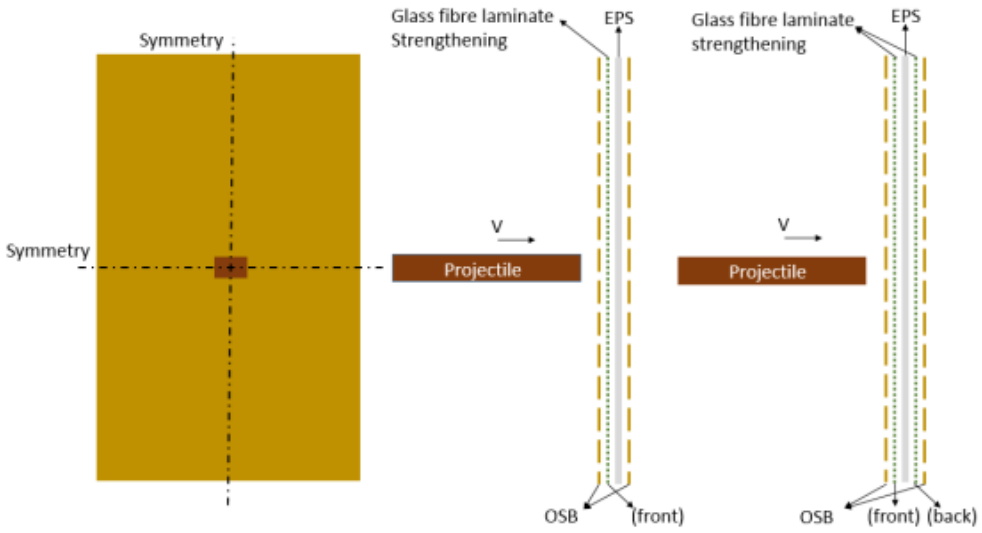


(a)


(b)

*Figure 5.2 (a) Schematic diagram of Glass fibre laminate strengthening position (L) Plan view (M) Interlayer strengthening (Panel B/C/D/G); (R) Double interlayer strengthening (Panel E/F); (b) Manufacture of the Glass fibre laminate strengthened OSB skin SIP*

### 5.2.2 Experimental setup

The available impact test techniques and facilities have been briefly reviewed by Lu and Yu (163). The pneumatic cannon testing system used in this system includes a pneumatic cannon, a L section steel support frame, four light sources, and two high speed cameras (i.e., FASTCAM_SA-Z and FASTCAM_Mini_UX100) linked to the data acquisition system. The laboratory apparatus is shown in Figure 5.3. G-clamps were used around the specimen and fastened on the steel frame for easy installation. The 1500w Halogen lights were used to provide intensive light. The centre area of the specimen was targeted with the timber projectile, the velocity of which was adjusted by changing air pressure in the pressure vessel. The data of the panel response and the residual velocity of the projectile were extracted and analysed from the clips recorded by the two high speed cameras. The images were captured at

2000 frames per second at full resolution of 1024*1024 pixels by high speed cameras.

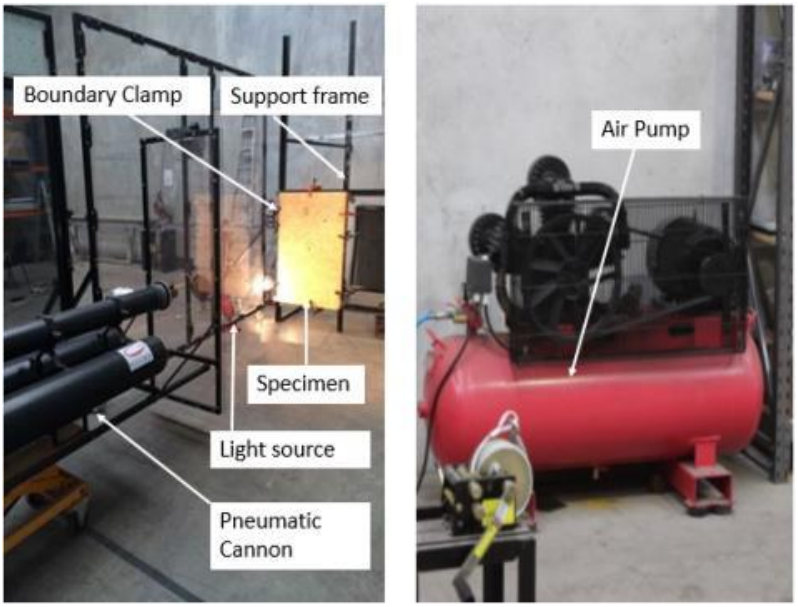


*Figure 5.3 Testing apparatus*

### 5.2.3 Experimental results

AS/NZS1170.2 does not specify a Pass/Fail criteria for a building envelop that is subjected to windborne debris impact. It only specifies that the debris loading shall be equivalent to 4 kg timber member with a 100mm*50mm cross section travelling at 0.4V. However, the standards such as SBC (US Standard Building Code) and FBC (Florida Building code) specify that the system is acceptable if specimens reject the debris impacts without penetration. Therefore, to examine the performance of the panels against windborne debris impact, the pass/fail criteria is used to quantify the performance in this study. The “pass” indicates there is no opening created on the panel, while the tested specimen is considered as “fail” when projectile impact caused an opening in the panel that would allow wind to blow through. In this study, it was observed that in some cases although the projectile did not create an opening in the panel, large impact force caused spalling damage to the back OSB layer, generating secondary OSB debris flying at a relatively high speed. Since this secondary debris could threat people behind the structural panel, the tested panel with spall damage to the back OSB layer is also considered as failed although no opening was created. Besides, the evaluation of “pass” or “fail” of each tested specimen, in this study, the residual velocity tracked from high speed cameras is also analysed to quantitatively evaluate the structural performance and penetration resistance capacity of the SIPs. The testing results are summarized in Table 5.1.

*Table 5.1 Testing scheme and results*

| Specimen | 1st Strengthening interlayer (front) | 2nd Strengthening interlayer (back) | Testing result | Impact velocity (m/s) | Residual velocity (m/s) |
|---|---|---|---|---|---|
| A (Reference panel) | - | - | Fail(Stay) | 18.0 | 0 |
| B-1st hit | 1mm | - | Fail(Stay) | 22.4 | 0 |
| C-1st hit | 1.5mm | - | Pass | 20.2 | -3.3 |
| C-2nd hit | 1.5mm | - | Pass | 22.5 | -4.3 |
| D-1st hit | 3mm | - | Pass | 26.1 | -4.0 |
| D-2nd hit | 3mm | - | Pass | 32.0 | -1.7 |
| E-1st hit | 1.5mm | 1mm | Fail(Stay) | 32.2 | 0 |
| E-2nd hit | 1.5mm | 1mm | Pass | 26.8 | -2.4 |
| F-1st hit | 3mm | 1.5mm | Pass | 33.8 | -4.7 |
| F-2nd hit | 3mm | 1.5mm | Fail | 40.7 | -2.1 |
| G-1st hit | 5mm | - | Fail | 40.4 | -3.0 |

N.B “-” means rebound velocity

### 5.2.3.1 Damage patterns

The specimen A was tested and used as a reference panel to identify the penetration resistance capacity of the commercial SIP with OSB skins, and to demonstrate the effectiveness of the glass fibre laminate strengthening measures proposed in this study. Four projectile impacts with the velocities of 15, 21.2, 18, and 20 m/s were applied on the panel, respectively. The test results for each impact were “pass”, “fail”, “fail” and “fail”, respectively. The failure mode was typical punching shear failure. The projectile impact at the velocity of 18m/s caused an opening with the projectile staying on the panel. The velocity of 18m/s was therefore deemed as the critical velocity to penetrate the reference panel. As shown in Figure 5.4, the damage was limit to a localised area as the typical punching shear failure. No obvious bending or shear failure response was observed on the panel. Therefore, each impact could be assumed as an independent strike and the existing localized failure has limited influence on the subsequent impact at other impact locations.

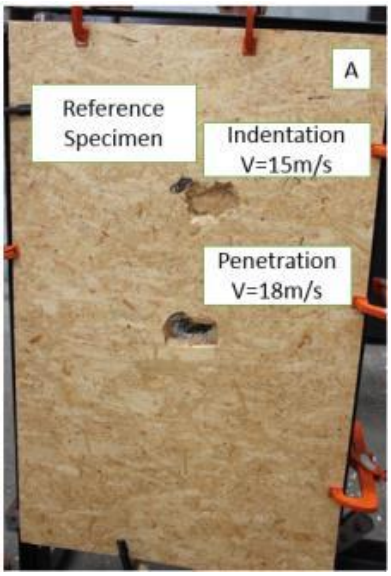


*Figure 5.4 Photograph of specimen A*

The specimen B was strengthened with one 1mm-thick glass fibre laminate sheet at position (a), as shown in Figure 5.5. The panel was subjected to the 4 kg timber projectile impact at velocity of 22.4 m/s. The test result was “fail” with the projectile penetrated but stayed in the panel as shown in Figure 5.5. The failure mode was typical shear punch failure. No crack or global structural response was observed on the panel. As the projectile stayed in the panel, 22.4 m/s was deemed the critical impact velocity to penetrate the specimen B. The testing results indicate that strengthening the commercial SIP with one 1 mm glass fibre laminate increased the critical impact velocity from 18 mm/s to 22.4 mm/s.

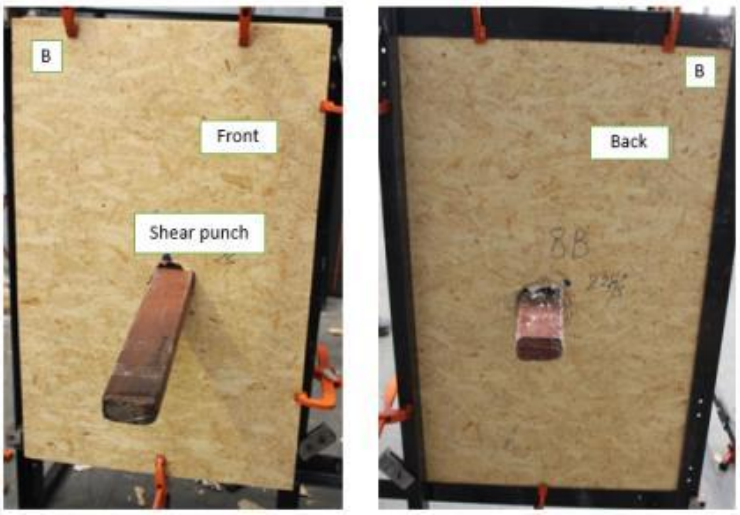


*Figure 5.5 Photograph of specimen B (L) Front view; (R) Back view*

The specimen C was similarly strengthened as specimen B, except the thickness of the glass fibre laminate sheet is increased to 1.5 mm. The specimen was first impacted by the projectile at velocity of 20.2 m/s. The first

impact caused a small dent on the front OSB skin of the specimen, but the specimen was not penetrated as shown in Figure 5.6. The specimen was then subjected to a second impact at velocity of 22.5 m/s. As shown in Figure 5.6, the second impact caused a larger dent on the front OSB skin and part of the EPS core of the specimen as compared to that generated by the first impact, but the specimen again was not penetrated although the glass fibre laminate sheet was also damaged. The panel rejected the timber debris in the two impacts with the rebound velocity of 3.3 m/s and 4.3 m/s, respectively. The second strike left a deeper indentation than the first strike. Slight crack on the back OSB skin was observed after the second strike but no OSB skin spalling damage was observed. Although some cracks on back OSB skin were observed after the second projectile impact, the slight crack on the OSB skin would not affect the function of panel to prevent the wind blowing into the house as the EPS core remained intact.

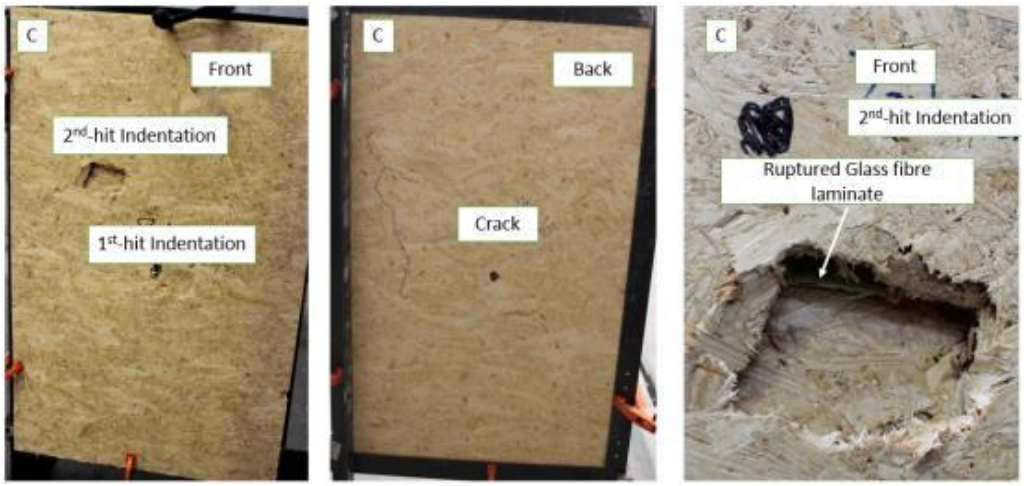


*Figure 5.6 Photograph of specimen C (L) Front view; (M) Back view; (R) 2nd-hit Indentation point*

The specimen D was similarly strengthened as specimen B and C, but the thickness of glass fibre laminate layer is 3mm. The specimen was impacted twice at different locations with the impact velocity of 26.1 m/s and 32 m/s, respectively. As shown in Figure 5.7, both impacts caused indentations on the front OSB skin. The strengthened panel rejected both strikes with the projectile rebound velocity of 4.0 m/s and 1.7 m/s, respectively. Neither impact penetrated the panel. As expected the second projectile impact caused a more severe damage on the back OSB skin, where large cracks developed from the centre area to the top boundary. However, the specimen passed both impacts as no opening was created that would allow wind blow through. As shown in Figure 5.8 although the second projectile impact caused severe crack on the back OSB skin and debonding of the glass fibre laminate sheet from the front OSB skin, the EPS core remained basically intact which would prevent wind flowing through the panel. It should be noted that the rebound velocity of the

second strike is less than the first one due to the energy dissipated by the fracture of the back OSB skin and relatively deeper indent on the front OSB skin. The specimen D was considered able to resist the debris impact at the velocity of 32 m/s.

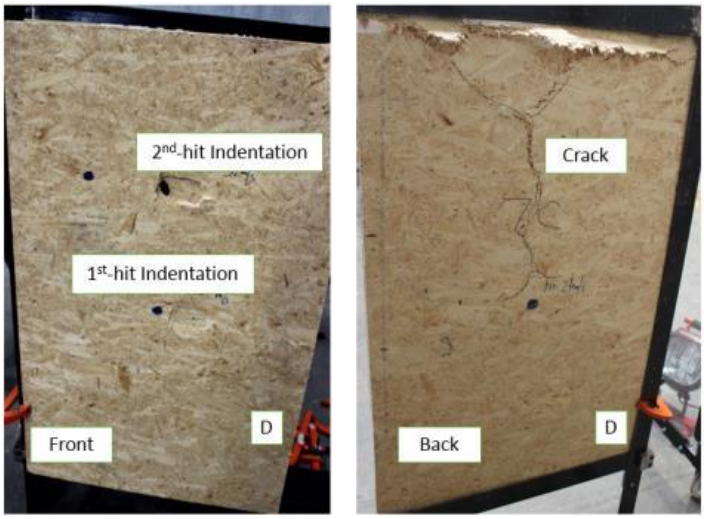


*Figure 5.7 Photograph of specimen D (L) Front view; (R) Back view*

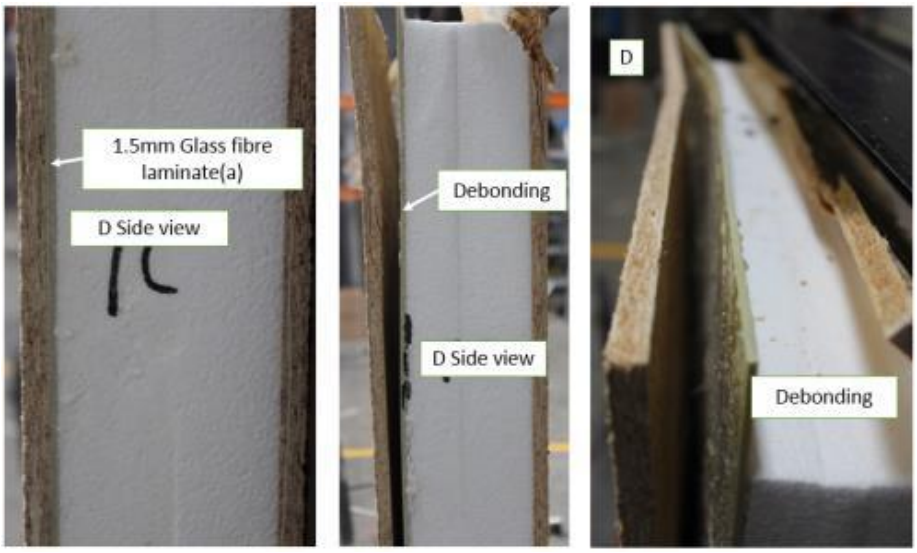


*Figure 5.8 Photograph of specimen D (L) Side view (before test); (M) Side view (after test); (R) Top side view (after test)*

Specimen E was strengthened with two glass fibre laminate layers as shown in Figure 5.9. The thickness of the front strengthening layer is 1.5 mm and that of the back layer is 1mm. It was tested with two impacts with velocity of 32.2 m/s and 26.8 m/s, respectively. As shown in Figure 5.9, both impacts caused penetrations on the front OSB skin. The first impact also damaged the front glass fibre laminate layer and EPS core. Although the projectile was stopped by the back glass fibre laminate layer and stayed in the panel, the first impact also caused severe damage to the back OSB skin and the EPS core. The back glass fibre laminate sheet at position (b) was ruptured and displaced with EPS

core. The panel was identified as “fail” after the first impact owing to its spalling damage of the back OSB skin, but passed the second projectile impact. The panel rejected the projectile in the second impact with a rebound velocity of 2.4 m/s. By comparing the performance of specimens D and E, it is obvious that using a thicker glass fibre sheet is more effective than using two thin glass fibre sheets in strengthening the panel.

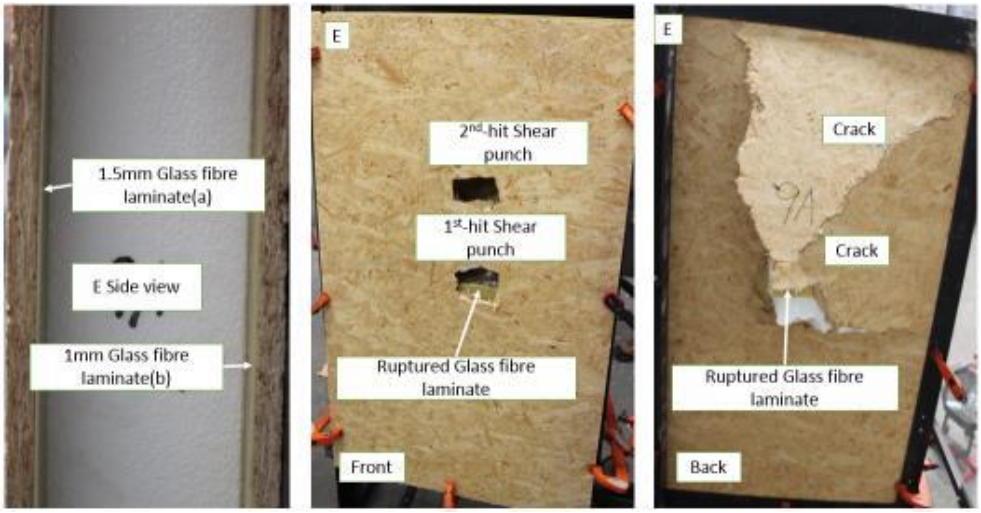


*Figure 5.9 Photograph of specimen E (L) Side view; (M) Front view; (R) Back view*

The specimen F was also strengthened with two glass fibre laminate interlayers as shown in Figure 5.10. The thickness of the front layer is 3mm and that of the back layer is 1.5 mm. The panel was also impacted twice with the first impact velocity 33.8 m/s and the second impact velocity 40.7 m/s. As shown in Figure 5.10 , the first projectile impact caused an indentation on the front OSB skin, and was rejected by the panel with a rebound velocity of 4.7m/s. The panel survived this impact and the test result was “pass”. The second strike at the velocity of 40.7 m/s caused a deeper indentation on the front OSB skin, and severe cracks extending from the centre to the top and the right side of the front OSB skin. Severe damage was also observed at the back OSB skin, with the top portion of OSB skin debonded and fell off the panel along the crack. As observed from the side view of the specimen, debonding occurred at all the interfaces between OSB skin, glass fibre laminate sheet and the EPS core. Although the panel rejected the projectile in the second impact with the rebound velocity of 2.1 m/s, the test result was classified as “fail” owing to the creation of secondary debris from the damaged back OSB skin. Therefore, the specimen F was identified as failed when subjected to the impact at 40.7m/s.


*Figure 5.10 Photograph of specimen F (L) Front view; (M) Back view; (R) Side view*

Figure 5.11 shows the damaged specimen G strengthened with a 5mm thick glass fibre laminate as an interlayer between the front OSB skin and EPS core. As shown, the projectile impact at the velocity of 40.4 m/s left an indentation and a large crack from the centre to the left side on the front OSB skin. The back OSB skin also suffered severe damage and debonding between the glass fibre laminate and the EPS foam. The panel rejected the projectile with a rebound velocity of 3 m/s. However, the panel was classified as “fail” since secondary debris from the back OSB skin was observed during the impact, although the impact did not create opening on the panel that would allow wind blow through.

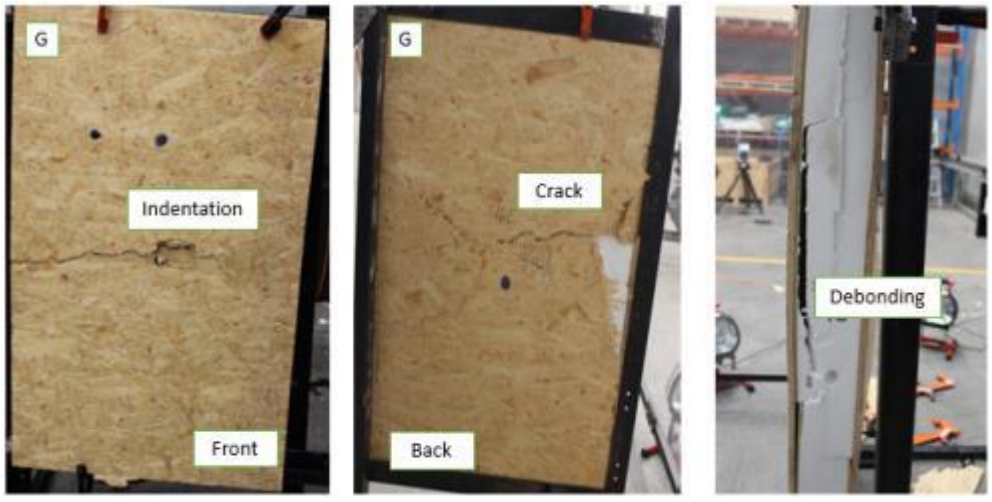


*Figure 5.11 Photograph of specimen G (L) Front view; (M) Back view; (R) Side view*

### 5.2.3.2 Comparisons and discussions

Based on the observations from the testing results, the reference panel A without glass fiber laminate strengthening failed at impact velocity 18 m/s. The projectile penetrated the panel and caused punching shear failure. Since both the OSB and EPS foam were brittle with relatively low strength, projectile

impacts caused only very localized damage. Other specimens B/C/D/E/F/G strengthened with glass fibre laminate as interlayer all demonstrated better impact-resistant performance than the reference panel. Because of the relatively high strength of glass fibre, projectile was in general stopped by the glass fibre laminate layer. However, this resulted in the impact energy being transferred to the entire panel. The damage mode of the panel was usually indentation in the front OSB skin associated to local punching shear damage, and large back OSB skin damage associated to global flexural response of the panel.

The specimen B, C, D and G strengthened with a single glass fibre laminate sheet in between the front OSB skin and EPS core showed capacity to resist projectile impact at higher velocity than the reference panel. Testing on the specimen C proved the critical impact velocity of the panel strengthened with a 1.5 mm-thick glass fibre laminate layer increased to 22.5 m/s. The specimen D strengthened with a 3 mm-thick glass fibre laminate interlayer survived the impact at 32 m/s, which indicated the resistance capacity of the specimen D was significantly improved as compared to the reference panel. The specimen G strengthened with a 5 mm glass fibre laminate interlayer did not pass the test at the impact velocity of 40.4 m/s owing to the secondary debris created from the severely damaged back OSB skin. As one of the two specimens strengthened with two glass fibre laminate sheets, the specimen E survived the projectile impact at velocity 26.8 m/s but failed at 32.2 m/s with the projectile penetrating and staying in the panel. The result indicated the critical impact velocity was more than 26.8 m/s for the 1.5mm-thick and 1mm-thick glass fibre laminates strengthened panel. The specimen F strengthened with a 3 mm and a 1.5 mm thick glass fibre laminates passed the test with the impact velocity of 33.8 m/s but failed when the impact velocity was 40.7 m/s owing to again the secondary debris generated from the back OSB skin. It can be concluded from the testing results that adding one or two glass fibre laminate sheets as interlayers effectively increases the projectile impact resistance capacity of the panel. The thicker is the glass fibre laminate, the higher is the penetration resistant capacity of the strengthened panel. However, the strengthening effectiveness cannot keep improving by increasing the thickness of glass fibre laminate. This is because the brittle OSB skin and EPS core cannot experience large deformation. When the glass fibre laminate sheet is thick and stops the projectile penetration, it transfers the impact energy to global panel response. Large flexural response of the panel damages the back OSB skin which leads to the failure of the panel. For example, the specimens F/G were not failed by direct penetration but the secondary debris owing to the failure of the back OSB skin.

## 5.3. Numerical simulation

### 5.3.1 Finite element model

The numerical model is developed in ANSYS and pre-processed in LS-PREPOST, which is shown in Figure 5.12. The accuracy of the model is verified by the testing results. The failure mode and the residual velocity of the projectile are compared and analysed. In this study, two specimens i.e. B/C strengthened with 1mm and 1.5mm thick fibre glass laminate are selected to calibrate the numerical model. The glass fibre laminate sheet is modelled with Belytschko-Tsay shell element, which has two integration points to model the biaxial behaviour. Timber projectile is modelled with eight-node solid elements. OSB skins and EPS core are modelled by using constant stress solid element with single integration node, which can help to avoid the negative volume during the calculation. As suggested by the convergence test result of a previous study (16) the whole panel is divided into dense and non-dense areas. As shown in Figure 5.12, impacted area is modelled with dense meshes of size 5*5 mm and 5*5*5 mm for shell element and solid element, respectively. The areas away from the impacted location are modelled with relatively coarse meshes with the mesh sizes of 25*25 mm and 25*25*25 mm for shell and solid elements, whereas the mesh size of the connecting areas are 25*5mm for shell elements and 25*5*5mm for solid elements. Due to symmetry, only a quarter of the full panel is modelled for computational efficiency.

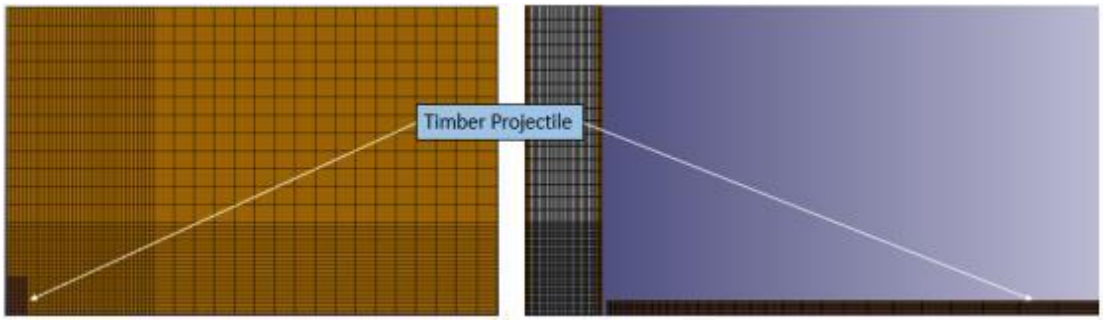


*Figure 5.12 Numerical model of a quarter panel (L) Plan view; (R) Side view*

### 5.3.1.1 Material models

The material models *MAT 3, *MAT 163, *MAT 143 and *MAT 20, are used to simulate glass fibre laminate interlayer, EPS foam core, OSB skin, and the timber projectile, respectively.

Herranen (135) reported the glass fibre laminate was an isotropic and linear material. The material model *MAT 3 PLASTIC KINEMATIC was used to model the glass fibre laminate interlayer. The detailed parameters of glass fibre laminate are given in Table 5.2.

*Table 5.2 Material parameters of Glass fibre laminate and EPS foam*

| *Glass fibre laminate (*MAT 3 PLASTIC KINEMATIC)* | | *EPS foam (*MAT 163 MODIFIED CRUSHABLE FOAM)* | |
|---|---|---|---|
| Mass density (kg/m$^3$) | 1900 | Mass density (kg/m$^3$) | 13.5 |
| Young's modulus (Pa) | 2.10E+10 | Young's modulus (Pa) | 2.10E+06 |

| | | | |
|---|---|---|---|
| Poisson's ratio | 0.118 | Poisson's ratio | 1.00E-04 |
| Tensile strength (Pa) | 2.00E+08 | Tensile stress cut off (Pa) | 3.30E+05 |
| Failure stain | 0.01 | Rate sensitivity via damping coefficient | 4.00E-01 |

As reported by Croop et al(164), material models like *MAT 57 LOW DENSITY FOAM, *MAT 63 CRUSHABLE FOAM, and *MAT 83 FU CHANG can simulate the properties of Polymeric foam. However, it was found that the material model *MAT 163 can define the strain rate effect for better simulation of the response of EPS foam core (16). In this study, the *MAT 163 CRUSHABLE FOAM is used in the finite element model to simulate the EPS core with the defined yield stress versus volumetric strain curve. The basic material properties of EPS are provided in Table 5.2. The stress- strain curves obtained from laboratory tests (165) are shown in Figure 5.13. *MAT ADD EROSION is applied to the EPS foam to better define the elimination of the failed elements to overcome the computational overflow. Moreover, hourglass control is applied on shell and solid elements (IHQ=2, 3) to avoid computational overflow.

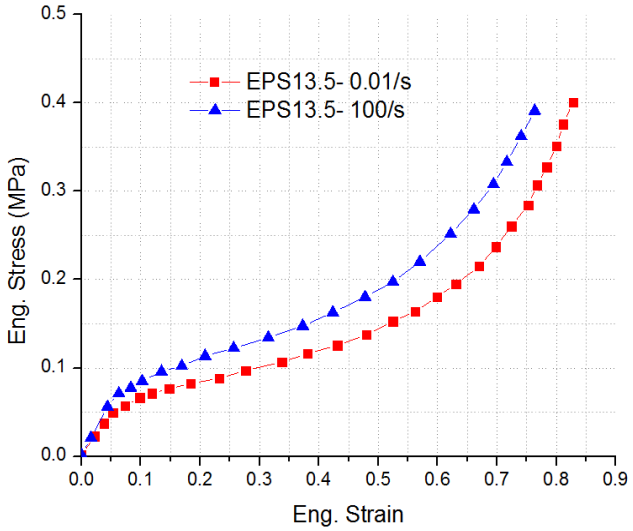


*Figure 5.13 Stress–strain curves of EPS foam (density 13.5 kg/m3)(165)*

The material model *MAT 143 WOOD is used for modelling the OSB skin. The OSB material parameters have been calibrated in a previous study (166). The detailed parameters are given in Table 5.3 based on the manufacturer's data sheet and material tests. The failure criteria of *MAT 143 WOOD in parallel mode and perpendicular mode are described as follows (167).

The failure in parallel mode occurs when

$$f_{\parallel} = \frac{\sigma_{11}^2}{X^2} + \frac{\left(\sigma_{12}^2 + \sigma_{13}^2\right)}{S_{\parallel}^2} - 1 \geq 0, \tag{5.1}$$

where X equals to $X_t$ (when $\sigma_{11} \geq 0$) and $X_C$ (when $\sigma_{11} < 0$).

The perpendicular mode failure occurs when

$$f_{\perp} = \frac{\left(\sigma_{22} + \sigma_{33}\right)^2}{Y^2} + \frac{\left(\sigma_{23}^2 + \sigma_{22}\sigma_{33}\right)}{S_{\perp}^2} - 1 \geq 0, \tag{5.2}$$

where Y equals to $Y_t$ (when $\sigma_{22+}\sigma_{33} \geq 0$) and $Y_C$ (when $\sigma_{22+}\sigma_{33} < 0$).

$X_t$ and $X_c$ stand for tensile and compressive strength parallel to the grain; $Y_t$ and $Y_c$ stand for tensile and compressive strength perpendicular to the grain; S stands for shear strength in the direction of the grain.

*Table 5.3 Material parameters of *MAT 143 WOOD*

| *OSB (*MAT 143 WOOD)* | | | |
|---|---|---|---|
| Mass density (kg/m$^3$) | 638 | Parallel fracture energy in tension (J) | 1.80E+04 |
| Parallel normal modulus (Pa) | 4.50E+09 | Parallel fracture energy in shear (J) | 1.80E+04 |
| Perpendicular normal modulus (Pa) | 4.50E+09 | Parallel softening parameter | 30 |
| Parallel shear modulus (Pa) | 1.50E+09 | Parallel maximum damage | 0.99 |
| Perpendicular shear modulus (Pa) | 1.50E+09 | Perpendicular fracture energy in tension (J) | 1.80E+04 |
| Parallel major Poisson's ratio | 0.23 | Perpendicular fracture energy in shear (J) | 1.80E+04 |
| Parallel compressive strength (Pa) | 1.59E+07 | Perpendicular softening parameter | 30 |
| Parallel tensile strength (Pa) | 9.90E+06 | Perpendicular maximum damage | 0.99 |
| Perpendicular compressive strength (Pa) | 1.59E+07 | Parallel shear strength (Pa) | 6.80E+06 |
| Perpendicular tensile strength (Pa) | 9.90E+06 | Perpendicular shear strength (Pa) | 6.80E+06 |

It was observed that the timber projectile did not experience obvious damage or deformation after each impact test. Therefore, rigid material *MAT 20 is used to model timber debris with the parameters of 888kg/m$^3$, 220GPa, and 0.1 for the density, Young's modulus and Poisson's ratio respectively.

#### 5.3.1.2 Boundary conditions

In the tests, G-clamps were applied along four sides of each panel. In the finite element model, pinned boundary condition with keyword *BOUNDARY SPC SET is used at the clamped locations of the panel to better model the testing conditions.

#### 5.3.1.3 Contact keywords

In the finite element model, *CONTACT ERODING SINGLE SURFACE was used to define the contact between the projectile and the specimen.

*CONTACT ERODING SURFACE TO SURFACE was applied between each contact surfaces, i.e., between the EPS and glass fibre laminate, and between the glass fibre laminate and OSB skins.

Mutalib (77) reported the FRP debonding could significantly influence the numerical simulation results. As observed from the impact video captured by high speed cameras, debonding between glass fibre laminate, EPS foam and OSB skin was found in some tested specimens as reported above. *CONTACT TIEBREAK SURFACE TO SURFACE ONLY was used to model the bonding conditions between glass fibre laminate interlayer and OSB/EPS. The adhesive strength was defined by two parameters, NFLS (tensile failure stress) and SFLS (shear failure stress) to model the adhesive strength in the panel. As defined in the manual of LS-DYNA (168), bonding between basalt fibre and OSB/EPS would only survive if

$$\left(\frac{|\sigma_n|}{NFLS}\right)^2 + \left(\frac{|\sigma_s|}{SFLS}\right)^2 \leq 1 \tag{5.3}$$

where $\sigma_n$ and $\sigma_s$ represent the tensile stress and shear stress, respectively. The normal strength of adhesive provided by the manufacturer is around 6 MPa to 7 MPa (16). The actual adhesive strength depends on the quality of the adhesive application between each surfaces and curing conditions. In this model, a lower limit of adhesive strength was used, which was about 4.5 MPa. This strength was determined as a result of a series of trial-and-error simulations and it leads to good and comparable match of the numerical simulation results to the laboratory test results. It should be noted that it is not uncommon that the actual bond strength is smaller than the epoxy strength. The bond strength depends not only on epoxy strength, but also on workmanship of applying it and on curing conditions, etc. Cases of actual bond strength substantially smaller than the epoxy strength have been reported in practice.

### 5.3.2 Comparisons between experimental and numerical simulation results

Two tested panels were selected to verify the accuracy of the finite element model. They are specimen B with 1 mm-thick glass fibre laminate interlayer placed between the front OSB skin and EPS core of the panel, and specimen C with 1.5 mm-thick glass fibre laminate interlayer also placed between the front OSB skin and EPS core. The numerically simulated damage modes and time histories of debris velocity were compared with the testing results. The comparisons of residual velocity are given in Table 5.4.

*Table 5.4 Data comparisons between laboratory test and numerical simulation (A)*

| Specimen | Impact velocity (VI) | | Residual velocity (VR) | | Error |
|---|---|---|---|---|---|
| | Test | Numerical | Test | Numerical | |
| B | 22.4m/s | 22.4m/s | 0m/s | 0m/s | 0% |
| C-1st hit | 20.2m/s | 20.2m/s | -3.3m/s | -3.4m/s | 3% |
| C-2nd hit | 22.5m/s | 22.5m/s | -4.3m/s | -4.7m/s | 9.3% |

N.B "-" means rebound velocity

### 5.3.2.1 Specimen B

The specimen B was subjected to a projectile impact at the velocity of 22.4 m/s. As shown in Figure 5.14(L), the projectile penetrated into and stayed in the panel. Numerical simulation closely reproduced the experimental test. The projectile penetrated through the specimen and generated some secondary debris from the damaged OSB skin and EPS. The failure mode was typical punching shear failure. Figure 5.15 compares the time histories of projectile velocity recorded in the test and from numerical simulation. As shown in the figure, numerical result agrees well with the test results, indicating the accuracy of the numerical simulations.

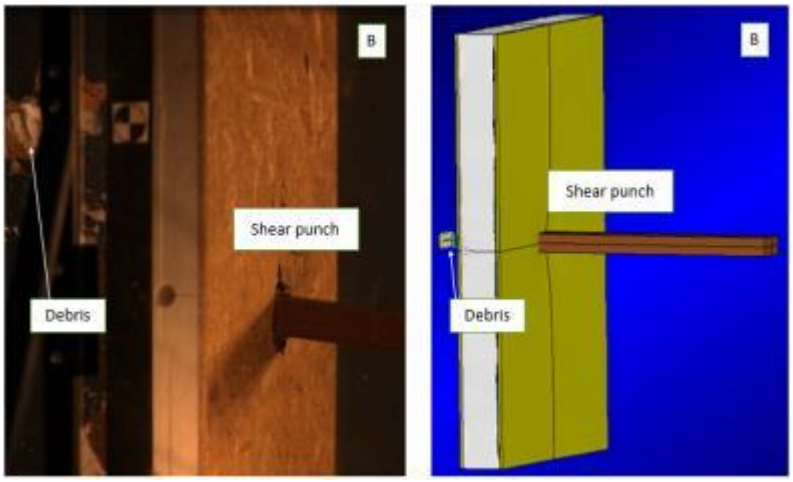


*Figure 5.14 Comparisons of damage mode of specimen B (L) Test; (R) Numerical*

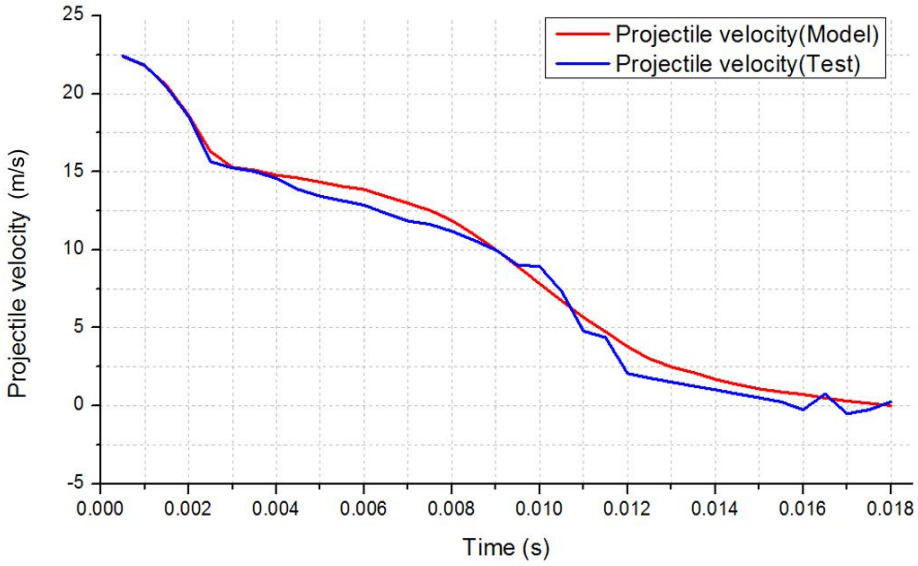


*Figure 5.15 Comparisons of projectile velocity obtained from laboratory test and numerical simulation during the 1st-hit on specimen B*

### 5.3.2.2 Specimen C

Figure 5.16 and Figure 5.17 compares the damage modes of specimen C subjected to two impacts at the velocity 20.2 m/s and 22.5m/s, respectively. As shown both strikes caused indentation on the front OSB skin and debonding between the front OSB skin and glass fibre laminate. The numerical simulation closely reproduced the test result. Figure 5.18 compares the projectile velocity time histories corresponding to the first impact recorded in the test and obtained from numerical simulation. As shown numerical simulation result agrees well with the test data. The panel rejected the projectile with a rebound velocity of 3.3 m/s in the laboratory test and 3.4 m/s in the numerical simulation. The difference between the numerical simulation and test result in rebound velocity is 3%.

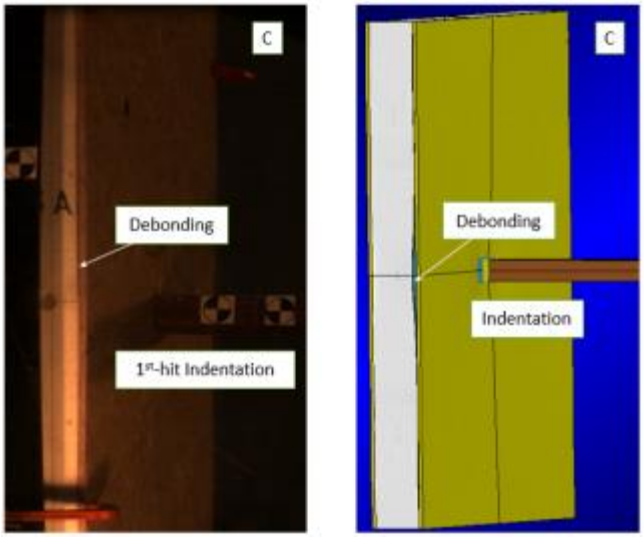


*Figure 5.16 Comparison of damage mode of 1st-hit on specimen C (L) Test; (R) Numerical*

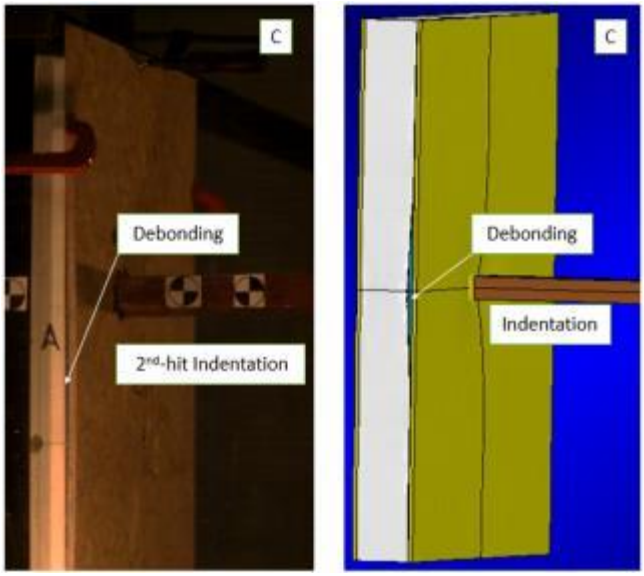


*Figure 5.17 Comparison of damage mode of 2nd-hit on specimen C (L) Test; (R) Numerical*

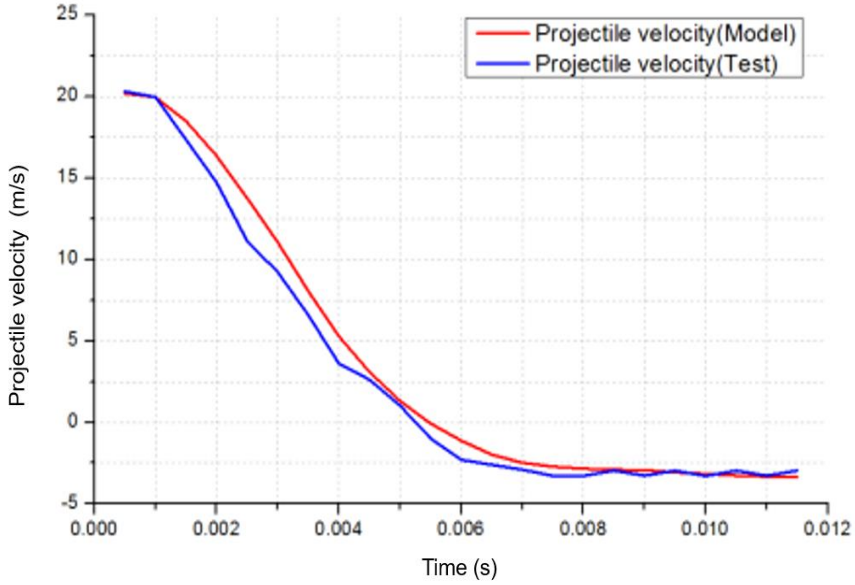


*Figure 5.18 Comparisons of projectile velocity obtained from laboratory test and numerical simulation during the 1st-hit on specimen C*

### 5.3.3 Vulnerability curve

The above verified numerical model can be used to simulate responses of OSB skin SIP panels subjected to windborne debris impact. As an example, in this study, the performance of OSB skin SIPs strengthened with a 1mm-thick glass fibre laminate interlayer between the front OSB skin and EPS core is analysed. Intensive numerical simulations are carried out to derive the vulnerability curve of the panel subjected to windborne debris impact. The thickness of EPS foam, OSB skin and glass fibre laminate of the example panel considered in the study are 100mm, 10mm and 1mm, respectively. The timber projectile with eight weights (i.e. 1kg, 2kg, 3kg, 4kg, 5kg, 6kg, 7kg, and 8kg), and the impact velocity ranging from 14m/s to 40m/s, covering the damaging and the extreme

credible impact velocity in the cyclone area (22) are considered in the simulations.

Table 5.5 and Table 5.6 summarize numerical results of the 1mm glass fibre laminate and 1.5mm glass fibre laminate strengthened SIP panels under different impact scenarios, where “P” and “N” indicate the perforation and non-perforation of the test, i.e., fail and pass of the panel. Table 5.7 and Table 5.8 give the threshold kinetic energy of the projectile corresponding to the different impact conditions. Both curves indicate that the performance of the panel in resisting the projectile impact cannot be reliably correlated with the impact kinetic energy. As indicated in Table 5.7, the panel rejected 5 kg projectile at the impact velocity of 18 m/s with kinetic energy 810J. However, the panel failed when it is subjected to an impact of a 3kg projectile at a velocity of 23 m/s with the kinetic energy of 793J. Similarly, as given in Table 5.8, the panel rejected the 5 kg projectile at velocity of 26 m/s with the kinetic energy of 1690J, but failed when it is subjected to a 3 kg projectile impact at a velocity of 33 m/s with the kinetic energy of 1633J. The results indicate that the panel is more vulnerable to be penetrated by the projectile with a smaller weight but a higher impact velocity at the same kinetic energy. This observation is similar to the results obtained by Zhang and Hao on project impact on laminated glass windows (45). Figure 5.19 shows the vulnerability curves corresponding to the projectile mass and impact velocity as given in Table 5.5 and Table 5.6. As shown in Figure 5.19, consistent results on the panel vulnerability can be derived by considering both the projectile mass and impact velocity.

*Table 5.5 Impact penetration results with respect to the projectile mass and velocity (Specimen B)*

| | Velocity(m/s) | | | | | | | | | | |
|---|---|---|---|---|---|---|---|---|---|---|---|
| Mass | 14 | 16 | 18 | 20 | 22 | 24 | 26 | 28 | 30 | 37 | 40 |
| 1kg | N | N | N | N | N | N | N | N | N | N | P |
| 2kg | N | N | N | N | N | N | N | N | P | P | P |
| 3kg | N | N | N | N | N | P | P | P | P | P | P |
| 4kg | N | N | N | N | P | P | P | P | P | P | P |
| 5kg | N | N | N | P | P | P | P | P | P | P | P |
| 6kg | N | N | P | P | P | P | P | P | P | P | P |
| 8kg | N | P | P | P | P | P | P | P | P | P | P |

*Table 5.6 Impact penetration results with respect to the projectile mass and velocity (Specimen C)*

| | Velocity(m/s) | | | | | | | | | | |
|---|---|---|---|---|---|---|---|---|---|---|---|
| Mass | 20 | 22 | 26 | 28 | 32 | 35 | 37 | 40 | 43 | 47 | 50 |
| 1kg | N | N | N | N | N | N | N | N | N | N | P |
| 2kg | N | N | N | N | N | N | N | N | P | P | P |
| 3kg | N | N | N | N | N | P | P | P | P | P | P |
| 4kg | N | N | N | N | P | P | P | P | P | P | P |
| 5kg | N | N | N | P | P | P | P | P | P | P | P |
| 6kg | N | N | P | P | P | P | P | P | P | P | P |
| 8kg | N | P | P | P | P | P | P | P | P | P | P |

*Table 5.7 Threshold kinetic energy of projectile to penetrate the strengthened panel (Specimen B)*

| | Velocity(m/s) | | | | | | |
|---|---|---|---|---|---|---|---|
| Mass | 14 | 16 | 18 | 20 | 22 | 28 | 37 |
| 1kg | | | | | | | 685J |
| 2kg | | | | | | 784J | |
| 3kg | | | | | 726J | | |
| 4kg | | | | 800J | | | |
| 5kg | | | 810J | | | | |
| 6kg | | 768J | | | | | |
| 8kg | 784J | | | | | | |

*Table 5.8 Threshold kinetic energy of projectile to penetrate the strengthened panel (Specimen C)*

| | Velocity(m/s) | | | | | | |
|---|---|---|---|---|---|---|---|
| Mass | 20 | 22 | 26 | 28 | 32 | 40 | 47 |
| 1kg | | | | | | | 1104J |
| 2kg | | | | | | 1600J | |
| 3kg | | | | | 1536J | | |
| 4kg | | | | 1568J | | | |
| 5kg | | | 1690J | | | | |
| 6kg | | 1452J | | | | | |
| 8kg | 1600J | | | | | | |

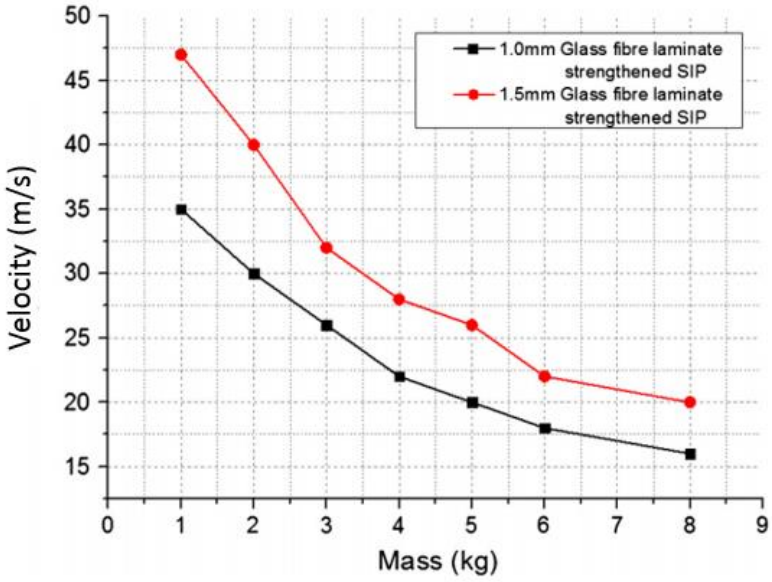


*Figure 5.19 Vulnerability curves of OSB skin SIP panel strengthened with 1 mm (Specimen B) and 1.5 mm (Specimen C) glass fibre laminate subjected to windborne debris impact*

## 5.4 Summary

In this chapter, laboratory tests on one non-strengthened OSB skin structural insulated panel and six glass fibre laminate strengthened panels subjected to windborne debris impact were carried out by using a pneumatic cannon testing system. The test results indicate two types of failure modes, i.e. punching shear failure and flexural failure of the back OSB skin with possible secondary debris from the broken OSB skin. The residual velocity of the projectile was recorded and measured by using high speed camera. It was found that the unstrengthened SIP panel can withstand the projectile impact at 18 m/s, and strengthening the panel with a 3 mm-thick glass fibre laminate sheet can increase the projectile impact resistance capacity to 32 m/s. However, further increasing the glass fibre laminate thickness is not effective because the damage mode changed from punching shear to flexural damage of the back OSB skin with possible secondary debris. A numerical model was also developed to simulate the panel responses subjected to debris impact. The numerical model was calibrated and verified against the testing data. With the calibrated numerical model, vulnerability curves of the panel were generated with respect to debris mass and velocity. It is found that the penetration resistant capacity of the panel is not determined by the kinetic energy of the projectile alone. Both the projectile mass and velocity would affect the penetration resistant capacity.

# Chapter 6 Experimental and numerical study on steel wire mesh and basalt fibre mesh strengthened structural insulated panel (SIP) against windborne debris impact

## 6.1 Introduction

In this chapter, the performances of OSB skin SIPs strengthened by steel wire mesh (Ø0.64mm, 6.5×6.5 mm spacing) and three types of basalt fibre mesh (Ø1mm, 10×10 mm spacing adhesive coated, 10×10 mm spacing uncoated and 5×5 mm spacing adhesive coated) under windborne debris impact are experimentally investigated by using air cannon impact testing system. The strengthening layer of steel wire mesh and basalt fibre mesh is shown in Figure 6.1 and Figure 6.2, respectively. The material properties of the strengthening mesh layers are given in Table 6.1. Numerical models are also developed to simulate the responses of OSB skin SIPs strengthened by steel wire and basalt fibre mesh. The accuracy of the models is verified by the experimental results.

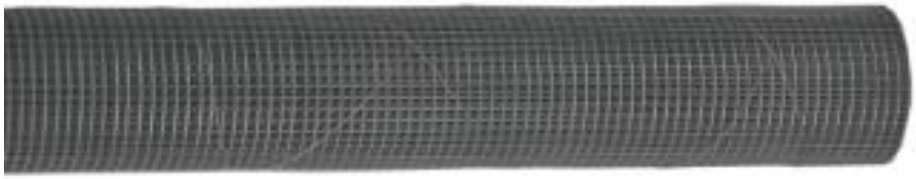

*Figure 6.1 Photograph of steel wire mesh roll*

*Figure 6.2 Photograph of basalt fibre mesh*

*Table 6.1 Material properties of steel wire mesh, basalt fibre mesh, OSB and EPS*

| *Steel wire mesh* | | *Basalt fibre mesh* | |
|---|---|---|---|
| Mass density (kg/m$^3$) | 7800 | Mass density (kg/m$^3$) | 2750 |
| Young's modulus (Pa) | 2.10E+11 | Young's modulus (Pa) | 2.00E+10 |
| Poisson's ratio | 0.3 | Poisson's ratio | 0.26 |
| Yield strength (Pa) | 3.00E+08 | Tensile strength (Pa) | 4.80E+09 |
| Oriented Strand board (OSB) | | EPS foam | |
| Mass density (kg/m$^3$) | 638 | Mass density (kg/m$^3$) | 13.5 |
| Normal modulus (Pa) | 4.50E+09 | Young's modulus (Pa) | 2.10E+06 |
| Tensile strength (Pa) | 9.90E+06 | Tensile stress cut off (Pa) | 3.30E+05 |

## 6.2 Experimental investigation

A total of seven specimens were manufactured and tested by using an air cannon impact system with a wood projectile specified in the Australian code (19). The damage modes were observed and the measurements including the projectile impacting velocity and the residual velocity were recorded through two high speed cameras. The specimens and the schematic diagram of experimental setup are detailed below.

### 6.2.1 Description of specimens

The specimens of unstrengthened OSB skin panel are commercially available and commonly used in building construction. The panel has a total thickness of 120 mm, consisting of two layers of 10 mm-thick OSB skins and a layer of 100 mm-thick EPS core. The dimension of the specimens tested is 1200*800mm. As will be demonstrated later in this paper, the panels under projectile impact suffered primarily localized punching shear failure. Therefore the height and width of the panel specimen have insignificant influence on its performance in resisting the projectile impact. The unstrengthened OSB skin SIP has been studied in (97). Some results are briefly presented here as reference to evaluate the effectiveness of the strengthening measures.

In this chapter, the reference panel is strengthened with one or two mesh layer(s). The strengthening layer can be an interlayer between the OSB skin and EPS core or on the front of the panel. Figure 6.3 illustrates the three positions of the strengthening layers considered in the study. The specimen A and B are strengthened with a layer of 6.5×6.5 mm spacing galvanized steel wire mesh and a layer of 10×10 mm spacing adhesive coated basalt fibre mesh interlayer between the front OSB skin and EPS core, respectively. The specimen C is strengthened with a layer of 10×10 mm spacing adhesive coated basalt fibre mesh on the front of the panel. The specimen D is strengthened with a 10×10 mm spacing uncoated basalt fibre mesh between the front OSB layer and EPS core. The specimen E is strengthened with a 5×5 mm spacing adhesive coated basalt fibre mesh interlayer. The specimen F is

strengthened with two layers of galvanized steel wire mesh interlayers between the EPS core and the front and back OSB skins. The specimen G is strengthened with two 10×10 mm spacing adhesive uncoated basalt fibre mesh interlayers.

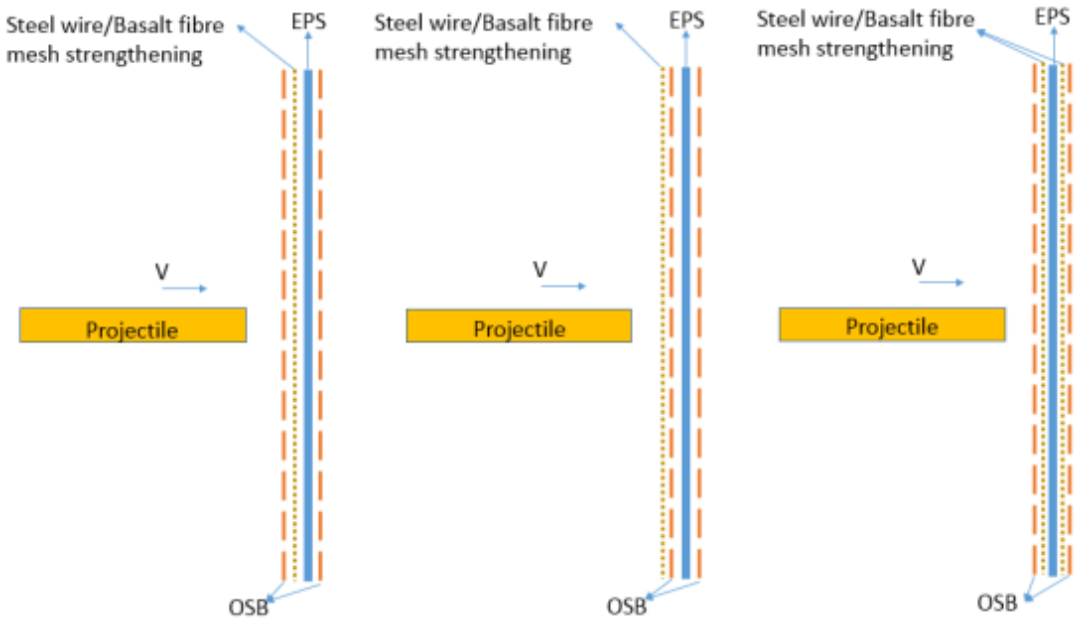


*Figure 6.3 Schematic diagram of steel wire mesh and basalt fibre mesh strengthening position (L) Interlayer strengthening (Specimen A/B/D/E); (M) Front strengthening (Specimen C); (R) Double interlayer strengthening (Specimen F/G)*

### 6.2.2 Experimental setup

The testing system includes an air cannon, a support frame, four halogen lights, two high speed cameras, and two recording computers as presented in Chapter 5.

### 6.2.3 Experimental results

In this study, the results were classified as “Pass” and “Fail” as per the Australian Wind Loading Code (AS/NZS 1170.2:2011) (19). “Pass” means no opening was created after the impact. “Fail” indicates either the debris penetrated the SIP panel or severe through cracks appeared on the SIP panel that allow wind blowing through the opening. The residual velocity of the debris, either passing through or rebounding, and the unpenetrated length of the projectile if the projectile stayed in the panel were also measured to compare the impact resistance capacity. In addition, the damage modes of each tested panel were also recorded. Together with the measured quantitative data, they are used to calibrate the numerical model. The detailed testing scheme and results are given in Table 6.2.

*Table 6.2 Testing scheme and results*

| Specimen | Strengthening method | Strengthening position | Testing result | Launching Velocity (m/s) | Residual Velocity (m/s) | Unpenetrated length of projectile (cm) |
|---|---|---|---|---|---|---|
| Reference panel (97) | Non-strengthened OSB skin SIP | NA | Fail(Stay) | 18.0 | 0 | NA |
| A-1st hit | Galvanized Steel wire mesh (Ø0.64mm, 6.5×6.5 mm spacing) | Interlayer | Fail | 22.8 | 7.7 | NA |
| A-2nd hit | | Interlayer | Fail(Stay) | 20.0 | 0 | 200 |
| B-1st hit | Adhesive coated Basalt fibre mesh(Ø1mm, 10×10 mm spacing) | Interlayer | Fail(Stay) | 20.0 | 0 | 470 |
| B-2nd hit | | Interlayer | Pass | 18.0 | -4.0 | NA |
| C-1st hit | Adhesive coated Basalt fibre mesh(Ø1mm, 10×10 mm spacing) | Front layer | Fail | 23.0 | 10.0 | NA |
| C-2nd hit | | Front layer | Fail(Stay) | 20.0 | 0 | 540 |
| D-1st hit | Uncoated basalt fibre mesh(Ø1mm, 10×10 mm spacing) | Interlayer | Fail(Stay) | 20.0 | 0 | 670 |
| D-2nd hit | | Interlayer | Pass | 18.0 | -4.8 | NA |
| E-1st hit | Adhesive coated basalt fibre mesh(Ø1mm, 5×5 mm spacing) | Interlayer | Pass | 16.0 | -2.0 | NA |
| E-2nd hit | | Interlayer | Fail(stay) | 20.0 | 0 | 750 |
| F-1st hit | Double galvanized Steel wire mesh(Ø0.64mm, 6.5×6.5 mm spacing) | Double Interlayer | Fail | 23.0 | 6.6 | NA |
| F-2nd hit | | Double Interlayer | Fail(stay) | 20.0 | 0 | 785 |
| G-1st hit | Double uncoated basalt fibre mesh(Ø1mm, 10×10 mm spacing) | Double Interlayer | Fail(stay) | 23.0 | 0 | 240 |
| G-2nd hit | | Double Interlayer | Pass | 20.2 | -4.6 | NA |

N.B “-” means rebound velocity after impact

### 6.2.3.1 Damage modes

The non-strengthened SIP panel in the previous study (97) is used as the reference panel in this study. The critical velocity was determined in the tests when the 4kg projectile penetrated the panel and stayed on it. With a higher or

lower velocity, the debris would penetrate through the panel with a punching shear failure mode or rebound back leaving an indentation on the panel, respectively. It was reported that the critical velocity of the non-strengthened SIP with the total thickness of 120 mm was 18 m/s. The global structural response such as panel bending was not observed after impact. The reference panel experienced localised punching shear failure as shown in Figure 6.4. Therefore, multiple impacts on the panel at different locations (97) were considered as independent events.

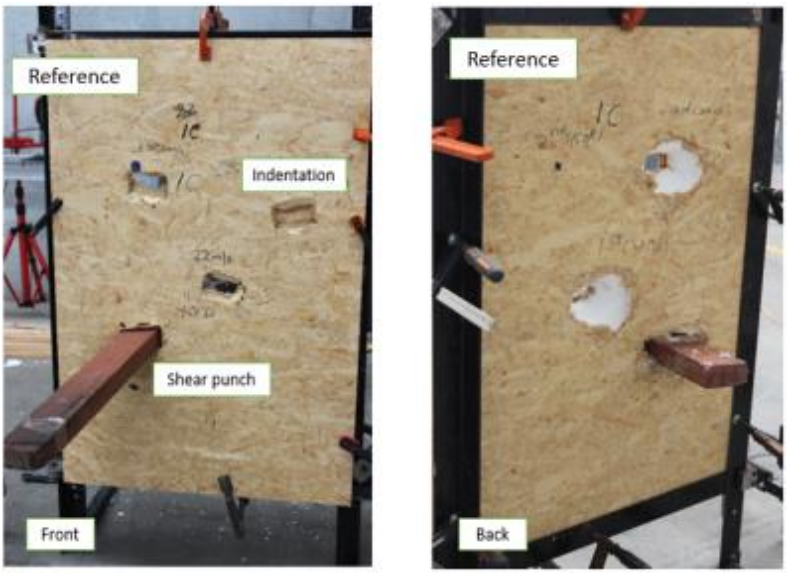


*Figure 6.4 Damage mode of the reference panel (97) (L) Front view; (R) Back view*

The specimen A strengthened with a steel wire mesh interlayer was subjected to two impacts at the velocities of 22.8 m/s and 20 m/s, respectively. Both impacts resulted in punching shear failure, indicating an addition of a layer of steel wire mesh to the panel does not prominently increase the ductility of the panel. The panel still experienced brittle punching shear failure due to projectile impact. No crack at the back OSB skin or boundary failure was observed as shown in Figure 6.5. The projectile with the launching velocity of 20 m/s penetrated and stayed on the panel. The impact velocity of 20 m/s is therefore identified as the critical velocity of the strengthened specimen A. Compared to the unstrengthened panel with the critical velocity of 18 m/s, strengthening the panel with a steel wire mesh interlayer only marginally increases its impact resistance capacity.

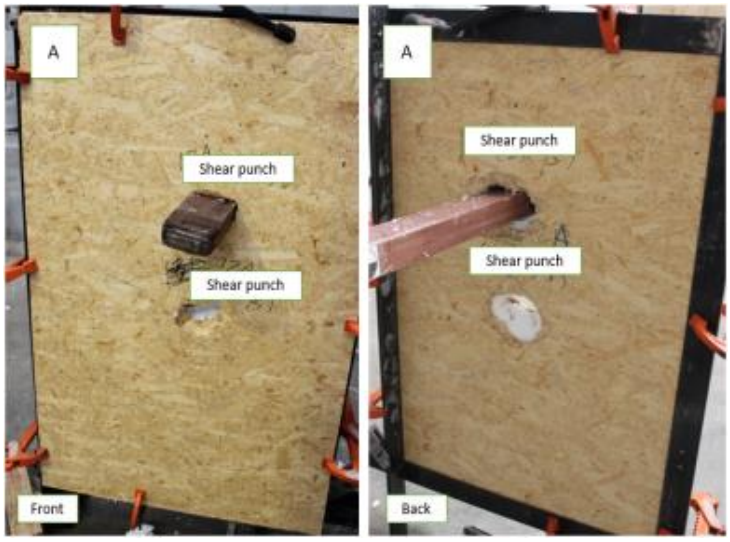


*Figure 6.5 Damage mode of specimen A strengthened with a steel wire mesh interlayer (L) Front view; (R) Back view*

The specimen B is a SIP strengthened with a 10×10 mm spacing adhesive coated basalt fibre mesh interlayer. A total of two impacts were conducted on this specimen. The impact with the velocity of 18 m/s had a result of “Pass” and left an indentation on the front OSB skin. As shown in Figure 6.6, the projectile with the velocity of 20 m/s penetrated and stayed on the panel, which led to a result of “Fail”. Neither crack at the back nor boundary failure after the impact was observed. The critical velocity is determined as 20 m/s for the specimen B. These results indicate that strengthening the panel with the ø0.64mm, 6.5×6.5 mm spacing steel wire mesh layer and the ø1mm, 10×10 mm spacing basalt fibre mesh layer have similar efficiency on the impact resistance capacity of the panel.

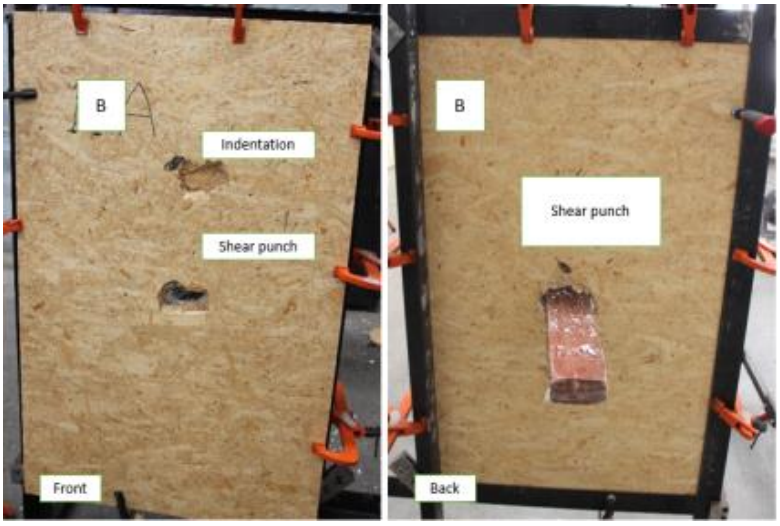


*Figure 6.6 Damage mode of specimen B strengthened with an adhesive coated basalt fibre mesh (10×10 mm spacing) interlayer (L) Front view; (R) Back view*

The specimen C is a SIP strengthened with a 10×10 mm spacing adhesive coated basalt fibre mesh at the front skin. Two impacts at the velocities of 22 m/s and 20 m/s were tested on this specimen. As shown in Figure 6.7, both impacts yielded the result of “Fail”. The projectile with impact velocity of 22 m/s penetrated through the panel and the projectile with 20 m/s impact velocity penetrated and stayed in the panel. The punching shear failure was observed after the impact. No crack at the back or boundary failure was observed after the two impacts. 20 m/s is again identified as the critical penetration velocity of the specimen C. These results indicate that placing the strengthening mesh layer on the front OSB skin or as an interlayer has the similar effectiveness on improving the impact resistance of the panel. These observations are different from those made in previous study (97), in which it was concluded that placing basalt fibre cloth at different locations affects the impact resistance capacity of the SIP. The results also indicated that the improvement on the impact resistance capacity by using steel and basalt fibre mesh is insignificant as compared to strengthening the panel with basalt fibre cloth.

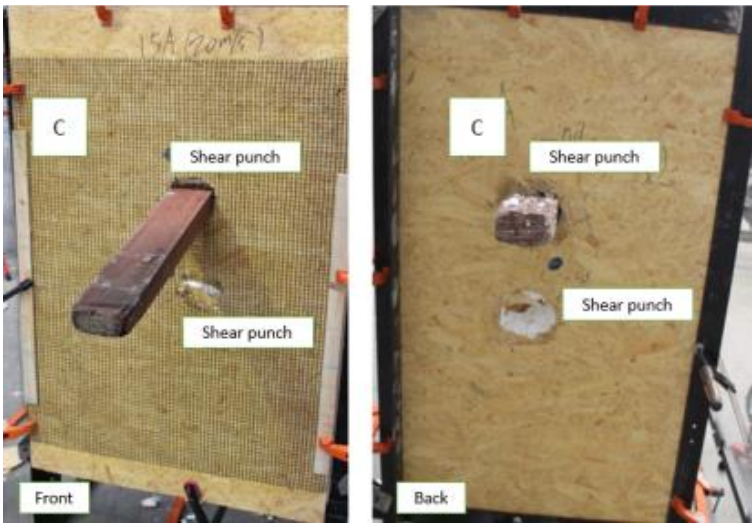


*Figure 6.7 Damage mode of specimen C strengthened with adhesive coated basalt fibre mesh (10×10 mm spacing) at front (L) Front view; (R) Back view*

The specimen D, similar to the specimen B, was strengthened with a 10×10 mm spacing basalt fibre mesh interlayer. The difference is that the specimen D used uncoated basalt fibre mesh while the specimen B used coated basalt fibre mesh. The specimen D was subjected to two impacts at the velocities of 20 m/s and 18 m/s, respectively. The panel experienced a typical punching shear failure and an indentation as shown in Figure 6.8. The 4kg projectile with velocity of 18 m/s impacted on the panel and rebounded with a velocity of 4.8 m/s. When the impact velocity was 20 m/s, the projectile penetrated and stayed on the panel. These results indicate that coating basalt fibre mesh has no effect on the impact resistance capacity of the panel. This is because the fibre mesh was coated with a very thin layer of epoxy resin. The strength of the epoxy

layer and the energy dissipated by the thin layer coating are trivial as compared to the high impact load and the total impact energy.

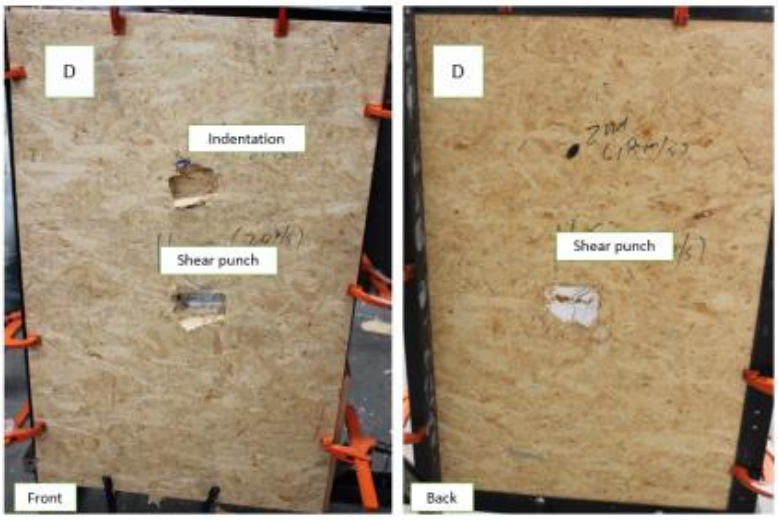


*Figure 6.8 Damage mode of strengthened specimen D with an uncoated basalt fibre mesh (10×10 mm spacing) interlayer (L) Front view; (R) Back view*

The specimen E was strengthened with an adhesive coated basalt fibre mesh interlayer (Ø1mm, 5×5 mm spacing). It was subjected to two projectile impacts at the velocities of 16 m/s and 20 m/s, respectively. As shown in Figure 6.9, the first projectile impact at 16 m/s left an indentation on the panel and the rebound velocity of the projectile was 2 m/s. The second projectile impact at 20 m/s penetrated the panel and stayed on it. No crack was observed at the back of the panel after two impacts. The critical velocity for the specimen E is therefore determined as 20 m/s. These results indicate that reducing the mesh spacing, in other words, using more dense fibre mesh has insignificant effects on the impact resistance capacity of the panel. As will be discussed later the panel strengthened with denser fibre mesh has slightly higher capacity than that with coarse mesh by comparing the projectile penetrated length, but the improvement in resisting the 4 kg projectile impact is negligible because of the large impact energy.

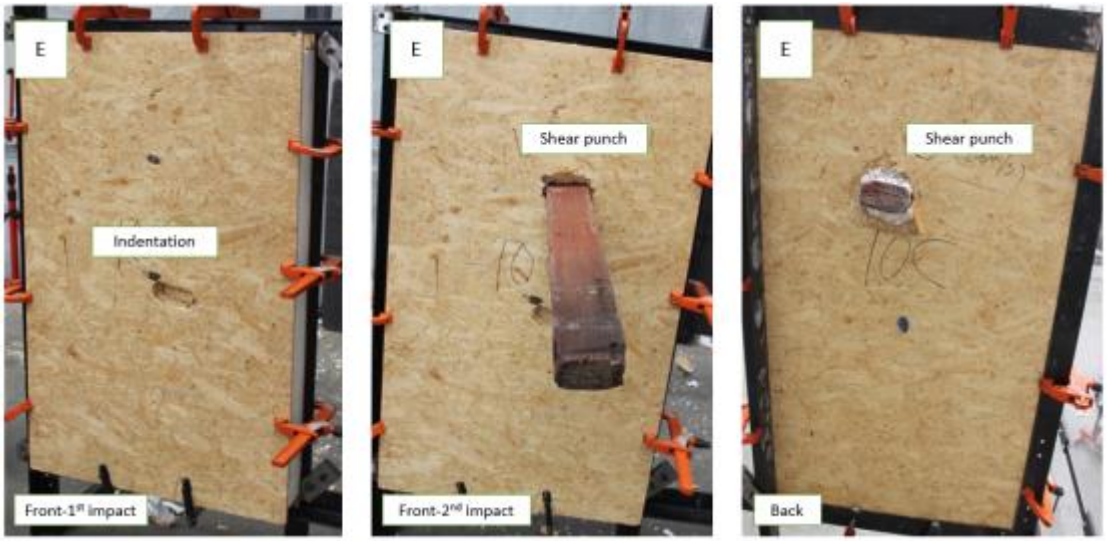


*Figure 6.9 Damage mode of specimen E strengthened with an adhesive coated basalt fibre mesh (5×5 mm spacing) interlayer (L) Front view-1st Impact 16 m/s; (M) Front view-2nd Impact 20 m/s; (R) Back view*

The specimen F was strengthened with two layers of steel wire mesh as double interlayers. It was subjected to two projectile impacts at the velocity of 23.0 m/s and 20 m/s, respectively. Both impacts caused localized punching shear failure on the panel as shown in Figure 6.10 and Figure 6.11. The projectile penetrated through the panel with a residual velocity of 6.6 m/s in the first impact. In the second impact, the projectile penetrated and stayed on the panel after the strike. The critical velocity is determined as 20 m/s for the specimen F. These results indicate that double-layer strengthening has similar effect as single layer strengthening in enhancing the impact resistance capacity of the SIP panel. This again could be attributed to the relatively low strength of the steel wire mesh as compared to the high projectile impact energy. As will be discussed later, using two layers of steel wire mesh indeed reduced the projectile penetration length, but it is not sufficient to prevent the projectile from piercing through the panel.

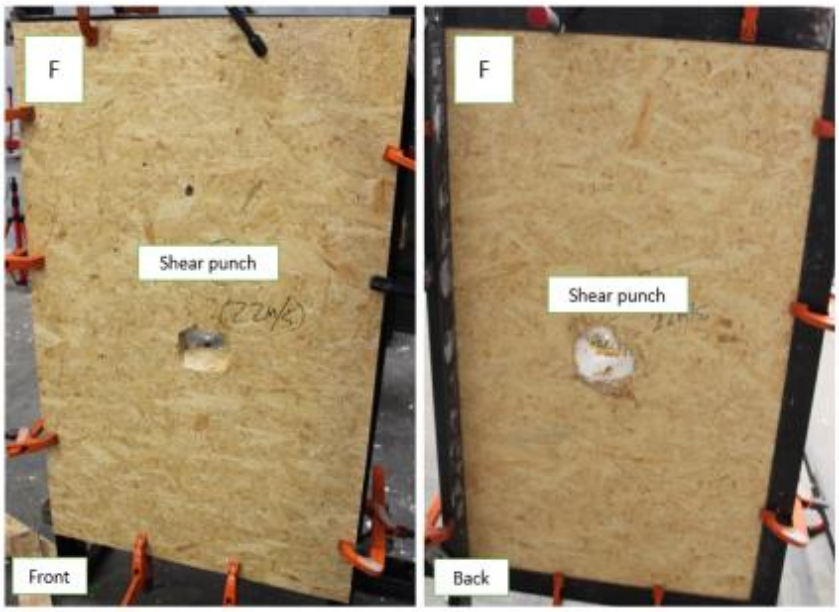


*Figure 6.10 Damage mode of specimen F strengthened with double steel wire mesh interlayers (1st impact 23 m/s) (L) Front view; (R) Back view*

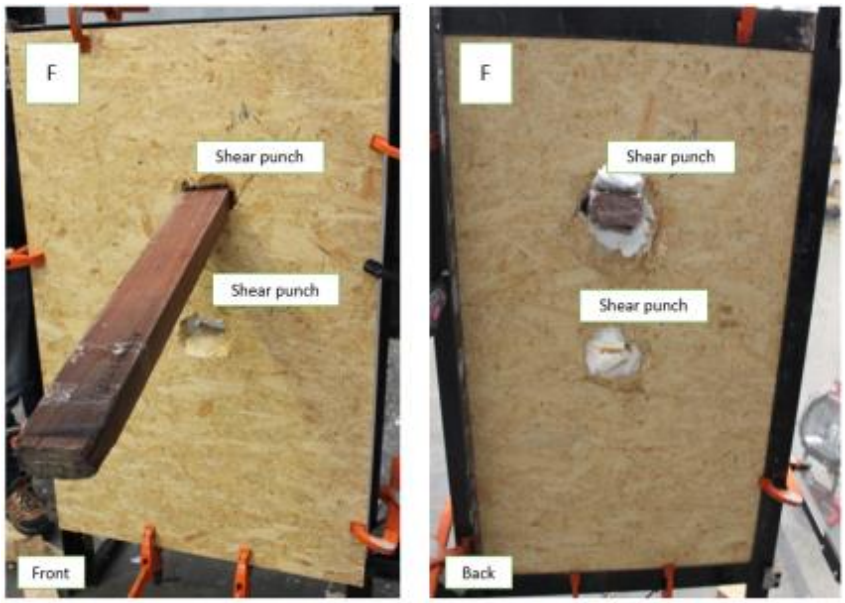


*Figure 6.11 Damage mode of specimen F strengthened with double steel wire mesh interlayers (2nd impact 20 m/s) (L) Front view; (R) Back view*

The specimen G was strengthened with two layers of uncoated basalt fibre mesh (Ø1mm, 10×10 mm spacing). The specimen was subjected to two impacts. The first projectile impact at the velocity of 23 m/s penetrated and stayed on the panel after impact as shown in Figure 6.12. The second projectile impact at the velocity of 20.2 m/s left an indentation on the front skin of the panel. A crack on the back OSB skin was also observed as shown in Figure 6.13. However, the testing result was specified as “Pass” since the crack was only observed at the back skin, therefore it is not a through crack. The front OSB skin and EPS core can prevent wind flowing through. The

critical velocity for the specimen G is therefore determined as 23 m/s. These results indicate the double basalt fibre mesh interlayer strengthened SIP could better resist the impact load than the double steel wire mesh strengthened SIP. This is because the basalt fibre mesh has higher tensile strength than the steel wire mesh used in this study.

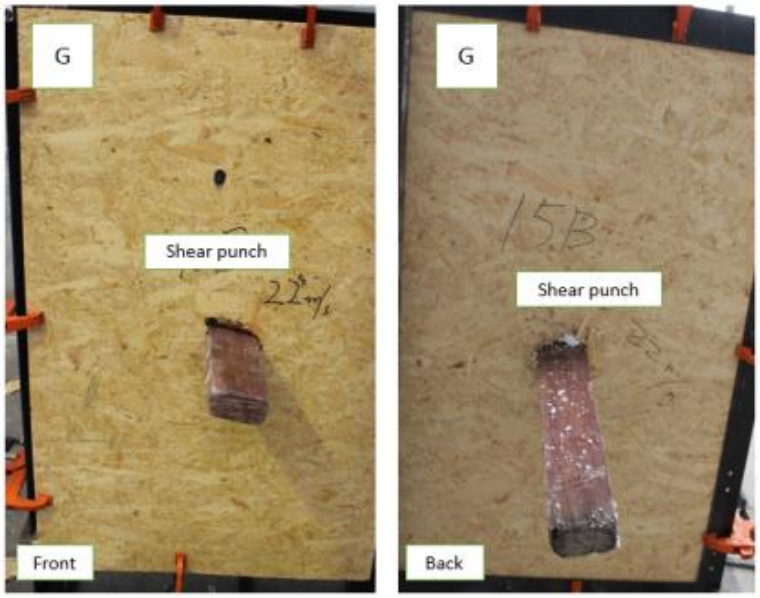


*Figure 6.12 Damage mode of specimen G strengthened with double uncoated basalt fibre mesh (10×10 mm spacing) interlayers (1st impact 23.0 m/s) (L) Front view; (R) Back view*

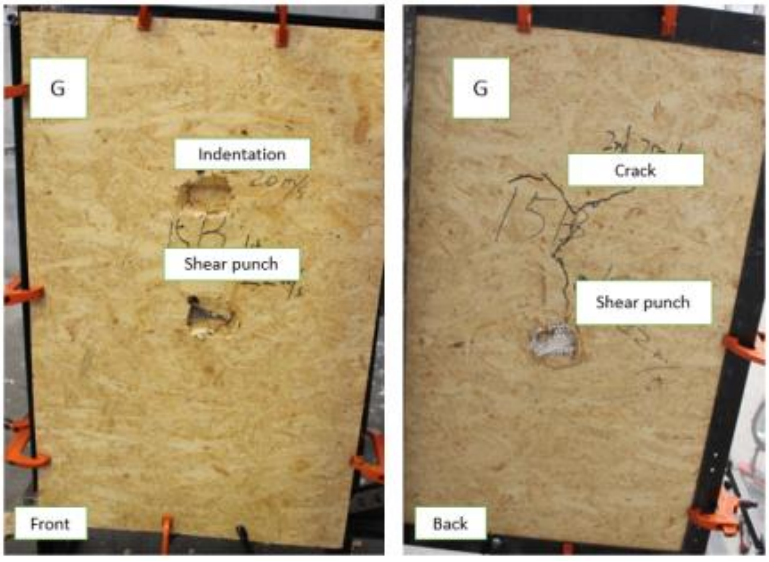


*Figure 6.13 Damage mode of specimen G strengthened with double uncoated basalt fibre mesh (10×10 mm spacing) interlayers (2nd impact 20.2 m/s) (L) Front view; (R) Back view*

### 6.2.3.2 Comparisons of different strengthened OSB skin SIPs

As given in last chapter, regarding the result of projectile impact on the reference panel, the critical velocity for the non-strengthened OSB skin SIP is 18 m/s. All the seven strengthened specimens tested in this study were demonstrated to have higher impact resistance capacity of different levels after

adding strengthening layer into the SIP. Due to the brittle attribute of the OSB skin and EPS foam material, the panel experienced localized punching shear failure and indentation damage. Only the specimen G survived the projectile impact at the velocity of 20 m/s. Therefore the enhancement on the impact resistance capacity of the panel by the strengthening techniques presented in the current study is only marginal, indicating steel wire mesh and basalt fibre mesh are not strong enough to strength OSB skin SIP to resist projectile impact.

As presented above, in impact tests, the projectile penetrated and stayed on six specimens (A, B, C, D, E and F) at the impact velocity of 20 m/s. Although the panels were considered failed because of creation of opening, the penetration length of the projectile is examined to analyse the impact resistance in more detail. Six specimens (A, B, C, D, E and F) showed different unpenetrated lengths of projectile, which were measured after testing to compare the impact resistant performance. As shown in Figure 6.14 and Table 6.2, the specimen A, B, C, D, E and F left 200 cm, 470 cm, 540 cm, 670 cm, 750 cm and 785 cm of projectile unpenetrated at the critical impact velocity of 20 m/s, respectively. Although these 6 panels are all considered having the same critical impact velocity of 20 m/s, the above results do indicate some different impact resistance capacities of the strengthening measures in terms of the strengthening material strength, wire mesh density, location and number of wire mesh layers. These are discussed in more detail below.


*Figure 6.14 Unpenetrated length of projectile (A/B/C/D/E/F) at the critical velocity of 20 m/s*

*a. The effect of strengthening materials on the unpenetrated length of projectile by comparing Specimen A and B; Specimen B and D; Specimen B and E; and Specimen F and G*

The projectile's kinetic energy was mainly absorbed by the penetration of the skins and EPS core with shear failure and the friction between the EPS core and the projectile. By comparing the unpenetrated projectile length of the specimen A strengthened with the 10x10 mm spacing steel wire mesh and the specimen B strengthened with10×10 mm spacing adhesive coated basalt fibre mesh, it can be concluded that specimen B has higher impact resistance capacity than specimen A because the respective unpenetrated projectile

length of specimens B and A are 470 cm and 200 cm, respectively. The difference in the impact resistance capacities of the two specimens can be attributed to the different wire mesh strength and a thin layer of epoxy coating in specimen B. Because the basalt fibre mesh has higher tensile strength than the steel wire mesh, the thin layer of epoxy coating, as discussed below, actually has adverse effects on impact resistance of the SIP panel.

Both specimen B and D were strengthened with the basalt fibre mesh of the same dimension at the same location. The difference is that specimen B was strengthened with adhesive coated basalt fibre mesh and the specimen D was strengthened with uncoated basalt fibre mesh. It was observed that the specimen B and D left 470 cm and 670 cm unpenetrated length of projectile, respectively, indicating applying a coating layer has adverse effects on the impact resistance capacity of the panel. The reason might be the uncoated fibre strip could deform to dissipate more energy than the adhesive coated fibre strip when it is subjected to projectile impact. In other words, attaching the mesh with epoxy coating makes it more vulnerable to brittle punching shear damage.

The influences of mesh spacing are discussed by comparing the performance of specimens B with 10×10 mm spacing adhesive coated basalt fibre mesh and the specimen E with 5×5 mm spacing adhesive coated basalt fibre mesh. The unpenetrated length of the projectile into specimen B and E is 470 cm and 750 cm, respectively, indicating reducing the mesh spacing increases the performance of the strengthened panel, as expected. Increasing the density of the basalt fibre mesh can enhance the energy dissipation ability of the strengthened panel. The specimen E (5×5mm spacing coated basalt fibre mesh interlayer strengthened SIP) is considered as the most effective single layer strengthened SIP against projectile impact, among the single-layer strengthened panels considered in this study.

The specimen F and G were strengthened with double layers of steel wire mesh and uncoated basalt fibre mesh (10×10mm spacing), respectively. As expected, the SIP strengthened with double layers outperformed all panels strengthened with a single layer mesh. The projectile penetrated the specimen F with the longest unpenetrated length of 785 cm at the velocity of 20 m/s. The specimen G strengthened with double layers of uncoated basalt fibre mesh (10×10mm spacing) had a higher critical velocity of 23 m/s than the specimen F due to the higher tensile strength of basalt fibre material. The specimen G with double basalt fibre mesh interlayer strengthening has the highest impact resistance capacity among the seven strengthened panels considered in this study.

*b. The effect of strengthening location on the unpenetrated length of projectile by comparing Specimen B and C*

The specimen B and C were strengthened with the same layer (adhesive coated basalt fibre mesh) but at different locations. The interlayer strengthened specimen B left 470 cm unpenetrated length of projectile and the specimen C strengthened on the front of the panel left 540 cm unpenetrated length of projectile, respectively, which indicates that the front strengthening is more effective than placing the strengthening layer as an interlayer. For the interlayer strengthened specimen B, the mesh layer is backed with soft EPS foam. The improvement of impact resistant capacity of the panel is limited owing to the mesh layer is easier to be stretched and penetrated under projectile impact. The mesh layer attached on the easily-deformed EPS material is prone to fail as compared to that attached on the rigid (OSB) surface. Therefore, the front strengthening method can provide slightly better impact resistance performance due to its enhancement of the penetration resistant capacity of the front OSB skin.

## 6.3 Numerical simulation

### 6.3.1 Finite element model

The numerical model shown in Figure 6.15 is developed by using commercial software ANSYS. The software LS-PREPOST is used to pre-process and post-process the simulation. The numerical model of the non-strengthened OSB skin SIP was verified in last chapter (97). In this study, two finite element models are further developed by including the 6.5×6.5 mm spacing steel wire mesh (ø0.64mm) interlayer strengthened SIP A and the 10×10 mm spacing coated basalt fibre mesh (ø1mm) interlayer strengthened SIP B. The accuracy of the numerical models of the strengthened panels is verified by comparing with the experimental results. The residual velocity of the projectile after impact is used to calibrate the finite element model. In the numerical model, the basalt fibre mesh and steel wire mesh are modelled by using beam element. OSB skin and EPS core are modelled with solid element. Based on the mesh convergence test in the previous study (16), the impact area is modelled with dense (5*5*5 mm) solid element, and the rest of the panel is modelled with 25*25*5 mm and 25*5*5 mm solid element. The steel wire mesh and the basalt fibre mesh in panel are modelled with 6.5 mm and 5.0 mm beam elements according to the physical sizes of mesh units, respectively. Owing to the symmetrical behaviour of the panel, only a quarter of the panel is modelled to simulate the dynamic response of the panel subjected to debris impacts.

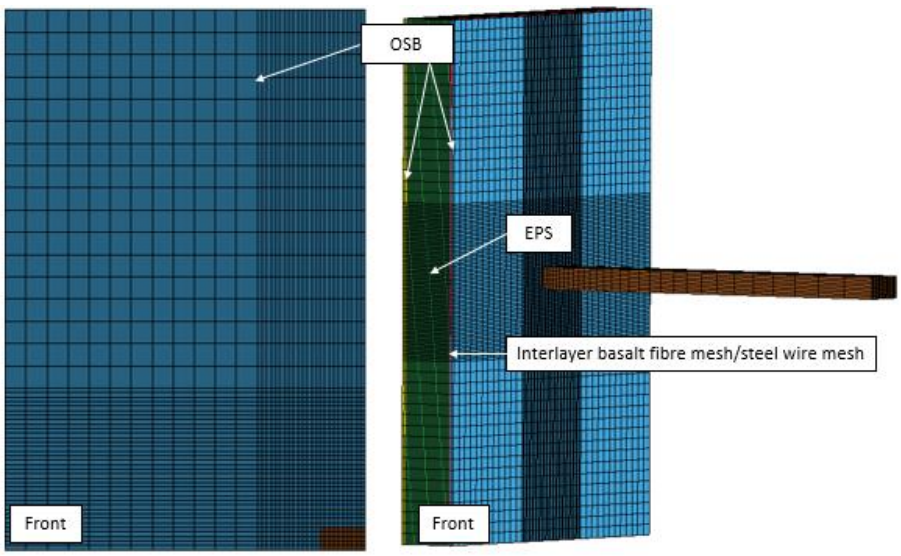


*Figure 6.15 Numerical model (L) Quarter model (front view); (R) Reflected full model (angled view)*

#### 6.3.1.1 Element types and boundary conditions

The OSB skin and EPS foam are modelled by using constant stress single integration node solid elements. The steel wire mesh and the basalt fibre mesh are modelled by using Hughes-Liu with cross section integration beam element. The timber debris is modelled by using eight-node solid elements. In the tests, all specimens were clamped onto the support frame by using G-clamps all along the boundary of the panel. The keyword of *BOUNDARY SPC SET is used in the numerical model to simulate the fully fixed boundary condition.

#### 6.3.1.2 Material models

The numerical model was built based on the calibrated model in the last chapter (97, 98). The material models *MAT 24, *MAT 163, *MAT 143 and *MAT 20 in LS-Dyna are used to model the mesh layer, EPS foam, OSB skin and timber debris, respectively.

As reported in (169), steel wire mesh exhibits elastic-plastic behaviour, which can be simulated by using *MAT 24 (*MAT PIECEWISE LINEAR PLASTICITY) in LS-DANA (168). The elastic-plastic material model *MAT 24 has been widely used to simulate the reinforcement in the concrete structure (170). Basalt fibre cloth was modelled by shell elements by using *MAT 54 (i.e. *MAT ENHANCED COMPOSITE DAMAGE) in the previous study (97). However, the *MAT 54 is not applicable to beam element in LS-DYNA. In this model, the basalt fibre mesh is modelled with *MAT 24 since the basalt fibre exhibits approximately linear elastic behaviour before its failure. The failure criteria for basalt fibre mesh are defined by the tensile strength. The failure of steel wire mesh is defined by both failure strain and yield strength. The parameters of the steel wire mesh and basalt fibre mesh used in the numerical models are listed in Table 6.3.

*Table 6.3 Material properties of steel wire mesh and basalt fibre mesh*

| *Steel wire mesh (*MAT 24 PIECEWISE LINEAR PLASTICITY)* | | *Basalt fibre mesh (*MAT 24 PIECEWISE LINEAR PLASTICITY)* | |
|---|---|---|---|
| Mass density (kg/m$^3$) | 7800 | Mass density (kg/m$^3$) | 2750 |
| Young's modulus (Pa) | 2.10E+11 | Young's modulus (Pa) | 8.90E+10 |
| Poisson's ratio | 0.3 | Poisson's ratio | 0.26 |
| Yield strength (Pa) | 3.00E+08 | Tensile strength (Pa) | 4.80E+09 |
| Tangent modulus (Pa) | 7.700e+08 | | |

#### 6.3.1.3 Contact algorithm

Four types of contact algorithm are used to simulate the contact in the numerical models of steel wire mesh strengthened SIP and basalt fibre mesh strengthened SIP. *ERODING SINGLE SURFACE is used to define the contact between the projectile and the strengthened panel. *CONTACT ERODING SURFACE TO SURFACE is applied between each contact surface, such as the contact between the EPS foam core and OSB panel. *NODES TO SURFACE is used to model the contact for impact involving the layer of steel wire mesh and the layer of basalt fibre mesh. In the previous study (97), debonding was found between the strengthening layer and the skin layer after projectile impact. Slight debonding was also observed between the wire mesh and the OSB layer in the test. *TIEBREAK NODES TO SURFACE is deployed in the model to simulate the bonding between the steel wire/ basalt fibre mesh and the OSB layer, as well as between the steel wire/ basalt fibre mesh and the EPS foam core.

### 6.3.2 Comparisons between experimental and numerical simulation results

The testing results of two specimens (i.e. specimen A/B) subjected to four hits in total are used to verify the accuracy of the finite element models. The specimen A is strengthened with steel wire mesh (ø0.64mm, 6.5×6.5 mm spacing) as interlayer and the specimen B is strengthened with coated basalt fibre mesh (10×10 mm spacing, ø1mm) as interlayer. It should be noted that both panels experienced localised punching shear failure under projectile impacts. In the numerical model, all impacts are modelled as individual event to strike the centre area of the specimen. The numerical results are compared with the testing results in terms of damage mode and the residual velocity of the projectile after impact, which are given in Table 6.4.

*Table 6.4 Comparisons between testing results and numerical results*

| Specimen | Launching velocity ($V_I$) | | Residual velocity ($V_R$) | | Error |
|---|---|---|---|---|---|
| | Test | Numerical | Test | Numerical | |
| A-1$^{st}$ hit | 22.8m/s | 22.8m/s | 7.7m/s | 7.32 m/s | -4.94 % |
| A-2$^{nd}$ hit | 20.0 m/s | 20.0 m/s | 0 m/s | 0 m/s | 0% |

| | | | | | |
|---|---|---|---|---|---|
| B-1st hit | 20.0 m/s | 20.0 m/s | 0 m/s | -0.34 m/s | N/A |
| B-2nd hit | 18.0 m/s | 18.0 m/s | -4.0m/s | -3.89m/s | 2.75 % |

N.B "-" means rebound velocity

#### 6.3.2.1 Specimen A

The specimen A was subjected to the first projectile impact at the velocity of 22.8 m/s. As shown in Figure 6.16, the specimen A experienced typical punching shear failure and the projectile penetrated through the panel. The damage mode can be well captured by the numerical simulation, i.e. shear failure of the steel wire mesh at the impact location, and new debris generated after the impact. The predicted residual velocity for the first impact is 7.32 m/s, which is 4.94% lower than the experimental result. The second impact on the specimen A was carried out with a lower velocity of 20 m/s. The projectile penetrated and stayed on the panel with localised punching shear failure as shown in Figure 6.17. The numerical results well agree with the testing results for the specimen A.

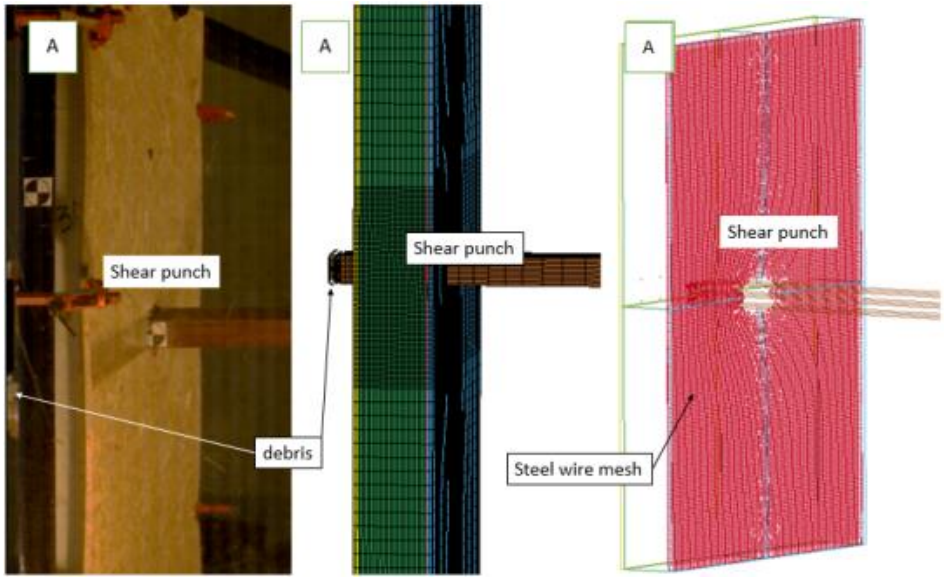


*Figure 6.16 Comparisons of damage mode of the specimen A (1st impact 22.8 m/s); (L) Test; (M) Numerical; (R) Numerical (the layer of steel wire mesh)*

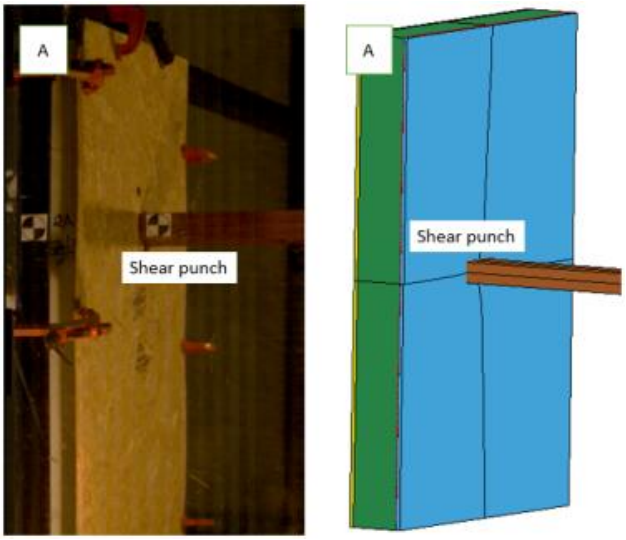


*Figure 6.17 Comparisons of damage mode of the specimen A (2nd impact 20 m/s); (L) Test; (R) Numerical*

### 6.3.2.1 Specimen B

The specimen B was also subjected to two projectile impacts at the velocities of 20 m/s and 18 m/s, respectively. As shown in Figure 6.18, a clear localised punching shear failure was observed in experimental test and numerical simulation when the specimen was subjected to 20 m/s projectile impact. The projectile at the first hit penetrated and stayed on the panel in the test while the projectile rebounded with a velocity of 0.34 m/s in the numerical simulation, indicating the numerical simulation slightly over predict impact resistance capacity of the panel. The second projectile impact at the launching velocity of 18 m/s rebounded in both test and numerical simulation. As given in Table 6.2, the rebound velocity from the test is 4 m/s and the numerical result is 3.89 m/s, with an error of 2.75%. These results indicate that the numerical model can give good predictions of the panel responses to the projectile impact.

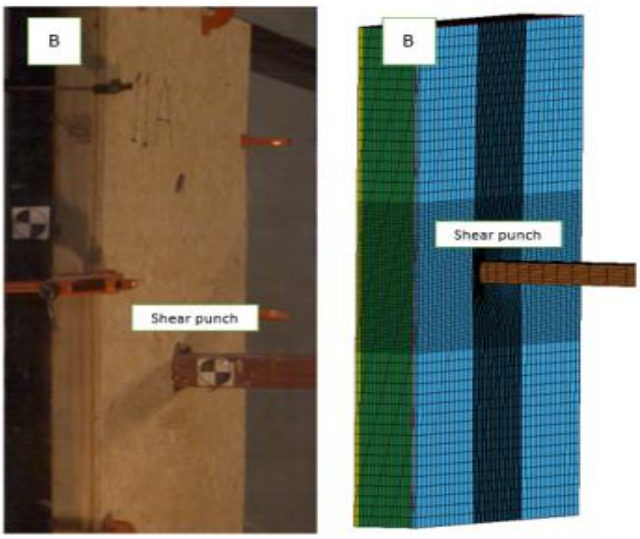


*Figure 6.18 Comparisons of damage mode of specimen B (1st impact 20 m/s); (L) Test; (R) Numerical*

## 6.4 Summary

In this chapter, experimental investigations have been conducted to study the effectiveness of using the steel wire mesh and basalt fibre mesh to strengthen OSB skin SIP to resist windborne debris impact. A total of seven strengthened SIP specimens were tested. It was found that the damage modes included indentation and punching shear failure. The application of steel wire mesh in this study was found less effective than basalt fibre mesh to enhance the impact resistance capacity of the SIP panel. Coating the basalt fibre mesh with a thin layer of epoxy was found having adverse effect on the impact resistance of the panel. Placing the wire mesh layer on the front OSB surface was found more effective than placing the strengthening layer between the OSB skin and EPS core. While the wire mesh has advantages of light weight and cheap, using wire mesh to strengthen the SIP panel only marginally increases the impact resistance of the panel. Increasing the mesh strength and density has obvious effect in enhancing the performance, but the cost also increases. Therefore, a balance needs to be sought in practice based on detailed analysis.

# Chapter 7 Experimental and numerical study on the basalt fibre cloth strengthened structural insulated panels under windborne debris impact

## 7.1 Introduction

Different fibres including carbon fibre (CFRP), glass fibre (GFRP) and basalt fibre (BFRP) can be used to strengthen SIPs. The effectiveness of using different fibres on strengthening structures has been studied. Wu et al. (82) tested concrete columns strengthened by applying CFRP and BFRP, respectively. The results showed that concrete columns strengthened with BFRP had comparable capacities with those strengthened with CFRP in terms of shear resistance and energy dissipation. Sim et al. (171) conducted Alkali-resistance testing and found that basalt fibre had better durability performance than glass fibre and better performance than carbon fibre on the thermal stability. Compared to the two most commonly studied fibres, i.e., carbon fibre and glass fibre, basalt fibre outperforms glass fibre in terms of strength and stiffness and deformation capability. Its strength and stiffness are lower than those of carbon fibre, but it has better deformation capability, i.e., more ductile than carbon fibre, implying possibly higher energy absorption capacity under impact loads than carbon fibre. As basalt fibre is cheaper than carbon fibre and has better mechanical properties than glass fibre, strengthening SIPs with basalt fibre cloth might be a practical solution for enhancing their capability to resist debris impacts in order for their applications in strong wind regions.

This chapter investigates the effectiveness of using basalt fibre cloth to strengthen SIPs with OSB skins on their capacity in resisting windborne debris impact. Four strengthened SIPs and one referencing panel without strengthening were tested. An air cannon testing system was used to launch a 4kg hardwood projectile with cross section of 50*100 and 900 mm length. The behaviours of the SIPs under projectile impact are presented and the efficiency of using basalt fibre cloth to strengthen the panel on its impact resistance capacity is discussed. A numerical model is also developed by using LS-DYNA to simulate the responses of the strengthened SIPs. The numerical simulation results are compared with the experimental results to verify the accuracy of the model. The calibrated numerical model can be used in the future to perform parametric simulations to study the performance of SIPs with OSB skins of different material, dimension, geometric and boundary conditions subjected to different scenarios of projectile impacts.

## 7.2 Experimental investigation

A total of five specimens (i.e. A/B/C/D/E) were manufactured and tested by using an air cannon system. The damage modes were observed and the structural responses including residual velocity of projectile was recorded by using two high speed cameras. The specimens and experimental setup are detailed below.

### 7.2.1 Description of specimens

All specimens have the identical dimension of 1200*800*120 mm. The non-strengthened specimen A consists of EPS foam core and two OSB face sheets. The specimens B/C/D/E are the SIPs strengthened by applying a basalt fibre cloth layer between the front OSB face sheet and EPS core as an additional interlayer(B and C), on front surface of the OSB face sheet(D) and on back OSB sheet(E), respectively as illustrated in Figure 7.1. The thickness of the OSB, EPS and basalt fibre cloth are 10 mm, 100 mm and 1mm, respectively. With different manufacturing process, the strength of basalt could range from 1600 MPa (172) up to approximately 4800MPa (37). The tensile strength of the basalt fibre used in this study is 4800 MPa and the density is 2750 kg/m$^3$ from the manufacturer. EPS, OSB and basalt fibre cloth are bonded together by using adhesive with bonding strength of 6-7 MPa (16). The detailed material properties of EPS, OSB and timber projectile are given in Section of numerical simulation in this paper.

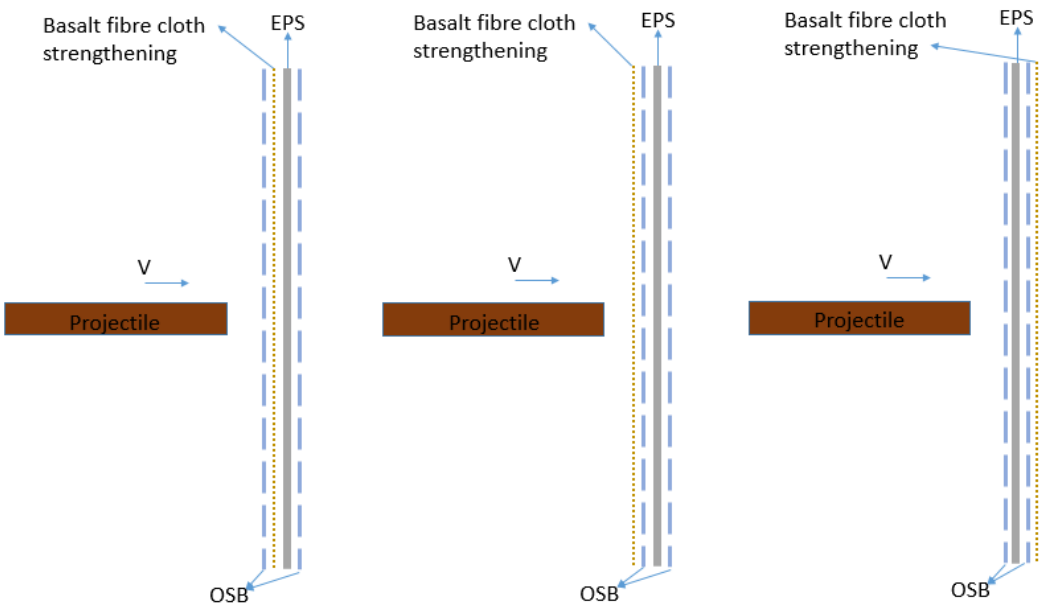


*Figure 7.1 Schematic diagram of Basalt fibre strengthening (L) Interlayer strengthening (Panel B/C) (M) Front surface strengthening (Panel D); (R) Back surface strengthening (Panel E)*

### 7.2.2 Experimental setup

The testing system includes an air cannon, a support frame, four halogen lights, two high speed cameras, and two recording computers as stated in Chapter 5.

### 7.2.3 Experimental results

The Australian wind loading code (AS/NZS 1170.2:2011)(19) specifies the result of windborne debris impact testing as pass or fail only. In this study, the residual velocity was measured for better understanding of the impact resistance capacity and also for calibrating the numerical model.

Understandably this criterion is established based on the consideration of structural safety because increased internal wind pressure due to opening would endanger the integrity of the building as reviewed above. However, in the tests, as will be reported in this paper, a new failure mode was observed, which did not occur in our previous testing of unstrengthened OSB SIPs (173), i.e., basalt fibre cloth stopped wood projectile from penetrating through the panel, but large impact force caused significant damages to the back OSB skin with debris from the damaged skin flying behind the panel. Since the primary function of a structural wall or panel is for people and property protection, occurrence of any damage that threats the safety of people behind the panel should also be considered as the failure of the structure. In this regard, the tested panel is considered as failed if secondary debris from damaged back OSB skin is observed although this is not defined in the current code. Therefore, the critical velocity in this study for assessing the panel failure represents either the projectile penetrated through the tested panel or secondary debris from damaged back OSB skin was generated. The experiment results are summarized in Table 7.1.

*Table 7.1 Test configuration and results*

| Specimen | Strengthening strategy | Testing result | Impact Velocity (m/s) | Residual Velocity (m/s) |
|---|---|---|---|---|
| A (Reference panel) | None | Fail(Stay) | 18.0 | 0 |
| B-1st hit | Interlayer | Pass | 22.0 | -6.0 |
| B-2nd hit | Interlayer | Pass | 26.8 | -5.0 |
| C-1st hit | Interlayer | Pass | 27.0 | -5.0 |
| C-2nd hit | Interlayer | Fail | 33.0 | -2.7 |
| D-1st hit | Front layer | Pass | 27.7 | -6.8 |
| D-2nd hit | Front layer | Fail | 34.0 | 0 |
| E | Back layer | Fail(Stay) | 32.0 | 0 |

N.B “-” means rebound velocity

#### 7.2.3.1 Damage modes

The specimen A was subjected to four repeated projectile impacts with speeds of 15, 21.2, 18, and 20 m/s, respectively. The corresponding results were pass, fail, fail and fail. When it was impacted at velocity 15 m/s, the projectile damaged the front OSB skin with an indentation. When impacted by the projectile at 21.2m/s and 20 m/s, the projectile penetrated through the panel. When impacted by the projectile at 18 m/s, the projectile also penetrated, but stayed in the panel as shown in Figure 7.2. Since at 18 m/s impact velocity the projectile perforated but stayed in the panel, the speed of 18 m/s was deemed as the critical speed to penetrate the specimen. It should be noted that, as shown in Figure 7.2, the damage of the panel was limited to a localised area due to punching shear damage. No overall structural response of the panel, i.e., bending and shear response was observed. Therefore each impact could be considered independent and did not affect the responses of the panel subjected to the subsequent impacts at different locations.

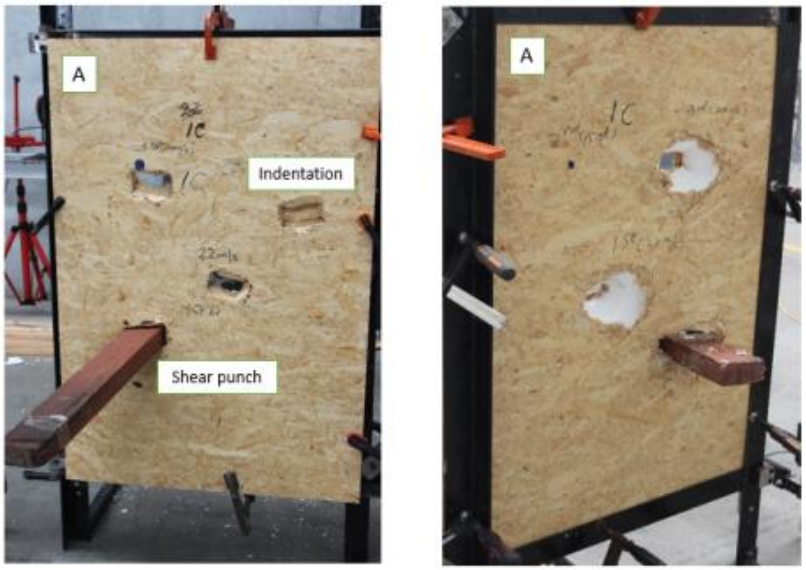


*Figure 7.2 Photograph of specimen A (L) Front view; (R) Back view*

The interlayer-strengthened specimen B, as shown in Figure 7.3, was subjected to two impacts at the velocity of 22 m/s and 26.8 m/s, respectively. The test results were pass and pass. As shown both strikes left indentation on the front OSB skin, small cracks were induced on the back OSB skin by the projectile strike at velocity 26.8 m/s, the cracks did not penetrate through the panel that could result in wind leaking through them. Therefore the panel is considered survived the impact.

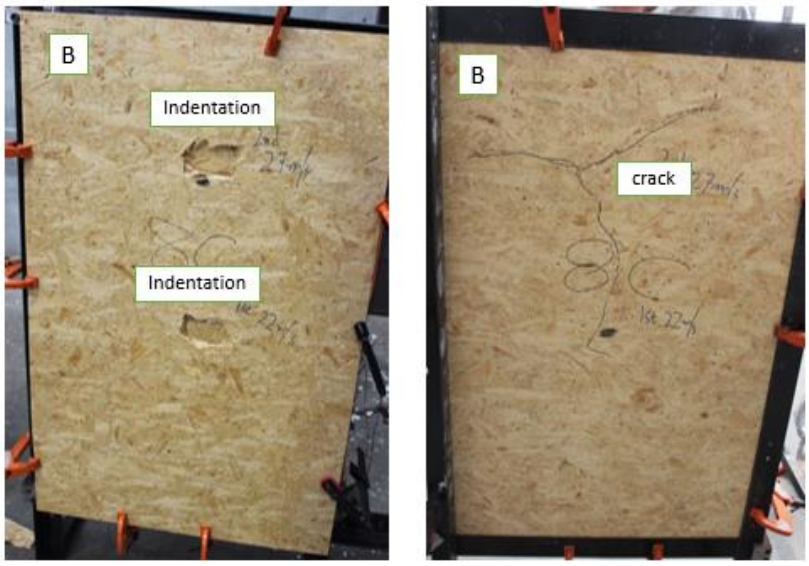


*Figure 7.3 Photograph of specimen B (L) Front view; (R) Back view*

The specimen C was also strengthened with a basalt fibre cloth as specimen B. It was impacted twice respectively at a velocity of 27 m/s and 32 m/s. The damage modes of the panel are shown in Figure 7.4. The panel rejected the projectile in both strikes with rebound velocity of 5.0 m/s and 2.7 m/s, respectively. Both strikes caused an indentation on the front OSB skin. The 32 m/s strike caused large cracks and complete failure of the back OSB layer as shown in Figure 7.4. Secondary debris caused by the fracture of the back OSB skin and EPS core was observed. The testing results for the 27 m/s and 32 m/s strikes were classified as “pass” and “fail”. Although the basalt fibre cloth rejected the projectile at velocity 32 m/s, the panel was considered failed because large cracks and damage in OSB skin and EPS core made the panel not possible to block wind from blowing through the panel.


*Figure 7.4 Photograph of specimen C (L) front view; (R) Back view*

The specimen D with a basalt fibre cloth glued to the front OSB skin was also tested twice. In the first test, the projectile impact velocity was 27 m/s. The strengthened panel rejected the projectile with a rebound velocity of 6.8 m/s. The projectile indented the panel and caused some wrinkling of the fibre cloth due to debonding of the cloth from the OSB skin as shown in Figure 7.5. The most significant debonding failure occurred at the bottom right quarter of the panel. Detailed examination of the impact location and the high speed camera images in Figure 7.6 revealed that although the projectile was aimed at the centre of the panel, the actual impacted location was slightly off the centre to the right upper quarter of the panel, with an eccentricity of 2 cm to the right side and 2 cm above the centre location. Moreover, as shown in Figure 7.6, the projectile impacted the panel at a slightly tilted angle, which is approximately 2 degree between the horizontal line and the projectile trajectory, owing to the air cannon was positioned with a slightly tilted angel to the horizontal line. As will be proven later in numerical simulations, these are the primary factors that caused unsymmetrical damage of the panel. As shown, the back OSB skin of the panel remained undamaged. Therefore the panel passed the projectile impact at 27 m/s. Figure 7.7 shows the damage mode of the panel subjected to a second projectile impact at a velocity of 34 m/s. As shown severe damage was induced by this impact, a large indentation was observed on the front skin with significant basalt fibre cloth debonding on the top section of the panel near the impacted location. The fibre cloth was also pulled out from the top boundary of the panel. The back OSB skin and EPS core near the impacted location were also completely fractured. Therefore the panel did not survive the projectile impact at velocity 34 m/s.


*Figure 7.5 Photograph of specimen D-1st strike (L) Front view; (R) Back view*


*Figure 7.6 Comparison of designed test and actual test condition (L) eccentricity; (R) tilted projectile impact angle*


*Figure 7.7 Photograph of specimen D-2nd strike (L) Front view; (R) Back view*

Figure 7.8 shows the damage mode of the specimen E with a basalt fibre cloth glued to the back OSB skin. As shown at impact velocity 32 m/s, the projectile penetrated into the panel but was stopped by the basalt fibre cloth. No perforation of basalt fibre cloth was observed. The panel with a layer of basalt fibre cloth on its back surface successfully stopped the projectile. However, as can be observed in Figure 7.8, impact force caused large panel deformation, which resulted in panel failure along the left and bottom boundary. The basalt fibre cloth was partially torn along the boundary and significant debonding between the basalt fibre cloth and the OSB back skin was also observed. Since boundary failure could lead to total collapse of the panel, and also create an opening for wind to leak through, the panel was then considered as failed the projectile impact at a velocity of 32 m/s.

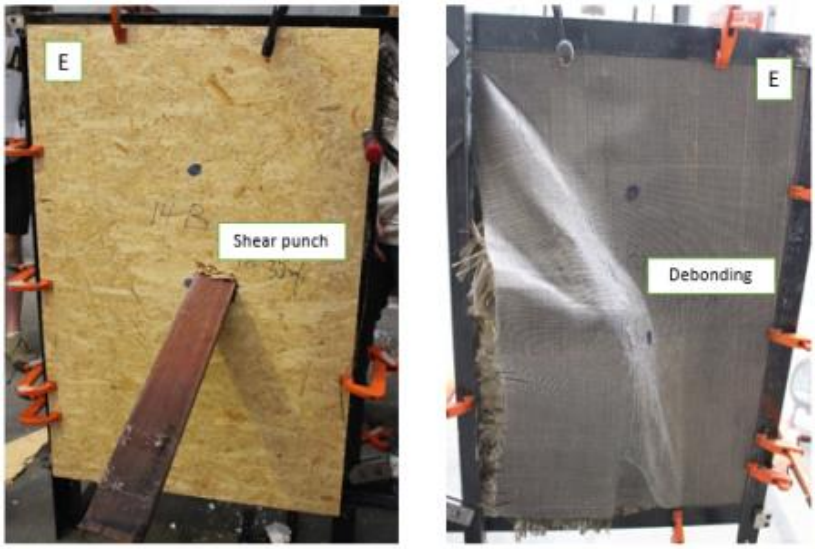


*Figure 7.8 Photograph of specimen E (L) Front view; (R) Back view*

### 7.2.3.2 Comparison and discussion

As observed from the testing results, the panel without basalt fiber strengthening was easily penetrated through due to the brittleness of OSB skin and weak EPS core. The specimen A without basalt fibre cloth strengthening was breached by the projectile at the critical velocity of 18 m/s. The panels B/C/D/E with basalt fibre cloth strengthening showed better impact-resistant performance.

As one of the two specimens strengthened with a fibre cloth as an interlayer, the specimen B rejected the projectile at the impact velocity of 22 m/s and 26.8m/s with damages only observed on the front OSB skin. The specimen C with the same strengthening as Specimen B rejected the first projectile strike at the velocity of 27 m/s, causing an obvious indentation on the front skin and small cracks on the back OSB skin. The second strike at the velocity of 33 m/s on the specimen C generated large fractures on the back OSB skin and pushed out the EPS material near the impacted location. These testing results indicate that strengthening the SIP panel by placing a 1 mm thick basalt fibre cloth inside the panel as an interlayer increases its capacity to resist the projectile impact from a velocity of 18 m/s to 27 m/s. Basalt fibre stopped the projectile from penetrating through the panel even at an impact velocity of 33 m/s. No basalt fibre failure was observed in the tests. However, it should be noted that in practice it is difficult to strengthen an existing panel by adding an interlayer. This strengthening scheme is investigated to examine the effectiveness and possibility of fabricating new panels to resist debris impact.

The specimens D and E with basalt fibre strengthening respectively on the front OSB and back OSB skin also demonstrated a significant increment in the panel capacity to resist projectile impact. Like specimen C, basalt fibre cloth successfully stopped projectile from penetrating through the panel and no fibre

rupture was observed. Panel damage was related to significant OSB skin rupture with secondary debris or boundary failure. For the three strengthening schemes, the increments in the resistance capacity are quite similar, i.e., the critical impact velocity of the panel increases from 18 m/s to 27 m/s. The basalt fibre stopped projectile from penetrating through the panel even at impact velocity of 32-34 m/s. However, at these high impact velocities, some secondary debris from the failed back OSB skin and EPS core was observed in the specimen C with placing the basalt fibre cloth as an interlayer, and the specimen D with placing the cloth on the front OSB skin, which could impose some threats to the people and contents behind the panel. Therefore the strengthening scheme with basalt fibre placed on the back OSB skin, i.e., specimen E, is a better choice since the fibre cloth worked as a catcher to prevent the secondary debris from the back OSB skin flying into the room. Moreover, placing basalt fibre cloth at the back skin also increases the flexural resistant capacity of the panel (174), which is important for the panel subjected to external wind pressure. This, however, is beyond the scope of the current study.

## 7.3 Numerical simulation

### 7.3.1 Finite element model

In this chapter, the numerical model is developed by using commercial software ANSYS and LS-PREPOST as shown in Figure 7.9. The accuracy of the numerical model will be verified by using the developed model to simulate the laboratory tests reported above. The failure mode and residual speed of the projectile will be compared to verify the model. In the numerical model, basalt fibre is modelled with shell elements, OSB skin and EPS core are modelled with solid elements. Based on mesh convergence test in previous study (16), 5*5mm and 5*5*5mm mesh size are used for shell elements and solid elements in the dense area as shown in Figure 7.9. 25*5mm and 25*25mm mesh size are applied to the rest of the shell elements, and the corresponding solid elements are 25*5*5mm and 25*25*25mm. Owing to the unsymmetrical behaviour observed in the test due to slight eccentric and tilted impacting as discussed above, the model of full panel is built in the simulation to better capture the panel behaviours.

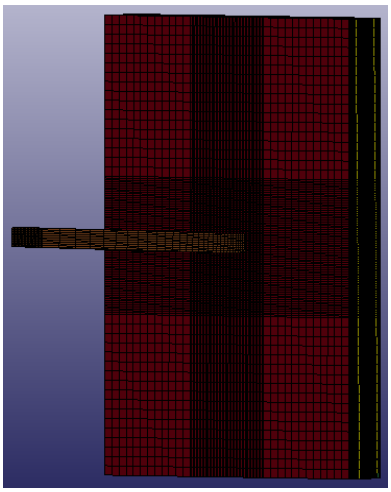

*Figure 7.9 Numerical model*

#### 7.3.1.1 Element types

In this study, the timber projectile is modelled by eight-node solid elements. The basalt fibre cloth is modelled by Belytschko-Tsay shell elements with two integration points for modelling the biaxial fabric. The OSB skin and EPS foam are modelled by using solid element with constant stress single integration node, which are used to overcome the negative volume during the simulation.

#### 7.3.1.2 Material models

The material models of OSB, EPS and timber projectile are applied according to the previous chapter. The material models *MAT 20, *MAT 54, *MAT 163 and *MAT 143 are selected to simulate the timber projectile, basalt fibre cloth, EPS foam and OSB skin, respectively.

The basalt fibre cloth is modelled by using material model *MAT 54 ENHANCED COMPOSITE DAMAGE, which is based on the Chang-Chang failure criteria although no basalt fibre failure was observed in the test.

When $\sigma_{aa} \geq 0$, the material would experience fibre rupture failure in tension fibre mode if

$$\sigma_f^2 = \left( \frac{\sigma_{aa}}{X_t} \right)^2 - 1 \geq 0 \tag{7.1}$$

When $\sigma_{aa} < 0$, the material would experience bucking and kinking in compression fibre mode if

$$\sigma_c^2 = \left( \frac{\sigma_{aa}}{X_t} \right)^2 - 1 \geq 0 \tag{7.2}$$

However, when $\sigma_{bb} \geq 0$ during the matrix model, tensile matrix mode failure like cracking under transverse tension and shearing would happen if

$$\sigma_m^2 = \left(\frac{\sigma_{bb}}{Y_t}\right)^2 + \left(\frac{\sigma_{ab}}{S_c}\right)^2 - 1 \geq 0 \tag{7.3}$$

When $\sigma_{aa} < 0$ in compressive matric mode, matrix cracking and shearing would happen if

$$\sigma_d^2 = \left(\frac{\sigma_{bb}}{2S_c}\right)^2 + \left[\left(\frac{Y_c}{2S_c}\right)^2 - 1\right]\frac{\sigma_{bb}}{Y_c} + \left(\frac{\sigma_{ab}}{S_c}\right)^2 - 1 \geq 0 \tag{7.4}$$

where $X_t$ stands for longitudinal compressive strength; $Y_c$ and $Y_t$ stand for transverse compressive strength (b-axis) and transverse tensile strength (b-axis), respectively; $S_c$ stands for shear strength;. Other parameters in the failure criteria can be defined by the maximum strains in tension and compression (175). The detailed parameters of basalt fibre are given in Table 7.2. As no dynamic material properties of basalt fibre are available, the strain rate effect on basalt fibre material properties is not considered.

*Table 7.2 Material parameters of Basalt fibre*

| Basalt Fibre (*MAT 54 ENHANCED COMPOSITE DAMAGE) | |
|---|---|
| Mass density (kg/m$^3$) | 2750 |
| Young's modulus (Pa) | 8.90E+10 |
| Poisson's ratio | 0.26 |
| Shear modulus (Pa) | 2.17E+10 |
| Longitudinal tensile strength (Pa) | 4.80E+09 |
| Longitudinal compressive strength (Pa) | 2.70E+07 |
| Effective failure strain | 0.24 |
| Maximum strain for fibre tension | 0.24 |
| Maximum strain for fibre compression | -0.135 |

### 7.3.1.3 Boundary conditions

Boundary condition affects the accuracy of simulation results. In the tests, the panel specimen was clamped with G-clamps around the four sides of each panel. In the numerical model, pinned boundary condition is applied at the clamped location of the panel to simulate the testing conditions by using the keyword *BOUNDARY SPC SET.

### 7.3.1.4 Contact keyword

In the numerical model, the contact between the projectile and the specimen is defined by using *CONTACT ERODING SURFACE TO SURFACE with

segment based contact option (i.e. SOFT=2). To model the contact between the skins and the core, *CONTACT ERODING SINGLE SURFACE is used and *CONTACT INTERIOR is utilized to avoid the negative volume within the EPS core. According to the study in previous chapter, the bonding between basalt fibre cloth and OSB/EPS is defined by using *CONTACT TIEBREAK SURFACE TO SURFACE ONLY.

### 7.3.2 Comparisons between experimental and numerical simulation results

To ensure the accuracy of the simulation, three tested panels have been selected to verify the numerical model. They are specimen A without strengthening as a reference for comparison, specimen D with basalt fibre layer applied to the front surface of the panel, and specimen E with the fibre cloth on the back surface of the panel. It should be noted that specimen B and specimen C with the fibre cloth as an additional interlayer is not considered here because it is not a realistic strengthening option.

The numerical results are compared with testing results including damage modes and residual velocity of the debris after impact.

#### 7.3.2.1 Specimen A

The specimen A subjected to 18 m/s impact is selected to calibrate the numerical model. Figure 7.10 (R) shows the numerical prediction of the failure mode of specimen A after the impact of 18 m/s. As shown the projectile penetrated through the panel and stayed in it. The simulated damage mode replicates the test result shown in Figure 7.10. The tests with impact velocities of 15 m/s and 20 m/s are also simulated to verify the numerical model. Numerical simulations also give good predictions of the failure mode and projectile residual velocity. As given in Table 7.3, the differences of the residual velocities for impact velocities of 15 m/s and 20 m/s are 8.2% and 1.5%, respectively, by comparing the testing results with the numerical results. It can be concluded that the numerical model can provide accurate predictions of the panel without strengthening subjected to projectile impact.

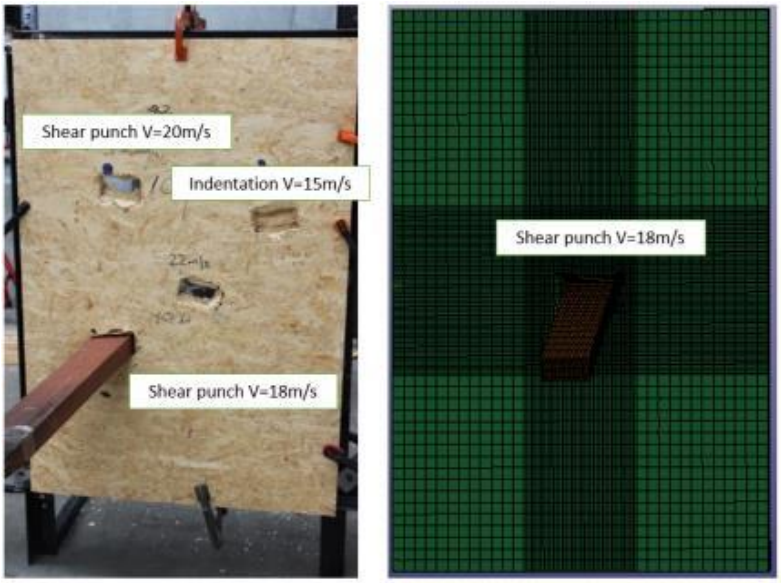


*Figure 7.10 Comparisons of damage mode of specimen A (Front view) (L) Test; (R) Numerical*

*Table 7.3 Data comparisons between laboratory test and numerical simulation (A)*

| Specimen | Test $V_I$ | Numerical $V_I$ | Test $V_R$ | Numerical $V_R$ | Error |
|---|---|---|---|---|---|
| A | 18m/s | 18m/s | 0m/s | 0m/s | 0% |
| A | 15m/s | 15m/s | -3.9m/s | -3.58m/s | 8.2% |
| A | 20m/s | 20m/s | 7.4m/s | 7.29m/s | 1.5% |
| D | 27.7m/s | 27.7m/s | -6.8m/s | -6.84m/s | 0.5% |
| E | 32m/s | 32m/s | 0m/s | 0m/s | 0% |

N.B "-" means rebound velocity, "$V_I$" means impact velocity, "$V_R$" means residual velocity

### 7.3.2.2 Specimen D

As shown in Figure 7.11 (L), the specimen D subjected to the projectile impact at 27.7 m/s experienced indentation on the front OSB skin and no crack was found on the back OSB skin. The basalt fibre cloth experienced partial debonding at the bottom side of specimen. By applying the same testing condition, i.e., the actual impacted location and the tilted impact angle of the projectile, the damage mode is well captured by the numerical predication as shown in Figure 7.11 (R). The projectile was rejected by the specimen D and rebounded at a velocity of -6.8 m/s in the test. Numerical simulation gives good prediction of the residual velocity, which is -6.84 m/s, with an error of 0.5%.

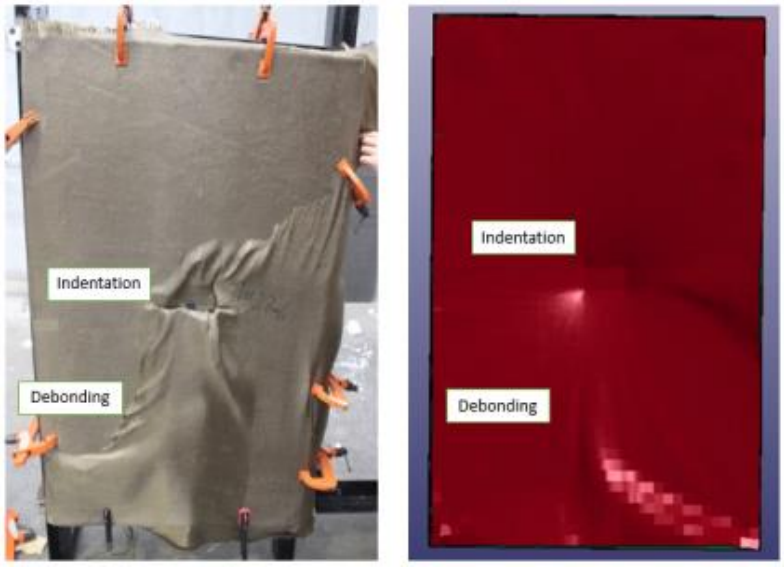


*Figure 7.11 Comparison of damage mode of specimen D (Front view) (L) Test; (R) Numerical*

#### 7.3.2.3 Specimen E

Figure 7.12 (L) shows the damage mode of specimen E after impacted by the projectile at 32m/s in the testing. The projectile penetrated and stayed on the specimen E in the test. The basalt fibre cloth at the back stopped the projectile and was partially torn around the boundary. As shown in Figure 7.12 (R), the damage mode in the numerical simulation is comparable to that obtained from the test. By comparing the damage modes from numerical results and testing results, it can be concluded that the numerical model gives reasonable predictions of the panel responses to the projectile impact.

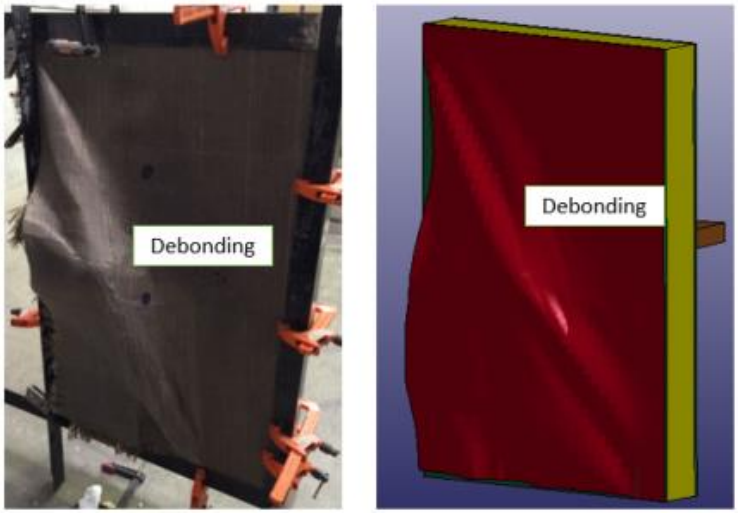


*Figure 7.12 Comparison of damage mode of specimen E (Back view) (L) Test; (R) Numerical*

## 7.4 Summary

In this chapter, both laboratory tests and numerical simulations have been conducted to investigate the effectiveness of using basalt fibre cloth to

strengthen SIPs with OSB skins to increase their capacity to resist windborne debris impact. A total of five SIP specimens without and with three strengthening schemes were tested. It was observed that under the impact of a 4 kg timber projectile at different velocities, the specimens could suffer shear punching, indentation, fibre cloth debonding, rupturing of the back OSB skin, and boundary failure. The application of basalt fibre cloth was found effective in enhancing the impact resistance capacity of the SIP. The placement of the basalt fibre cloth at the back OSB skin was found to be the most appropriate method among the three schemes investigated in this study. In addition, numerical models have been developed to simulate the response of SIPs without and with basalt fibre cloth strengthening subjected to projectile impact. The accuracy of the numerical model has been verified with the test data. The validated numerical model can be utilized to conduct further parametric simulations to better understand the performance of basalt fibre cloth strengthened SIPs with OSB skins, so that the optimal strengthening techniques by using basalt fibre cloth for effective engineering adaptation can be determined.

***The [Meng Q, Chen W, Hao H. Vulnerability Analyses of Structural Insulated Panels with OSB Skins Strengthened by Basalt Fiber Cloth Subjected to Windborne Debris Impact. International Journal of Structural Stability and Dynamics. 2018 Jun;18(06):1850088.] is unable to be reproduced here due to copyright restrictions.***

***The [Vulnerability Analyses of Structural Insulated Panels with OSB Skins Strengthened by Basalt Fiber Cloth Subjected to Windborne Debris Impact] can instead be accessed via [https://doi.org/10.1142/S0219455418500888]***

# Chapter 9 Conclusion and recommendation

## 9.1 Main findings

This study is aimed to investigate the capacities of OSB Skin Structural Insulated Panels in resisting windborne debris impacts, and the effectiveness of various strengthening techniques in improving the impact resistance. In this study, four materials (i.e., glass fibre laminate, steel wire mesh, basalt fibre mesh and basalt fibre cloth) are used to strengthen structural insulated panels with OSB skin against windborne debris impact. Dynamic response and damage mode of the unstrengthened and strengthened SIPs are studied. To understand the dynamic behaviours of OSB skin and glass fibre laminate material, dynamic tensile tests are carried out. Parametric studies have also been undertaken to investigate the influence of strengthening methods on impact resistance capacity. The major contributions and findings in this thesis are summarised below.

Chapter 3 and Chapter 4 present the strain rate effect on the material properties of oriented strand board (OSB) and glass fibre laminate material. The dynamic tensile strength of OSB material at the strain rate of 28.7 $s^{-1}$ is about two times of its quasi-static strength. For the glass fibre laminate, when the strain rate reaches 104.6 $s^{-1}$, the failure strain is 4.24%, with an increment of 89.3 % comparing with the failure strain at quasi-static status. The tensile strength increases from approx. 340 MPa to approx. 430 MPa when the strain rate increases from 2.8 $s^{-1}$ to 105 $s^{-1}$. The tensile strength vs strain rate curves are plotted for both OSB and glass fibre laminate material, and the empirical formulae of dynamic increase factors of strength and failure strain are also derived.

Chapter 5, Chapter 6 and Chapter 7 present the performances of OSB skin SIP strengthened by glass fibre laminate, steel wire mesh, basalt fibre mesh and basalt fibre cloth, respectively. The enhancements of impact resistance capacity due to different strengthening measures are found from the experimental and numerical investigations. The basalt fibre cloth is found as the most effective material to strengthen the OSB skin SIP. As observed from testing, the back strengthening method has better performance because the fibre cloth functions as catcher to protect the resident inside the house. The steel wire mesh and basalt mesh are considered as lightweight and cheap material to strengthen the OSB skin SIP with limited improvement.

Chapter 8 presents the vulnerability study of basalt fibre fabric strengthened OSB SIP. The numerical model calibrated in Chapter 7 is used for generating vulnerability curves by considering different bonding strength and fabric thickness. The empirical formulae derived from vulnerability curves can be used to predict the thresholds of projectile mass and velocity of penetrating basalt fibre cloth strengthened SIP.

## 9.2 Recommendations for future work

Based on the experimental and numerical work of SIP strengthening, further investigations could be explored as follows.

As observed in Chapters 5, 6 and 7, the impact resistance capacities of structural panels increased by strengthening and the debonding occurred between the strengthening layer and the OSB skins. To improve the impact-resistant performance of strengthened panel, better bonding between the strengthening layer and OSB skins is needed in future study. Boundary failure was observed in the testing. The development of boundary conditions is also needed in future study. Beside the windborne debris impact threat, the strengthened SIP subjected to other threats including accidental gas explosion is worth studying. In addition, design guidelines based on new design and strengthening techniques are desired for the engineering practice of SIP strengthening in cyclonic area.

# References


1. Allen G. Hurricane Andrew's Legacy: 'Like A Bomb' In Florida. NPR; 2012.
2. Ed R. Preliminary Report (updated 2 March 1993) Hurricane Andrew, 16-28 August 1992: National Hurricane Center; 1993.
3. Kareem A. Structural performance and wind speed-damage correlation in Hurricane Alicia. Journal of Structural Engineering. 1985;111(12):2596-610.
4. Hook DD, Buford MA, Williams TM. Impact of Hurricane Hugo on the South Carolina coastal plain forest. Journal of Coastal Research. 1991:291-300.
5. Mehta KC. Wind induced damage observations and their implications for design practice. Eng Struct. 1984;6(4):242-7.
6. Mehta KC, Cheshire RH, McDonald JR. Wind resistance categorization of buildings for insurance. J Wind Eng Ind Aerod. 1992;44(1–3):2617-28.
7. Pan K, Montpellier P, Zadeh M. Engineering observations of 3 May 1999 Oklahoma tornado damage. Weather Forecast. 2002;17(3):599-610.
8. Lee BE, Wills J. Vulnerability of fully glazed high-rise buildings in tropical cyclones. J Archit Eng. 2002;8(2):42.
9. Porter WH. Structural insulated panel. Google Patents; 2001.
10. Chen W, Hao H, Du H. Failure analysis of corrugated panel subjected to windborne debris impacts. Eng Failure Anal. 2014;44:229-49.
11. Chen W, Hao H, Irawan P, Chen S, Meng Q. Experimental investigations of fabric material against projectile impacts. Construction and Building Materials. 2016;104:142-53.
12. Chen W, Hao H, Li J, editors. Fragility curves for corrugated structural panel subjected to windborne debris impact. International Conference on Performance-based and Life-cycle Structural Engineering; 2015: School of Civil Engineering, The University of Queensland.
13. Chen W, Hao H, Meng Q. Experimental study of steel wire mesh reinforced structural insulated panels against windborne debris impact. 2017.
14. Chen WS, Hao H, Du H, editors. Numerical study of corrugated metal panels subjected to windborne debris impacts. Key Engineering Materials; 2015: Trans Tech Publ.
15. Chen W, Hao H. A study of corrolink structural insulated panel (SIP) to windborne debris impacts. Key Engineering Materials. 2014;626.
16. Chen W, Hao H. Experimental and numerical study of composite lightweight structural insulated panel with expanded polystyrene core against windborne debris impacts. Mater Design. 2014;60:409-23.
17. Chen W, Hao H. Experimental investigations and numerical simulations of multi-arch double-layered panels under uniform impulsive loadings. International Journal of Impact Engineering. 2014;63:140-57.
18. Chen W, Hao H. Performance of structural insulated panels with rigid skins subjected to windborne debris impacts–Experimental investigations. Construction and Building Materials. 2015;77:241-52.
19. Committee JT. AS/NZS 1170.2: 2011 Structural design actions-Part 2: Wind actions. Australian/New Zealand Standard (AS/NZS), Joint Technical Committee BD-006, Australia/New Zealand. 2011.
20. Frank NL, Husain S. The deadliest tropical cyclone in history. Bulletin of the American Meteorological Society. 1971;52(6):438-45.
21. Adminstration NAaS. Why and How NASA Investigates Hurricanes.
22. Center NH. Hurricane Andrew 1992.

23. Sparks PR, Schiff S, Reinhold T. Wind damage to envelopes of houses and consequent insurance losses. Journal of Wind Engineering and Industrial Aerodynamics. 1994;53(1):145-55.
24. FEMA. Hurricane Andrew in Florida Observations. Recommendations, and Technical Guidance, FEMA, Federal Insurance Administration.
25. Perry D. Hurricane Andrew-Preliminary observations of WERC Post-disaster Team. College Station, TX: Wind Engineering Research Council, September. 1992.
26. Lessons Learned from Failures of the Building Envelope in Windstorms. Journal of Architectural Engineering. 2005;11(1):10-3.
27. Minor JE, Mehta KC, McDonald JR. Failure of structures due to extreme winds. Journal of the Structural Division. 1972;98(11):2455-71.
28. Minor JE. Windborne debris and the building envelope. Journal of Wind Engineering and Industrial Aerodynamics. 1994;53(1–2):207-27.
29. Wills JAB, Lee BE, Wyatt TA. A model of wind-borne debris damage. Journal of Wind Engineering and Industrial Aerodynamics. 2002;90(4–5):555-65.
30. Lin N, Holmes JD, Letchford CW. Trajectories of wind-borne debris in horizontal winds and applications to impact testing. J Struct Eng. 2007;133(2):274-82.
31. McDonald JR. Impact resistance of common building materials to tornado missiles. Journal of Wind Engineering and Industrial Aerodynamics. 1990;36:717-24.
32. Børvik T, Langseth M, Hopperstad O, Malo K. Ballistic penetration of steel plates. International journal of impact engineering. 1999;22(9-10):855-86.
33. Børvik T, Langseth M, Hopperstad O, Malo K. Perforation of 12 mm thick steel plates by 20 mm diameter projectiles with flat, hemispherical and conical noses: Part I: Experimental study. International Journal of Impact Engineering. 2002;27(1):19-35.
34. Børvik T, Hopperstad O, Berstad T, Langseth M. Perforation of 12 mm thick steel plates by 20 mm diameter projectiles with flat, hemispherical and conical noses: part II: numerical simulations. International journal of impact engineering. 2002;27(1):37-64.
35. Corbett G, Reid S, Johnson W. Impact loading of plates and shells by free-flying projectiles: a review. International Journal of Impact Engineering. 1996;18(2):141-230.
36. Virostek S, Dual J, Goldsmith W. Direct force measurement in normal and oblique impact of plates by projectiles. International Journal of Impact Engineering. 1987;6(4):247-69.
37. Goldsmith W, Finnegan SA. Normal and oblique impact of cylindro-conical and cylindrical projectiles on metallic plates. International Journal of Impact Engineering. 1986;4(2):83-105.
38. Awerbuch J, Bodner S. An investigation of oblique perforation of metallic plates by projectiles. Experimental Mechanics. 1977;17(4):147-53.
39. Woodward R, Baldwin N. Oblique perforation of targets by small armour-piercing projectiles. Journal of Mechanical Engineering Science. 1979;21(2):85-91.
40. Fatt MSH, Park KS. Modeling low-velocity impact damage of composite sandwich panels. Journal of Sandwich Structures & Materials. 2001;3(2):130-68.
41. Marom I, Bodner S. Projectile perforation of multi-layered beams. International Journal of Mechanical Sciences. 1979;21(8):489-504.
42. Corran R, Shadbolt P, Ruiz C. Impact loading of plates—an experimental investigation. International Journal of Impact Engineering. 1983;1(1):3-22.
43. Radin J, Goldsmith W. Normal projectile penetration and perforation of layered targets. International Journal of Impact Engineering. 1988;7(2):229-59.

44. Hetherington J, Rajagopalan B. An investigation into the energy absorbed during ballistic perforation of composite armours. International Journal of Impact Engineering. 1991;11(1):33-40.
45. AS/NZS. Structural design actions. Part2: Wind actions. Sydney, NSW, Australia: Standard Australia & Standards New Zealand; 2011.
46. FEMA. Taking Shelter From the Storm: Building a Safe Room For Your Home or Small Business (Third Edition). USA: Federal Emergency Management Agency; 2008.
47. SBC. Standard for Determining Impact Resistance from Windborne Debris. Birmingham, Alabama, USA: Southern Building Code Congress International; 1999.
48. FBC. Florida Building Code 2010, Building. USA: International Code Council, Inc.; 2011.
49. Scheer DL. Large wind missile impact performance of public and commercial building assemblies: Florida State University; 2005.
50. Ginger J, Henderson D, Edwards M, Holmes J, editors. Housing damage in windstorms and mitigation for Australia2010.
51. Frye U, Ginger J, Mullins P. Response of cladding to windborne debris impact. The Seventh Asia-Pacific Conference on Wind Engineering; November 8-12, 2009; Taipei, Taiwan: Chinese Taiwan Association for Wind Engineering; 2009.
52. Braden CP. Large wind missile impact performance of public and commercial building assemblies: University of Florida; 2004.
53. Scheer DL. Large wind missile impact performance of public and commercial building assemblies. 2005.
54. Fernandez G, Masters FJ, Gurley KR. Performance of hurricane shutters under impact by roof tiles. Engineering Structures. 2010;32(10):3384-93.
55. Wensu Chen HH. Experimental investigations and numerical simulations of multi-arch double-layered panels under uniform impulsive loadings. International Journal of Impact Engineering. 2014;63:140-57.
56. Zhang X, Hao H, Ma G. Laboratory test and numerical simulation of laminated glass window vulnerability to debris impact. Int J Impact Eng. 2013;55:49-62.
57. Zhao H, Elnasri I, Girard Y. Perforation of aluminium foam core sandwich panels under impact loading—An experimental study. International journal of impact engineering. 2007;34(7):1246-57.
58. Børvik T, Langseth M, Hopperstad O, Malo K. Perforation of 12mm thick steel plates by 20mm diameter projectiles with flat, hemispherical and conical noses: part I: experimental study. Int J Impact Eng. 2002;27(1):19-35.
59. Meng Q, Hao H, Chen W. Numerical study of basalt fibre cloth strengthened Structural Insulated Panel under windborne debris impact. Applied Mechanics & Materials. 2016;846.
60. Wang J, Waas AM, Wang H. Experimental and numerical study on the low-velocity impact behavior of foam-core sandwich panels. Compos Struct. 2013;96(1):298-311.
61. Found MS, Howard IC, Paran AP. Size effects in thin CFRP panels subjected to impact. Compos Struct. 1997;38(1–4):599-607.
62. Found MS, Howard IC, Paran AP. Impact behaviour of stiffened CFRP sections. Compos Struct. 1997;39(3–4):229-35.
63. Mines RAW, Worrall CM, Gibson AG. Low velocity perforation behaviour of polymer composite sandwich panels. Int J Impact Eng. 1998;21(10):855-79.

64. Mutalib A. Damage assessment and prediction of FRP strengthened RC structures subjected to blast and impact loads: the University of Western Australia; 2011.
65. Herbin AH. Fragility analysis of building envelope components subject to windborne debris impact hazard: Faculty of the Louisiana State University and Agricultural and Mechanical College in partial fulfillment of the requirements for the degree of Master of Science in Civil Engineering in The Department of Civil and Environmental Engineering by Alexander H. Herbin BSCE, Louisiana State University; 2011.
66. Herbin AH, Barbato M. Fragility curves for building envelope components subject to windborne debris impact. J Wind Eng Ind Aerod. 2012;107-108:285-98.
67. Croop B, Lobo H. Selecting material models for the simulation of foams in LS-DYNA. Proceedings of 7th European LS-DYNA Conference; Salzburg2009.
68. Remennikov AM, Kong SY. Numerical simulation and validation of impact response of axially-restrained steel–concrete–steel sandwich panels. Compos Struct. 2012;94(12):3546-55.
69. Meo M, Vignjevic R, Marengo G. The response of honeycomb sandwich panels under low-velocity impact loading. International Journal of Mechanical Sciences. 2005;47(9):1301-25.
70. Meo M, Morris AJ, Vignjevic R, Marengo G. Numerical simulations of low-velocity impact on an aircraft sandwich panel. Compos Struct. 2003;62(3–4):353-60.
71. Guo J, Shi G, Wang Y, Lu C. Efficient modeling of panel-like structures in perforation simulations. Computers & Structures. 2003;81(1):1-8.
72. Zhou DW, Stronge WJ. Low velocity impact denting of HSSA lightweight sandwich panel. IJMS. 2006;48(10):1031-45.
73. Li J, Zhang YX. Evolution and calibration of a numerical model for modelling of hybrid-fibre ECC panels under high-velocity impact. Composite Structures. 2011;93(11):2714-22.
74. Triantafillou TC. Shear strengthening of reinforced concrete beams using epoxy-bonded FRP composites. ACI structural journal. 1998;95(2).
75. Muszynski LC, Purcell MR. Composite reinforcement to strengthen existing concrete structures against air blast. Journal of Composites for Construction. 2003;7(2):93-7.
76. Mutalib AA, Hao H. Numerical analysis of FRP-composite-strengthened RC panels with anchorages against blast loads. Journal of Performance of Constructed Facilities. 2010;25(5):360-72.
77. Mutalib AA, Hao H. Development of PI diagrams for FRP strengthened RC columns. International Journal of Impact Engineering. 2011;38(5):290-304.
78. Triantafillou TC. Strengthening of masonry structures using epoxy-bonded FRP laminates. Journal of composites for construction. 1998;2(2):96-104.
79. Jing M, Raongjant W, editors. Using GFRP to develop the mechanical performance of structural insulated panels. Advanced Materials Research; 2013: Trans Tech Publ.
80. Mousa MA, Uddin N. Experimental and analytical study of carbon fiber-reinforced polymer (FRP)/autoclaved aerated concrete (AAC) sandwich panels. Engineering Structures. 2009;31(10):2337-44.
81. Mohotti D, Ngo T, Mendis P, Raman SN. Polyurea coated composite aluminium plates subjected to high velocity projectile impact. Mater Design. 2013;52:1-16.
82. Wu G WZ, Lu Z, Wei h, Hu X. The Outstanding Advantages of Applying Basalt Fiber Polymer (BFRP) in Structure Post-earthquake Strengthening and Rehabilitation.

83. Lopresto V, Leone C, De Iorio I. Mechanical characterisation of basalt fibre reinforced plastic. Composites Part B: Engineering. 2011;42(4):717-23.
84. Nie J, Wang H, Zhang T, Cai Q, Qin K. Experimental study on flexural behavior of RC beams strengthened with stainless steel wire mesh and permeability polymer mortar [J]. Journal of Building Structures. 2005;2:002.
85. Huang H, Liu B-Q, Xing G-H, Liu Y-S, Li T-Q. Experiment on RC T-type beam bridge strengthened with high strength stainless steel wire mesh and permeability polymer mortar. Zhongguo Gonglu Xuebao(China Journal of Highway and Transport). 2007;20(4):83-90.
86. Morton E, Thompson A, Villaescusa E, Roth A, editors. Testing and analysis of steel wire mesh for mining applications of rock surface support. 11th ISRM Congress; 2007: International Society for Rock Mechanics.
87. Ibrahim HM. Experimental investigation of ultimate capacity of wired mesh-reinforced cementitious slabs. Constr Build Mater. 2011;25(1):251-9.
88. Kumar V, Patel P. Strengthening of axially loaded circular concrete columns using stainless steel wire mesh (SSWM)–Experimental investigations. Construction and Building Materials. 2016;124:186-98.
89. Gao C, Huang L, Yan L, Ma G, Xu L. Compressive behavior of CFFT with inner steel wire mesh. Composite Structures. 2015;133:322-30.
90. Li J, Wu C, Hao H, Su Y. Experimental and numerical study on steel wire mesh reinforced concrete slab under contact explosion. Materials & Design. 2017;116:77-91.
91. Shaheen YB, Eltaly BA, Abdul-Fataha SG. Structural performance of ferrocement beams reinforced with composite materials. Structural Engineering and Mechanics. 2014;50(6):817-34.
92. Manalo A. Structural behaviour of a prefabricated composite wall system made from rigid polyurethane foam and Magnesium Oxide board. Constr Build Mater. 2013;41:642-53.
93. Alldritt K. Designing a strand orientation pattern for improved shear properties of oriented strand board. Journal of Materials in Civil Engineering. 2013;26(7).
94. Shmulsky R, Jones PD. Forest products and wood science: John Wiley & Sons; 2011.
95. Lindquist CR, Clarke JT, Chin PP, MacDonald MJ, Walsh JP. Flat oriented strand board-fiberboard composite structure and method of making the same. Google Patents; 1995.
96. Mines R, Worrall C, Gibson A. Low velocity perforation behaviour of polymer composite sandwich panels. International Journal of Impact Engineering. 1998;21(10):855-79.
97. Meng Q, Hao H, Chen W. Experimental and numerical study of basalt fibre cloth strengthened structural insulated panel under windborne debris impact. Journal of Reinforced Plastics and Composites. 2016;35(17):1302-17.
98. Meng Q, Hao H, Chen W. Laboratory test and numerical study of structural insulated panel strengthened with glass fibre laminate against windborne debris impact. Constr Build Mater. 2016;114:434-46.
99. Kopowski S, Gebbeken N. Wood Sandwich Constructions Subjected to Small Caliber Impact. International Journal of Protective Structures. 2013;4(2):127-41.
100. Atas C, Sevim C. On the impact response of sandwich composites with cores of balsa wood and PVC foam. Composite Structures. 2010;93(1):40-8.
101. Thomas W. Poisson's ratios of an oriented strand board. Wood science and technology. 2003;37(3-4):259-68.

102. Uang C-M, Gatto K. Effects of finish materials and dynamic loading on the cyclic response of woodframe shearwalls. Journal of Structural Engineering. 2003;129(10):1394-402.
103. Lacroix D, Doudak G. Behaviour of Light-Frame Wood Stud Walls Under High Strain Rates. 3rd Specialty Conference on Material Engineering & Applied Mechanics. 2013.
104. Cassidy ED, Davids WG, Dagher HJ, Gardner DJ. Performance of wood shear walls sheathed with FRP-reinforced OSB panels. Journal of Structural Engineering. 2006;132(1):153-63.
105. Sretenovic A, Müller U, Gindl W. Comparison of the in-plane shear strength of OSB and plywood using five point bending and EN 789 steel plate test methods. Holz als Roh-und Werkstoff. 2005;63(2):160-4.
106. Fan M, Enjily V. Structural properties of oriented wood strand composite: effect of strand orientation and modeling prediction. Journal of engineering mechanics. 2009;135(11):1323-30.
107. Böhm M, Šedivka P, Bomba J, Reisner J. Strength Characteristics of OSB in Bending–Difference between Upper and Lower Panel Faces. Drvna industrija. 2011;62(2):123-7.
108. Durham J, Lam F, Prion HG. Seismic resistance of wood shear walls with large OSB panels. Journal of Structural Engineering. 2001;127(12):1460-6.
109. Feraboli P. Notched response of OSB wood composites. Composites Part A: Applied Science and Manufacturing. 2008;39(9):1355-61.
110. Tedesco J, Ross C, Kuennen S. Strain rate effects on the compressive strength of shock-mitigating foams. Journal of sound and vibration. 1993;165(2):376-84.
111. Naito K. Tensile Properties of Polyimide Composites Incorporating Carbon Nanotubes-Grafted and Polyimide-Coated Carbon Fibers. Journal of Materials Engineering and Performance. 2014;23(9):3245-56.
112. Naito K. Effect of Strain Rate on Tensile Properties of Carbon Fiber Epoxy-Impregnated Bundle Composite. Journal of materials engineering and performance. 2014;23(3):708-14.
113. Al-Zubaidy H, Zhao X-L, Al-Mahaidi R. Mechanical characterisation of the dynamic tensile properties of CFRP sheet and adhesive at medium strain rates. Compos Struct. 2013;96:153-64.
114. Chen W, Hao H, Hughes D, Shi Y, Cui J, Li Z-X. Static and dynamic mechanical properties of expanded polystyrene. Mater Design. 2015;69:170-80.
115. Zhang X, Hao H, Shi Y, Cui J, Zhang X. Static and dynamic material properties of CFRP/epoxy laminates. Constr Build Mater. 2016;114:638-49.
116. Zhan T, Wang Z, Ning J. Failure behaviors of reinforced concrete beams subjected to high impact loading. Engineering Failure Analysis. 2015;56:233-43.
117. Albdiry M, Ku H, Yousif B. Impact fracture behaviour of silane-treated halloysite nanotubes-reinforced unsaturated polyester. Engineering Failure Analysis. 2013;35:718-25.
118. Lichtenfeld JA, Van Tyne CJ, Mataya MC. Effect of strain rate on stress-strain behavior of alloy 309 and 304L austenitic stainless steel. Metallurgical and Materials Transactions A. 2006;37(1):147-61.
119. Zhao GP, Wang ZH, Zhang JX, Huang QP, editors. Modeling and Testing Strain Rate-Dependent Tensile Strength of Carbon/Epoxy Composites. Key Engineering Materials; 2007: Trans Tech Publ.
120. Chen W, Lu F, Cheng M. Tension and compression tests of two polymers under quasi-static and dynamic loading. Polym Test. 2002;21(2):113-21.

121. Gary G, Bailly P. Behaviour of quasi-brittle material at high strain rate. Experiment and modelling. European Journal of Mechanics-A/Solids. 1998;17(3):403-20.
122. Zhou J, Chen X. Stress-strain behavior and statistical continuous damage model of cement mortar under high strain rates. Journal of Materials in Civil Engineering. 2012;25(1):120-30.
123. Zhu D, Mobasher B, Rajan SD. Dynamic tensile testing of Kevlar 49 fabrics. Journal of Materials in Civil Engineering. 2010;23(3):230-9.
124. Xiao X. Dynamic tensile testing of plastic materials. Polymer Testing. 2008;27(2):164-78.
125. EGGER. DBWIS054 - E Safety Data Sheet EGGER OSB. 2014.
126. Chen W, Meng Q, Hao H, Cui J, Shi Y. Quasi-static and dynamic tensile properties of fiberglass/epoxy laminate sheet. Constr Build Mater. 2017;143:247-58.
127. Liu L, Dai L, Bai Y, Wei B. Initiation and propagation of shear bands in Zr-based bulk metallic glass under quasi-static and dynamic shear loadings. Journal of non-crystalline solids. 2005;351(40):3259-70.
128. Hao Y, Hao H. Dynamic compressive behaviour of spiral steel fibre reinforced concrete in split Hopkinson pressure bar tests. Constr Build Mater. 2013;48:521-32.
129. Zhai C, Chen L, Fang Q, Chen W, Jiang X. Experimental study of strain rate effects on normal weight concrete after exposure to elevated temperature. Mater Struct. 2017;50(1):40.
130. Barre S, Chotard T, Benzeggagh M. Comparative study of strain rate effects on mechanical properties of glass fibre-reinforced thermoset matrix composite. Composites Part A: Applied Science and Manufacturing. 1996;27(12):1169-81.
131. Reis JML, Coelho JLV, Monteiro AH, da Costa Mattos HS. Tensile behavior of glass/epoxy laminates at varying strain rates and temperatures. Composites Part B: Engineering. 2012;43(4):2041-6.
132. Naderi M, Khonsari M. Thermodynamic analysis of fatigue failure in a composite laminate. Mech Mater. 2012;46:113-22.
133. Liakat M, Khonsari M. Analysis and life prediction of a composite laminate under cyclic loading. Composites Part B: Engineering. 2016;84:98-108.
134. Whisler D, Kim H. Effect of impactor radius on low-velocity impact damage of glass/epoxy composites. JCoMa. 2012;46(25):3137-49.
135. Herranena H, Allikasb G, Eermea M, Venea K, Ottoa T, Gregorb A, et al. Visualization of strain distribution around the edges of a rectangular foreign object inside the woven carbon fibre specimen. Estonian Journal of Engineering. 2012;18(3):279-87.
136. Ochola R, Marcus K, Nurick G, Franz T. Mechanical behaviour of glass and carbon fibre reinforced composites at varying strain rates. Compos Struct. 2004;63(3):455-67.
137. Davies R, Magee C. The effect of strain-rate upon the tensile deformation of materials. J Eng Mater Technol. 1975;97(2):151-5.
138. Staab GH, Gilat A. High strain rate response of angle-ply glass/epoxy laminates. JCoMa. 1995;29(10):1308-20.
139. Welsh L, Harding J. Effect of strain rate on the tensile failure of woven reinforced polyester resin composites. Le Journal de Physique Colloques. 1985;46(C5):C5-405-C5-14.
140. Schoßig M, Bierögel C, Grellmann W, Mecklenburg T. Mechanical behavior of glass-fiber reinforced thermoplastic materials under high strain rates. Polym Test. 2008;27(7):893-900.

141. Harding J, Welsh LM. A tensile testing technique for fibre-reinforced composites at impact rates of strain. JMatS. 1983;18(6):1810-26.
142. Yao Y, Zhu D, Zhang H, Li G, Mobasher B. Tensile Behaviors of Basalt, Carbon, Glass, and Aramid Fabrics under Various Strain Rates. J Mater Civ Eng. 2016:04016081.
143. Daniel I, Liber T. Strain Rate Effects on Mechanical Properties of Fiber Composites. Part 3. DTIC Document; 1976.
144. Lifshitz JM. Impact strength of angle ply fiber reinforced materials. JCoMa. 1976;10(1):92-101.
145. Armenakas A, Sciammarella C. Response of glass-fiber-reinforced epoxy specimens to high rates of tensile loading. Exp Mech. 1973;13(10):433-40.
146. Hou J, Ruiz C. Measurement of the properties of woven CFRP T300/914 at different strain rates. Composites Sci Technol. 2000;60(15):2829-34.
147. Belingardi G, Vadori R. Low velocity impact tests of laminate glass-fiber-epoxy matrix composite material plates. International Journal of Impact Engineering. 2002;27(2):213-29.
148. Okoli OI, Smith GF. The effect of strain rate and fibre content on the Poisson's ratio of glass/epoxy composites. Compos Struct. 2000;48(1–3):157-61.
149. Landel RF, Nielsen LE. Mechanical properties of polymers and composites: CRC Press; 1993.
150. Wisnom M. Size effects in the testing of fibre-composite materials. Composites Sci Technol. 1999;59(13):1937-57.
151. Harding J. Effect of strain rate and specimen geometry on the compressive strength of woven glass-reinforced epoxy laminates. Compo. 1993;24(4):323-32.
152. Shokrieh MM, Omidi MJ. Tension behavior of unidirectional glass/epoxy composites under different strain rates. Compos Struct. 2009;88(4):595-601.
153. Ou Y, Zhu D. Tensile behavior of glass fiber reinforced composite at different strain rates and temperatures. Constr Build Mater. 2015;96:648-56.
154. ASTM. D638-03 Standard test method for tensile properties of plastics. ASTM International2003.
155. Sierakowski R. Strain rate effects in composites. Applied Mechanics Reviews. 1997;50(12):741-61.
156. Mohotti D, Ali M, Ngo T, Lu J, Mendis P. Strain rate dependent constitutive model for predicting the material behaviour of polyurea under high strain rate tensile loading. Mater Design. 2014;53:830-7.
157. Xu S, Ruan D, Beynon JH, Rong Y. Dynamic tensile behaviour of TWIP steel under intermediate strain rate loading. Materials Science and Engineering: A. 2013;573:132-40.
158. Xiao XR. Dynamic tensile testing of plastic materials. Polym Test. 2008;27(2):164-78.
159. Peterson BL, Pangborn RN, Pantano CG. Static and High Strain Rate Response of a Glass Fiber Reinforced Thermoplastic. JCoMa. 1991;25(7):887-906.
160. Loewenstein KL. The manufacturing technology of continuous glass fibers. 1973.
161. Kawata K, Hondo A, Hashimoto S, Takeda N, Chung H, editors. Dynamic behaviour analysis of composite materials. Proceeding of Japan-US Conference on Composite Materials; 1981: Japan Society for Composite Materials, Tokyo.
162. Sun Y, Yu Z, Wang Z, Liu X. Novel protective covering to enhance concrete resistance against projectile impact. Constr Build Mater. 2015;96:484-90.
163. Lu G, Yu T. Energy absorption of structures and materials: Elsevier; 2003.

164. Croop B, Lobo H, DatapointLabs N, editors. Selecting material models for the simulation of foams in LS-DYNA. Proceedings of the 7th European LS-DYNA conference, Dynamore Gmbh, Salzburg, Germany; 2009.
165. Chen W, Hao H, Hughes D, Shi Y, Cui J, Li Z. Static and dynamic mechanical properties of expanded polystyrene. Materials & Design. 2015;69:170-80.
166. Hao H, Chen W, Chen S, Meng Q, editors. Finite Element Analysis of Structural Insulated Panel with OSB Skins against Windborne Debris Impacts (Keynote paper). 1st Pan-American Congress on Computational Mechanics (PANACM); 2015.
167. Murray YD. Manual for LS-DYNA Wood Material Model 143. 2007.
168. LS-DYNA. Keyword User's Manual V971. 2006;Livermore(CA: LSTC).
169. Cruzado A, Leen S, Urchegui M, Gómez X. Finite element simulation of fretting wear and fatigue in thin steel wires. International Journal of Fatigue. 2013;55:7-21.
170. Chen L, Fang Q, Fan J, Zhang Y, Hao H, Liu J. Responses of Masonry Infill Walls Retrofitted with CFRP, Steel Wire Mesh and Laminated Bars to Blast Loadings. Adv Struct Eng. 2014;17(6):817-36.
171. Sim Jongsung PC, Moon Do Young. Characteristics of basalt fiber as a strengthening material for concrete structures. Composites Part B: Engineering. 2005;36(6–7):504-12.
172. Deák T, Czigány T. Chemical composition and mechanical properties of basalt and glass fibers: a comparison. Textile Research Journal. 2009;79(7):645-51.
173. Chen Wensu HH. Performance of structural insulated panels with rigid skins subjected to windborne debris impacts–Experimental investigations. Construction and Building Materials. 2015;77:241-52.
174. Chajes MJ, Thomson TA, Januszka TF, Finch WW. Flexural strengthening of concrete beams using externally bonded composite materials. Construction and Building Materials. 1994;8(3):191-201.
175. Osborne M. Single-Element Characterization of the LS-DYNA MAT54 Material Model: University of Washington; 2012.

# Appendix I

Statements of the Co-authors

To whom it may concern

I, Qingfei Meng, conducted literature review, experimental investigations and written manuscripts of the paper titled "**Failure behaviours of Oriented Strand Board (OSB) material under quasi-static and dynamic loads**" which was revised and edited by the second co-author and the third co-author. The second and third co-author also help in performing the experimental investigations and analysis of numerical results. The fourth fifth and sixth co-author provided help during the dynamic experimental investigations.

(.....)

I, as a Co-author, endorse that this level of contribution by the candidate indicated above is appropriate.

(Prof. Hong Hao) (.....)

(Dr. Wensu Chen) (.....)

(Prof. Yanchao Shi) (.....)

(Mr. Jian Cui) (.....)

(Mr. Xuejie Zhang) (.....)

To whom it may concern

I, Qingfei Meng, conducted dynamic experimental investigations and written partial of manuscripts of the paper titled "**Quasi-static and dynamic tensile properties of fiberglass/epoxy laminate sheet**" which was revised and edited by the First co-author and the third co-author. The first Co-author conducted the literature review, static experimental investigations and analysis the whole test result. The fourth co-author and fifth co-author provide help in the dynamic experimental investigation. The first and third co-author also help in performing the experimental investigations and analysis of numerical results.

(.....)

I, as a Co-author, endorse that this level of contribution by the candidate indicated above is appropriate.

(Prof. Hong Hao) (.....)

(Dr. Wensu Chen) (.....)

(Prof. Yanchao Shi) (.....)

(Mr. Jian Cui) (.....)

To whom it may concern

I, Qingfei Meng, conducted literature review, numerical investigation, analysis of numerical results, experimental investigations and written manuscripts of the paper titled below which was revised and edited by the second co-author and the third co-author. The co-authors also help in performing the experimental investigations and analysis of numerical results.

**Experimental and numerical study on the basalt fibre cloth strengthened SIP panels under windborne debris impact**

**Experimental and numerical study on the glass fibre laminate strengthened structural insulated panel against windborne debris impact**

**Experimental and numerical study on steel wire mesh and basalt fibre mesh strengthened structural insulated panel (SIP) against windborne debris impact**

**Vulnerability analyses of OSB skin structural insulated panel strengthened with basalt fibre cloth subjected to windborne debris impact**

(.....)

I, as a Co-author, endorse that this level of contribution by the candidate indicated above is appropriate.

(Prof. Hong Hao) (.....)

(Dr. Wensu Chen) (.....)